UNIVERSITAT DE BARCELONA

Wide bandgap chalcogenide thin films onto transparent substrates

Mohamed Ould Salem

Tesi doctoral

Wide bandgap chalcogenide thin films onto transparent substrates

Autor: Mohamed Ould Salem

Directors: Dr. Marcel Placidi i Dr Zacharie Jehl

UNIVERSITAT DE BARCELONA

Wide bandgap chalcogenide thin films onto transparent substrates

Programa de doctorat en Enginyeria i Ciències Aplicades

Autor: Mohamed Ould Salem

Directors: Dr. Marcel Placidi i Dr. Zacharie Jehl

Tutor: Prof. Alejandro Pérez Rodríguez

IREC

UNIVERSITAT DE BARCELONA

Summary

Acknowledgements

First of all, I would like to thank the following people, who have helped me undertake this research and assisted me throughout the process, without whom I would not have been able to complete my thesis! my Ex-supervisor Edgardo for giving me the opportunity to study my PhD at IREC, for his enthusiasm for the project, for his support, encouragement and patience, my supervisors Marcel Placidi and Zacharie Victor Samuel Nathana Jehl for their help and support to overcome all the difficulties and put together all the pieces to make this project finally work. Also, I would like to thank my thesis tutor, Alejandro Pérez-Rodríguez.

I would like to give a special thank you to Diouldé, I appreciate all the help you have given me.

I would like to thank everyone at Solar Energy Materials and Systems Group (SEMS): Victor, Yudania, Nachio, Sergio, Kounal, Alax, Florian, Pedro, Maxim, Jacob, Anjelika, Markos, Alex, Rober, Enric, Fabian and Rafael. My gratitude goes out to each and every one of you for your assistance throughout this project.

I would like to thank all the members of MAScIR who made me feel like I was a part of the team during my secondment: Prof Sekkat, Safae, Siham, Sara, Nadjet, Nada, Ikrame, Yahya, Abdeljalil, Nawfel and Zakaria.

I would like to thank also all the members I have meet during my secondment at MET: Eglė, Matas and Martinas.

I would like to acknowledge the Islamic Development Bank (IsDB) from Saudi Arabia; as well as the INFINITE-CELL project (H2020-MSCA-RISE-2017-777968) from the European Commission.

Last but not least, I would like to thank my family: my dear mother Kadija Es-swidat and my late father, Ahmed Salem, to my brothers: Cheikhna, Moustapha and Mohamed Sagier, my sisters Kadijatou, Saida and specifically my brother Ethmane.

Preface

The work presented in this thesis was carried out at the Catalonian Institute for Energy Research (IREC) in Sant Adrià de Besòs (Barcelona, Spain) from 2017 to 2021 in the framework of the Islamic Development Bank (IsDB) Scholarship (60033643) Kingdom of Saudi Arabia; and of the INFINITE-CELL project (H2020-MSCA-RISE-2017-777968) from the European Commission.

This thesis focuses on the development of high efficiency solar cells based on Ga rich $Cu(In_{1-x}Ga_x)Se_2$ chalcopyrite-based devices on fluorine-doped tin oxide (FTO) transparent substrates, in order to develop a perfect top cell candidate in c-Si/CIGS tandem solar cell, toward realizing future low cost and high efficiency photovoltaic (PV) devices.

Structure of this thesis: The work in this manuscript is divided into five chapters presented in the following order:

- **The first chapter** is devoted to the introduction and subdivided into several sections. A first part starts with the rapid growth in global energy consumption and its impacts on climate change, as the increased atmospheric concentrations of carbon dioxide (CO_2) and the change in the earth's temperature. One of the main reasons for these phenomena is the heavy dependence of global energy consumption mainly on fossil fuels. Therefore, a second section is dedicated to the evolution of the installed capacity and the cost of various renewable energy sources in comparison with fossil fuels, as an alternative clean energy, less expensive, available in some capacity nearly everywhere, and can meet world energy demand. In a third section, solar photovoltaic energy is introduced as one the most abundant and cleanest renewable energy source available; solar PV global capacity and annual additions, principles of Solar Cell operation, PV technologies generations, thin film CIGS technology and the best research-cell efficiencies for the different PV technologies, are then described. The final section aims to present the objectives of the present thesis.

- **The second chapter** is subdivided into several sections according to the typical structure of a CIGS-based thin film solar cell. The first section is an introduction on the most attractive priorities of CIGS thin film solar cells, mostly wide bandgap CIGS. The second section is focused on the properties and advantages of transparent substrates,

specifically fluorine doped tin oxide coated glasses (FTO). In the third section, an overview on the fundamental effects of gallium contents on the properties of CIGS absorber layers and solar cells is provided, including the crystal structure, the opto-electrical properties, phase composition, as well as the band gap widening which constitutes the main objective of substituting gallium (Ga) for indium (In). The fourth section is devoted to the deposition techniques of polycrystalline CIGS materials. The fifth section is dedicated to the development of Ga rich CIGS solar cells. Then, the main parameters limiting the efficiency of wide band gap CIGS thin film solar cells is discussed, and strategies for reaching higher efficiencies and the use of alternatives buffer layers, are proposed.

- **In the third chapter** a brief overview of the absorber's synthesis methodology is presented including a description of the different thin film deposition methods and the corresponding characterization techniques used in the course of this thesis. The main deposition and characterizations parameters used in the synthesis and characterization are detailed as well.

- **The fourth chapter** is dedicated to the presentation of the results regarding the optimization of a baseline process for Ga rich CIGS on FTO substrate based on a sequential process, including the deposition of metallic stack precursors by sputtering and thermal evaporator, and followed by reactive annealing under chalcogen atmosphere. The first section has been dedicated to the optimization of compositional ratios CIG and GIG of Ga rich CIGS, the second section is about the effects of annealing temperature on such precursors, and the last section deals with the development of other possible buffer layers than CdS for Ga rich CIGS solar cells. A complete chemical/structural/morphological characterization of the films is performed using several techniques including X-ray Fluorescence (XRF), X-ray diffraction analysis (XRD), Raman spectroscopy and scanning electron microscopy (SEM).
- **The fifth chapter** focuses on the influence of the incorporation of alkali elements strategies on Ga-rich CIGS absorber films and the impact on the devices performance. The first section examines the effect of sodium pre-incorporation into Ga rich CIGS

absorbers and the second section on the heavy alkali (CsF and RbF) post-deposition treatment (PDT).

Finally, the conclusions of the present work and different future research pathways to increase device performance of wide bandgap CIGS as a viable contender in tandem solar cells, are described.

Table of figures

List of tables

1 Introduction

1.1 General context

Access to energy is an important component for every aspect of life, in particular, economic growth, transport, health, education, etc. In fact, despite increased global energy production since the middle of the last century, as shown in Figure 1.1, a seventh of the world's population still do not have access to electricity, especially in rural communities the majority of whom are located in countries of the sub-Saharan Africa, south America and south-east Asia [1][2][3].

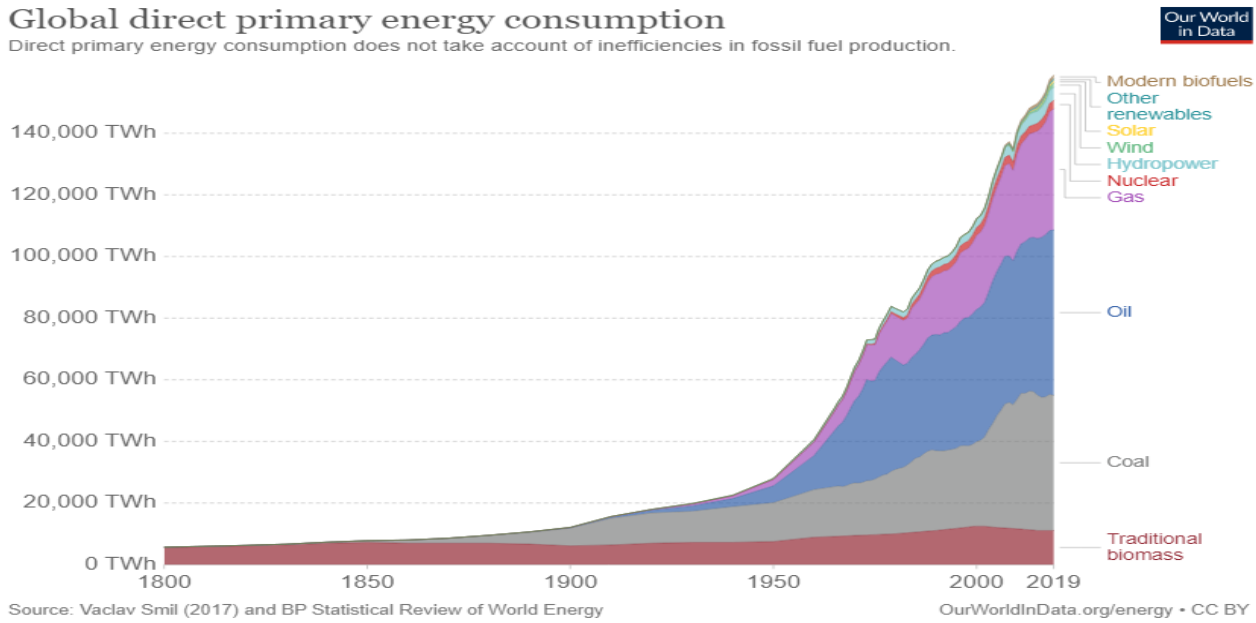

Figure 1.1: Global direct primary energy Consumption. (Source: Vaclav Smil (2017). Energy Transitions: Global and National Perspectives. & BP Statistical Review of World Energy.

Additionally, the main source of energy production in the word are fossil fuels, mainly coal, oil and natural gas [4][5]. This near-total dependence on fossil fuels causes serious environmental problems, such as climate change, global warming, air pollution, and acid rain [6][7][8]. For example, electricity generation is responsible for 30% of the total carbon dioxide (CO_2) emissions in the world [9]. As observed in figure 1.2, the concentration of (CO_2) in the atmosphere increased from 270 parts per million (ppm) in 1880, to 410 ppm in 2019, that has resulted in a rapid increase in Earth's average surface temperature to reach 1.1°C during the

same period. According to the National Oceanic and Atmospheric Administration of United States, January 2020 was the hottest January on record globally.

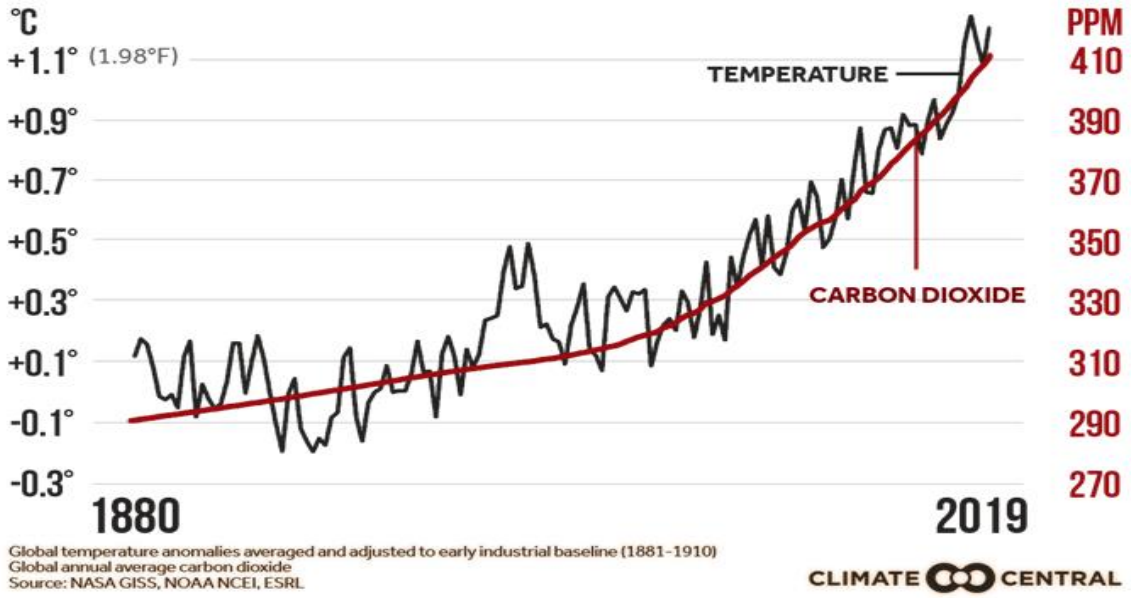

Figure 1.2: Global atmospheric carbon dioxide concentrations in parts per million (ppm) and temperature change. Source: NASA GISS, NOAACEL.ESRL.

Moreover, fossil fuel depletion, as a result of increased demand and the rapid price increases, has been identified as a future challenge [10]. As observed in figure 1.3, if the world continues to consume fossil fuels at 2011 rates, the reserves of oil, gas and coal will last a further 40, 50 and 80 years, respectively. For the previous reasons, to meet the increasing energy demand for energy due to rapid population growth, technological progress, rising standard of living and to cope with climate change, renewable energies have been considered as the best alternative sources to fossil fuels, being environmentally friendly and virtually inexhaustible.

Renewable energy in general is the conversion of a renewable natural source into thermal or electrical energy, such as solar, wind, hydro, tidal, geothermal and biomass energies [11]. These resources are abundant worldwide and can meet many times the world's energy demand and contribute to the reduction of greenhouse gas emissions that is required to achieve the targets of COP26 in 2030 for limiting average global surface temperature about 1.5 °C[12] [13]. In the last decade alone, this sector has shown strong development, resulting

in a low levelized cost of electricity for renewable energy and an increase in its share in the energy generation global mix from 5.9 % in 2009 to 13.4% in 2019, as shown in Figure 1.3. This growth has been especially high for solar PV and wind power, which grew up at average annual rates of 36.5% and 23.0% respectively.

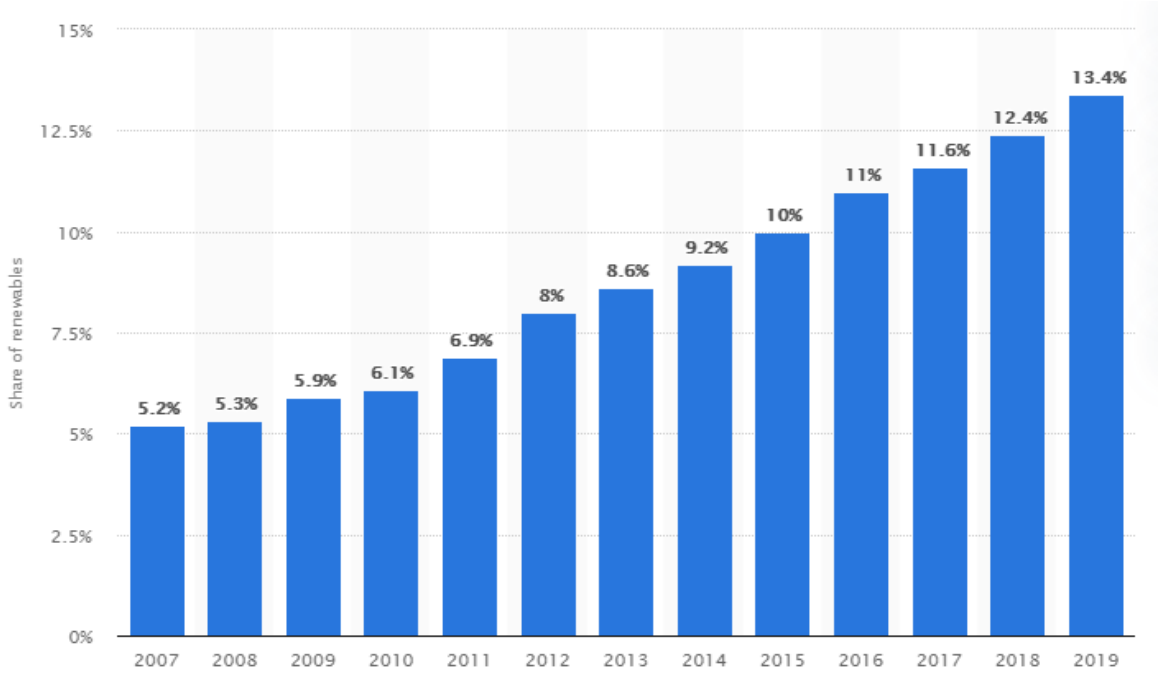

Figure 1.3: Share of renewable power sources in energy generation globally from 2007 to 2019 [source https://www.statista.com/statistics/489131/share-of-renewables-in-power-generation-globally].

1.2 Levelized cost of electricity for various energy sources

The Levelized Cost of Electricity (LCOE) is the most frequently method of comparing the cost of different energy technologies and iIts economic feasibility [14]. It accounts for all lifetime costs of the system including operation, maintenance, construction, taxes, insurance, and other financial obligations of the project. They are then divided by the expected total energy outcome in the system's lifetime (kWh)[15][16].

The simplified calculation formula for LCOE is as follows [14]:

$$LCOE = \frac{\sum_{t=1}^{n} \frac{I_t + M_t + F_t}{(1+r)^t}}{\sum_{t=1}^{n} \frac{E_t}{(1+r)^t}} \qquad (1.1)$$

- $\mathbf{I_t}$ = Investment and expenditures for the year (t).
- $\mathbf{M_t}$ = Operational and maintenance expenditures for the year (t).
- $\mathbf{F_t}$ = Fuel expenditures for the year (t).
- $\mathbf{E_t}$ = Electrical output for the year (t).
- **r** = The discount Rate.
- **n** = The (expected) lifetime of the power system.

Figure 1.4 shows LCOE for various energy source. A significant reduction in the cost for solar and wind energy is observed, mainly solar energy which is divided into photovoltaic (PV) and solar thermal, and gets the most attention because they are straightforward to implement and provide reasonable conversion. This explains the drop in cost for PV energy over the past decade e.g., the cost per MWh of solar PV fell from 248 $ in 2010 to 40 $ in 2019, making it one of the most developed sustainable energy sources. According to the International Energy Agency (IEA) roadmap, PV's share of global electricity should reach 16% by 2050. In order to achieve the vision in this roadmap, the total PV capacity installed each year needs to rise 124 GW per year on average, with a peak of 200 GW per year between 2025 and 2040 [17].

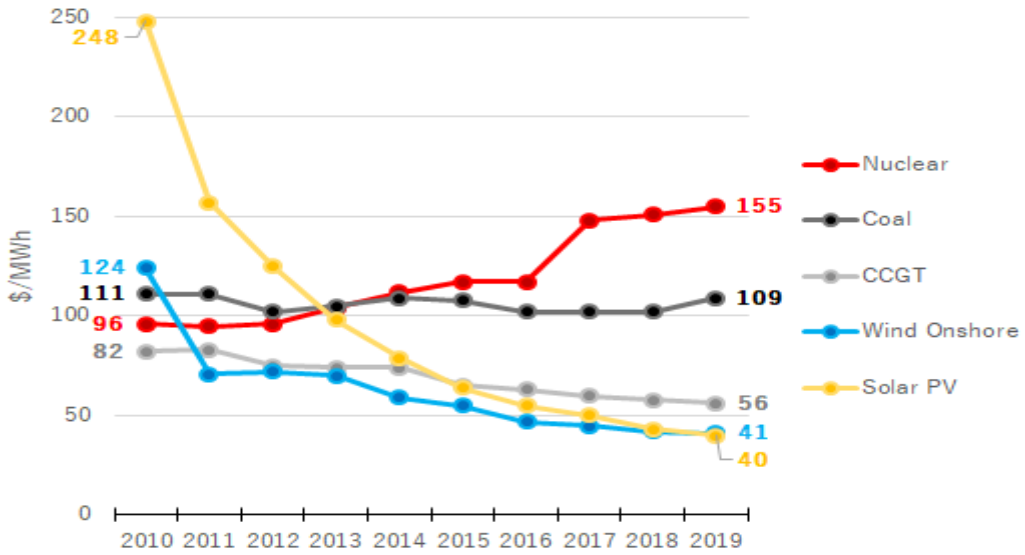

Figure 1.4: LCOE Comparison 2010-2019 [Source: Lazard, Levelized Cost of Energy Analysis - Version 13.0].

1.3 Photovoltaic technologies

Solar energy is an inexhaustible, eco-friendly energy and freely available in large quantities more or less anywhere in the world. According to previous estimations, the solar radiation reaching the Earth crust each year represents 7.500 times the world's total annual primary energy consumption [18].

Photovoltaic solar energy is the transformation of part of the solar radiation (heat) into electricity (work) employing a solar cell [19]. It is the cleanest and fastest growing power generation technology among solar energy sources [20] [21] and is widely used as an autonomous electricity source in isolated locations, water pumping, communications, satellites and spacecraft, due to its ease of installation and low cost, as well as for megawatt-scale power plants [22]. As noted in figure 1.5 the solar PV global capacity has grown from 23 gigawatts in 2009 to more than 627 gigawatts in 2019 [23], and it is expected to reach 840 in 2030 [24].

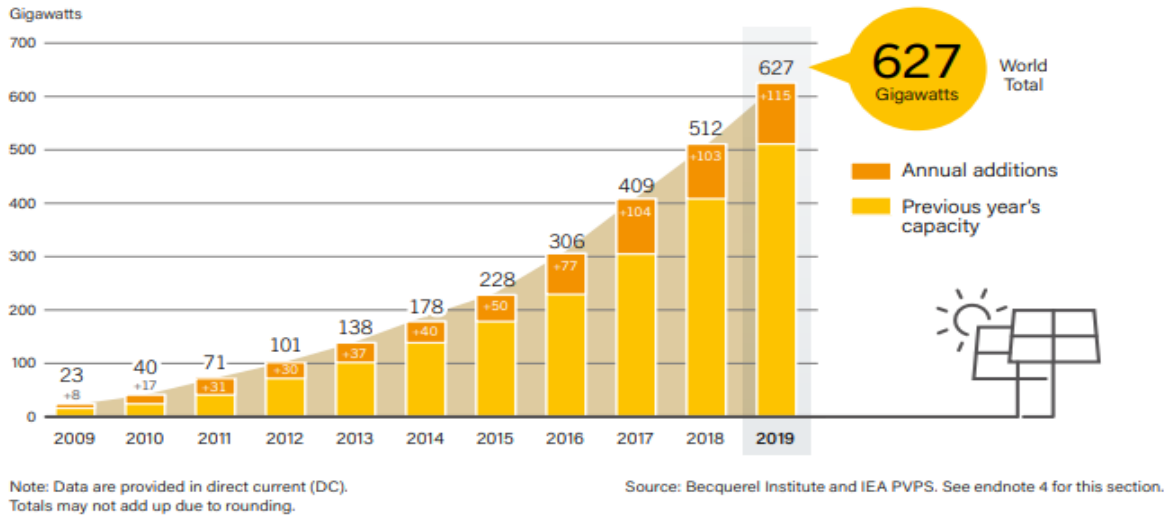

Figure 1.5: Solar PV Global Capacity, by Country and Region, 2009-2019 [25].

1.4 Photovoltaic cell technologies

The principles of Solar Cell operation is based on the electrical properties of semiconductors. The simplest solar cell is build using a p-n junction as selective carrier filter, and is made by contacting a P-type with an N-type semiconductor. When N and P type semiconductors are placed together to form a PN junction, as shown in Figure 1.6, a very large charge carrier density gradient exists between both sides of the PN junction. Electrons migrate into the P-side and holes migrate into the N-side. The diffusion of an electron from the N-side to the P-side leaves a donor site behind on the N-side, and likewise the hole leaves an acceptor site on the P-side.

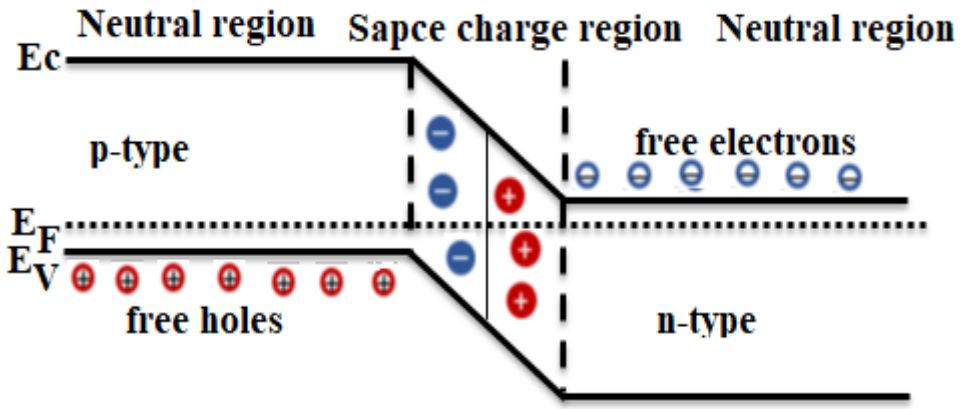

Figure 1.6: PN junction.

When the junction is illuminated, photons have energies higher than the bandgap of the semiconductors (hv> Eg) creating then electron-hole pairs. Electrons in the conduction band diffuse from the junction to the bulk of the semiconductor, while leftover holes in the valence band migrate from the bulk to the junction. Before recombination could take place, these photo-generated electrons and holes are separated by their respective diffusion and selection at the pn junction. This charge separation causes a current flow across the junction which when connected to an external circuit gives rise to the short-circuit current, Isc. In the absence of an external circuit, there is a build-up of the photo-generated charge carriers on either side of the junction giving rise to the open-circuit voltage, Voc. When an electric load is connected to the circuit, the photo-induced electromotive force leads to power generation and an energy transfer from the cell to the load (Figure 1.7). The maximum conversion efficiency of a single

junction solar cell, which will be discussed later, is calculated according to the detailed balanced formalism, and is called the Shockley-Queisser limit [REFERENCE].

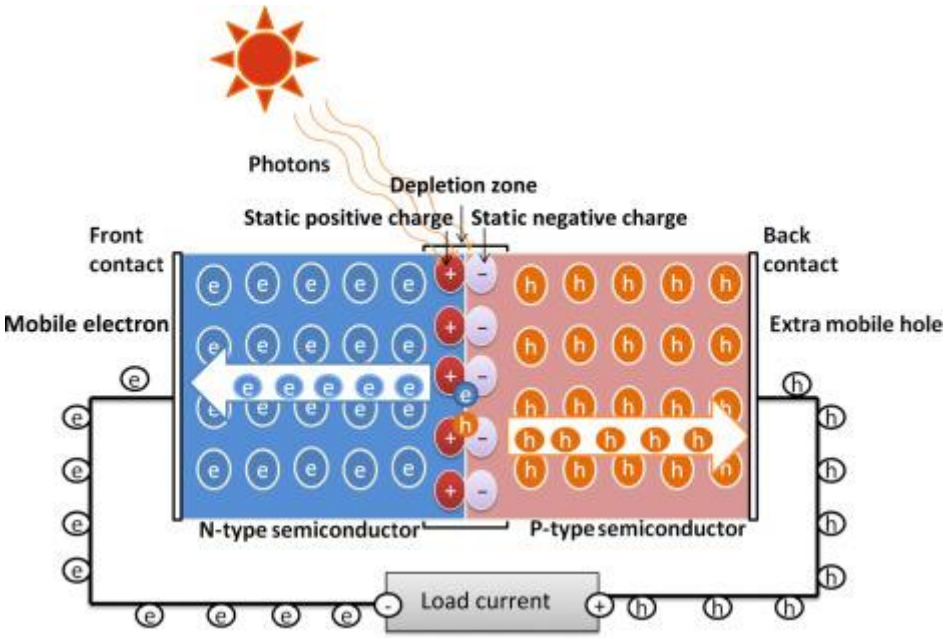

Figure 1.7: Schematic representation of a p-n junction photovoltaic cell [26].

1.5 Classification of photovoltaic technologies

The long term development of different photovoltaic technologies throughout the past years, relies on the necessity of cost reduction, efficiency improvement, availability of abundant materials and simplification of technological processes involved in the fabrication, in order to make it more competitive. Based on these previous objectives, PV technologies are usually divided into three different generations.

First Generation of PV Technologies: mono-crystalline and polycrystalline silicon

The first generation of PV technologies is the dominant one in the commercial production of solar cells, representing 92% of photovoltaic market (figure 1.8) [27],[28]. This technology includes both monocrystalline and polycrystalline Si solar modules [29].

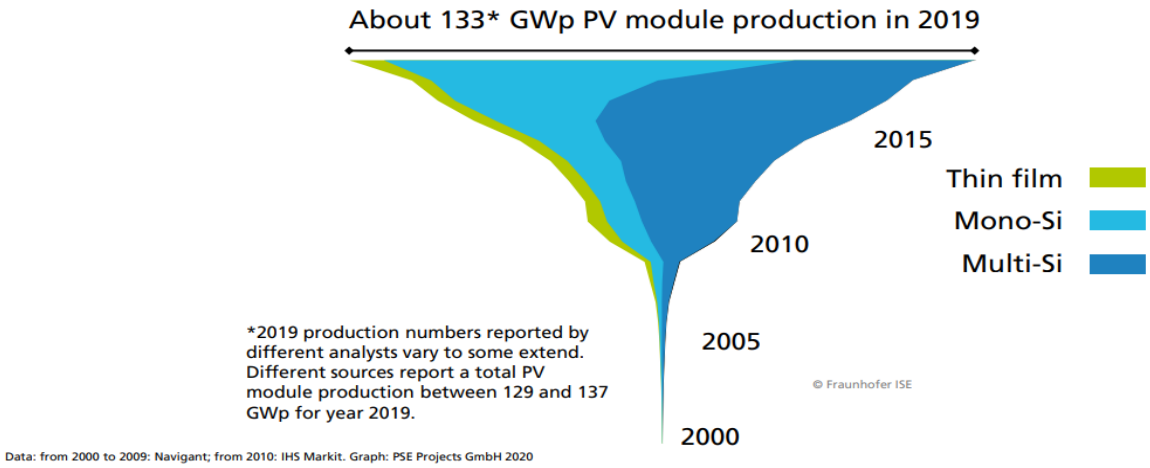

Figure 1.8: Annual PV Production by Technology Worldwide (in GWp) [30].

The advantages of this photovoltaic generation are that silicon is one of the most abundant elements in the earth's crust (27%), the high efficiency demonstrated at cell and module level with a record laboratory solar cell of 26.7%, the long-term stability, and the reliability because share a lot of common points with the electronic industry [31]. Among the main disadvantages one can mention the relatively high cost to produce c-Si wafers (even if today the prices have decreased a lot and Si solar panels are very cheap) and that most of this industry is concentrated outside of Europe, the requirement of high temperature processing, and the necessity of thick wafers because the material exhibit indirect bandgap and in consequence relatively low light absorption coefficient. In addition, the silicon wafers are fragile, therefore hardly suitable for flexible applications [32] or BIPV. Nevertheless, this is a very mature and consolidated technology, and currently is clearly dominating the PV market.

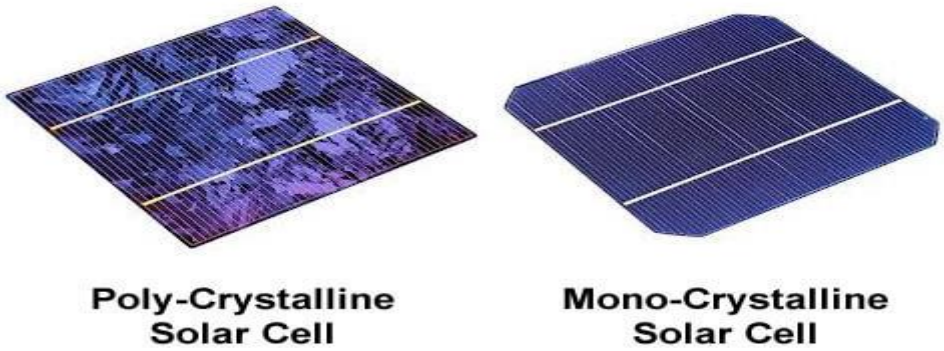

Figure 1.9: Two types of crystalline solar silicon, source, https://www.tindosolar.com.au/learn-more/poly-vs-mono-crystalline/ (accessed on 26/11/2020).

Second Generation PV Technologies: Thin Films-Based Solar Cells (TFSCs)

The second generation of solar cells started to be developed in the 1980s. The main advantage of this family of technologies is their potential to reduce production costs, as well as offer new possible applications of PV energy, hardly achieved for c-Si such as flexible and semi-transparent or transparent devices [21]. Firstly, owing to their high absorption coefficient as compared to c-Si, as a result of their direct bandgap, a very thin layer is sufficient to absorb a large part of the solar spectrum, which reduces material consumption. [33] In addition, most of the thin film PV technologies are produced using faster and cheaper manufacturing process for large-area devices [34]. These materials have also demonstrated long-term stability even in high temperature environments [27]. Secondly, the large number of chemical and physical methods useful to deposit thin films, and their adaptability to almost any kind of substrates, offer a wide variety of choices in terms of the device design and fabrication, with a lot of freedom for the improvement of device performance [35].

Production of commercial thin-film modules started in 2006; today, the global annual PV production by thin-film panels has reached 5.7 GWp. As show in figure 1.10 they currently represent 5.4 % of the annual global PV production.

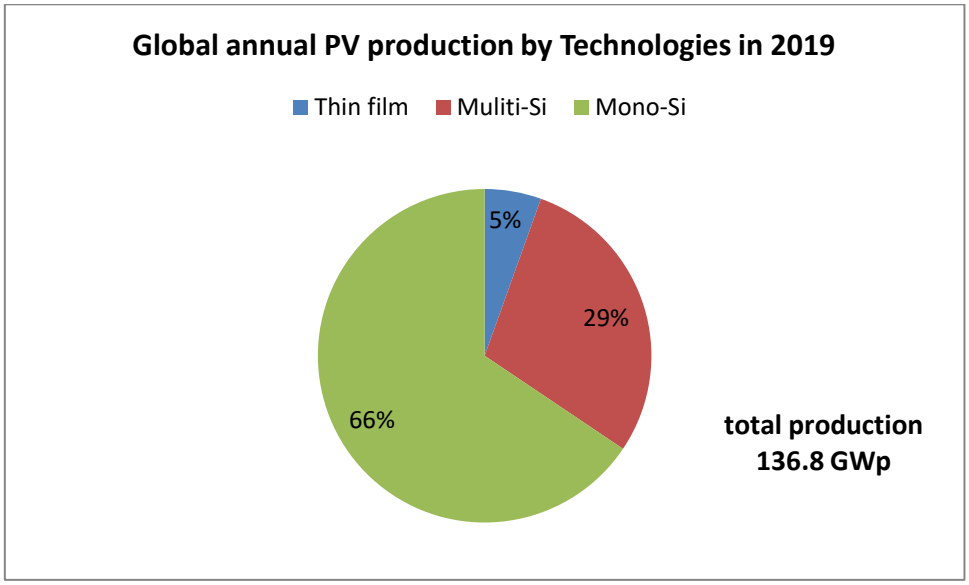

Figure 1.10: PV Production by Technology, source data from [30].

The thin film PV technologies that have reached commercial step are based on amorphous silicon (a-Si), cadmium telluride (CdTe), and copper indium gallium di-selenide (CIGS)[36][37][38]. As shown in Figure 1.11, the market share of thin films in the global production of photovoltaic solar panels was 15% in 2009, and then gradually declined due to the gradual reduction of a-Si technologies production, correlated to the impressive increase of c-Si modules fabrication in Asia countries. In addition, during last years, CdTe have maintained some market portion for thin film technologies.

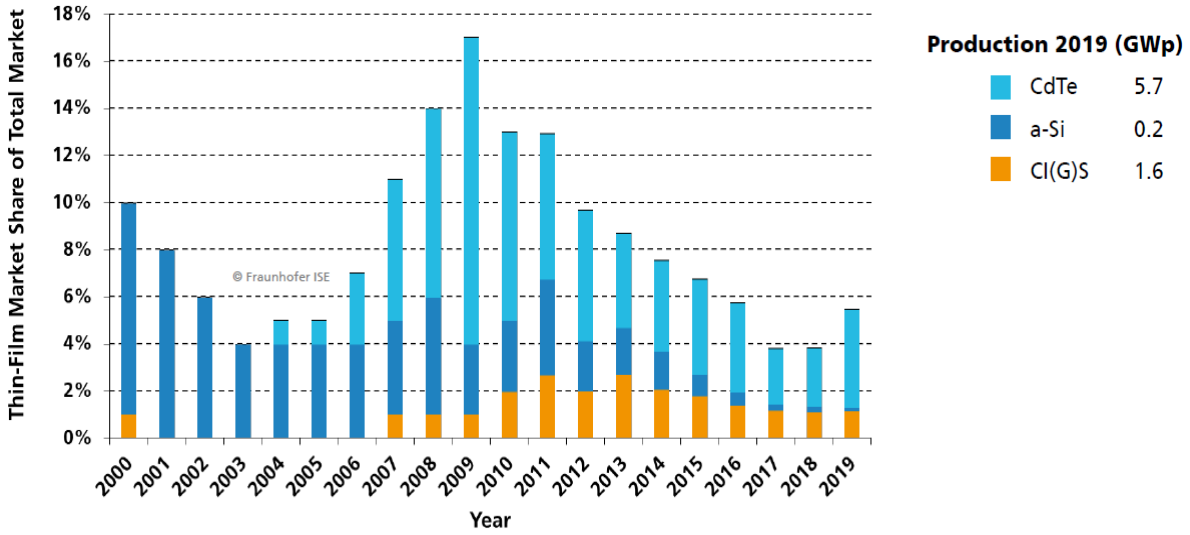

Figure 1.11: Thin film market share in global production of PV modules from, 2000-2019 [30].

Third Generation PV Technologies: High Efficiency Solar Cells and New Concepts

The third generation of PV technologies is based on emerging materials and concepts such as dye-sensitized solar cells (DSSC), organic photovoltaics (OPV), quantum dots solar cells, perovskite, multi-junction cells, hot carrier cells, etc. Most of these concepts can promise either very high efficiency and/or very reduced production costs, but are still under development, and will require yet several years of development and validation to be in the market. One of the most interesting concepts developed among the third generation of PV, are the so-called multi-junction or tandem solar cells. This type of devices is based on the stacking or monolithic integration of individual solar cells with different bandgaps. The use of multiple devices allows to push the Shockley-Queisser limit towards values much higher than the maximum ones for a single junction solar cell. Efficiencies higher than 40% have been demonstrated in the laboratory with a theoretical thermodynamic limit as high as of 86% for an infinite number of solar cells [39]. This technology is nowadays mainly based on III-V

semiconductors, being then very expensive and only applicable in very specific cases such as the use in non-terrestrial applications with concentration as for example telecommunication satellites [38] [40].

Currently, the extension of tandem concepts toward cheaper and simpler technologies, including thin films, perovskites or organic solar cells, is under intensive research due to the possibility to obtain unprecedented conversion efficiencies at very low cost.

Finally, figure 1.12 summarizes the conversion efficiency records reported up to now for individual solar cells as well as for large area modules, where c-Si, thin films (CIGS and CdTe) and lately perovskites are the most relevant technologies. In figure 1.13, the famous Efficiency Chart of NREL (National Renewable Energy Laboratory) summarizing the evolution of the conversion efficiency for the different solar cell technologies is presented. Clearly, and for the moment, efficiencies higher than 30% in the laboratory are only achievable with tandem devices concepts, and the present Thesis is focused in the development of materials that can be in the near future directly applied for such type of solar cells.

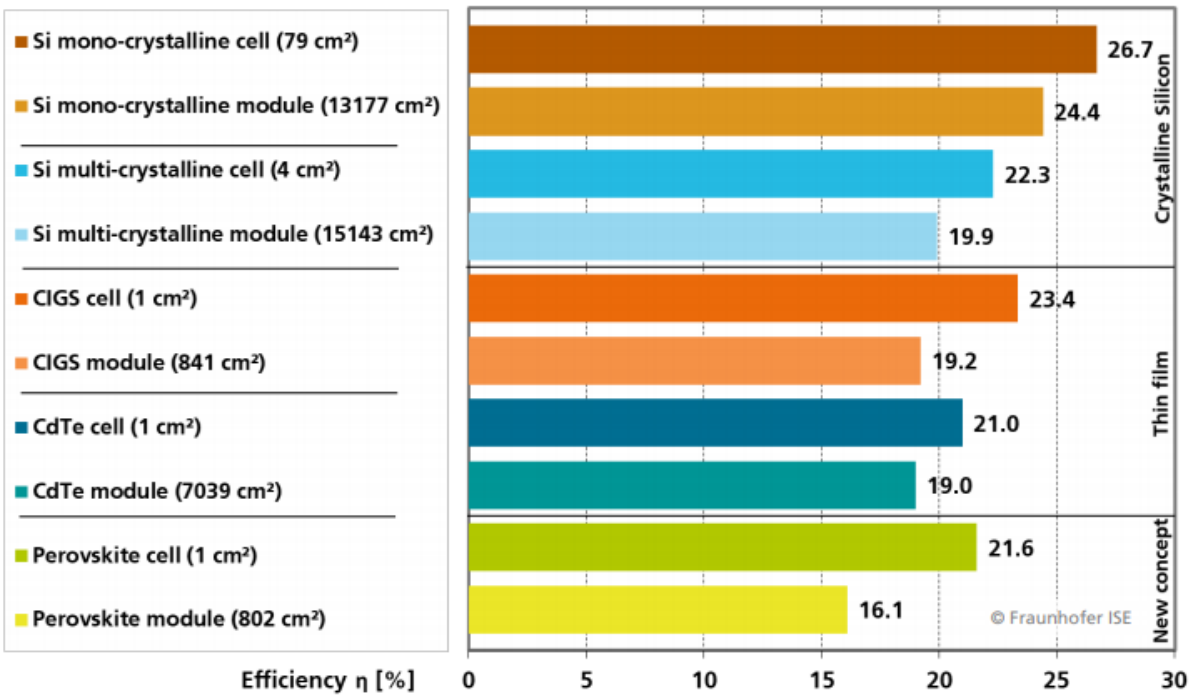

Figure 1.12: Efficiency comparison of three technologies: Best Lab Cells vs. Best Lab Modules [30].

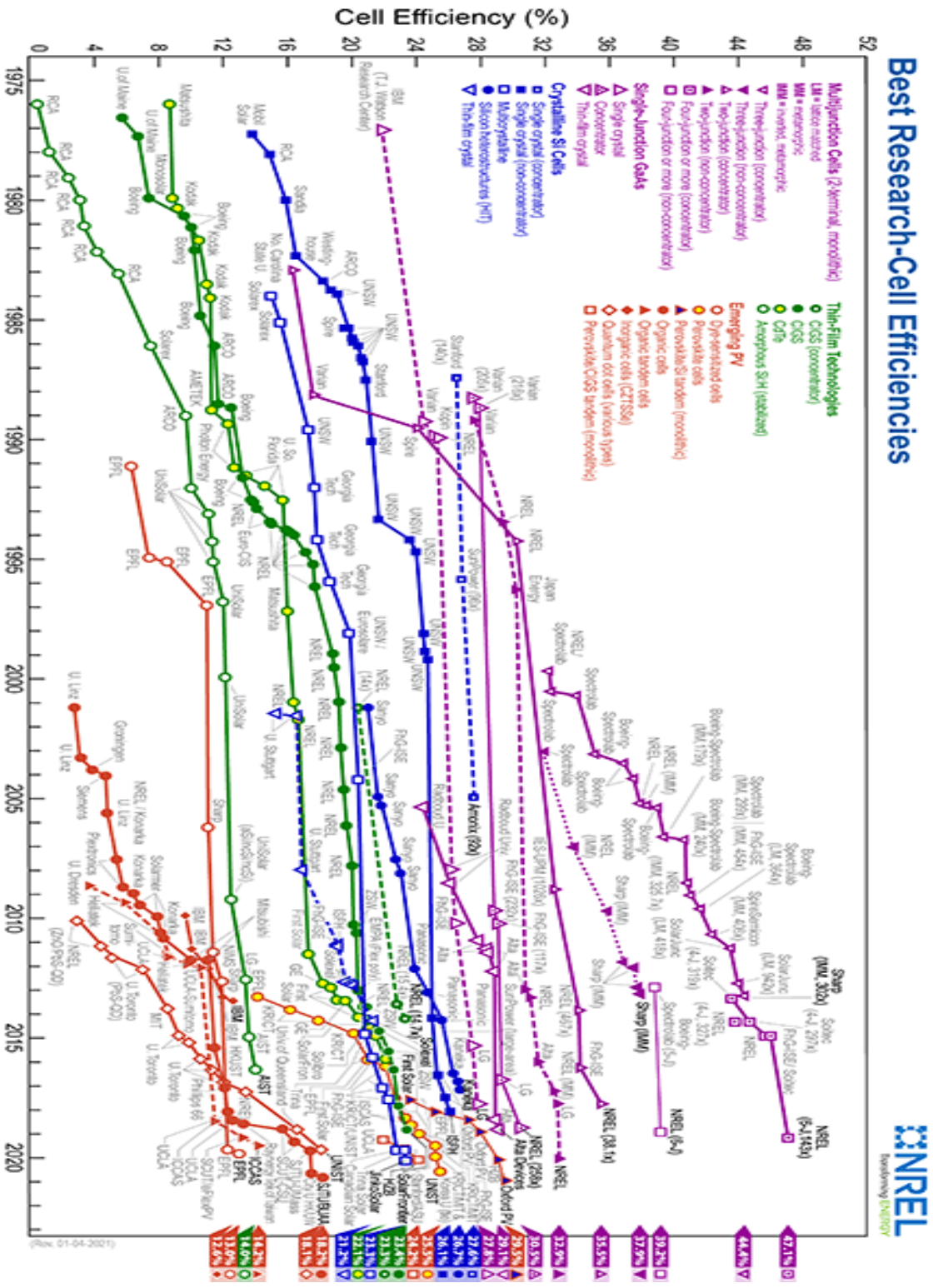

Figure 1.13: Best research-cell efficiencies for the different PV technologies, source National Renewable Energy Laboratory.

1.6 Objectives of the present thesis

In view of the progresses and relevance of emerging concepts for PV, in particular of the enormous potential of tandem solar cells based on already demonstrated industrial technologies, the main objective of this thesis is to develop **wide bandgap CIGS-based thin film solar cells onto transparent conducting oxide substrates.** This type of devices exhibit the properties required to be used as top cells in tandem configuration, and can open very interesting perspectives towards cost-efficient photovoltaics. To achieve this general objective, the following sub-objectives are defined:

1- Identification of the main mechanisms that are limiting the conversion efficiency of wide bandgap Ga-rich CIGS solar cells and analysis of the possible strategies for overcoming these challenges.

2- Development and optimization of a two-step sequential process based on the sputtering of metallic stacks followed by a reactive thermal annealing, for Ga-rich CIGS alloys (Ga / (Ga + In) ≥ 0,70) thin film solar cells onto highly transparent fluorine doped tin oxide substrates.

3- Implementation of advanced strategies for selective surface passivation to improve the conversion efficiency of wide bandgap Ga-rich CIGS solar cells.

2 Ga-rich CIGS based thin film solar cells technologies

2.1 Introduction

Chalcopyrite $CuIn_{1-x}Ga_x(S_{1-y}Se_y)_2$ (CIGS)-based thin film solar cells (TFSCs) is the most efficient thin film photovoltaic technologies today [41]. Due to their high PCE record of 23.35% at laboratory scale and 19.2% at the commercial module level [42][30], low costs, high stabilities, high absorption coefficient ($\alpha \approx 10^5$ cm^{-1}) [43], and the possibility to tune its bandgap by substituting In by Ga or Se by S, is being considered for different possible PV applications. As an example of the flexibility of this technology, the band-gap can vary from 1.0 eV ($CuInSe_2$) to 1.68 eV ($CuGaSe_2$)[44][45] and the material has the possibility to be deposited by several different techniques onto various types of substrates, whiles keeping high conversion efficiency [35]. Ga rich CIGS ($x \geq 0.7$) are desirable in several aspects. First, a band-gap of 1.5 eV ($x \approx 0.7$) is closer to the optimum theoretical band gap of CIGS absorber layer [46] Although the optimum band gap of a single junction solar cell ranging between 1.2 to 1.4 eV according to Shockley and Queisser's calculations. In addition, the higher voltage that can be achieved with Ga rich CIGS is necessary in solar cell modules because energy loss due to series resistances can be reduced. Ga rich CIGS thin film is also required for the wide bandgap top cells in a tandem solar cell [47]. In this Chapter, the most relevant characteristics of Ga rich CIGS semiconductors will be presented and discussed, together with the most relevant methodologies for the synthesis and deposition of the material, followed by a review of the solar cell structure, and finally with a discussion of the current strategies toward enhanced conversion efficiency.

2.2 Transparent back contact

The typical structure for a CIGS-based thin film solar cell is shown in figure 2.1. The most common material stack configuration consists of soda lime glass (SLG)/molybdenum back contact (Mo) /CIGS absorber layer / buffer layer / window layer/ Ni/Al metallic grid and finally and anti-reflection layer (***SLG/Mo/CIGS/CdS/i-ZnO/ZnO:Al/Ni-Al/MgF_2).*** This

configuration is in particular called substrate configuration, and it was implemented for the first time by Boeing [48].

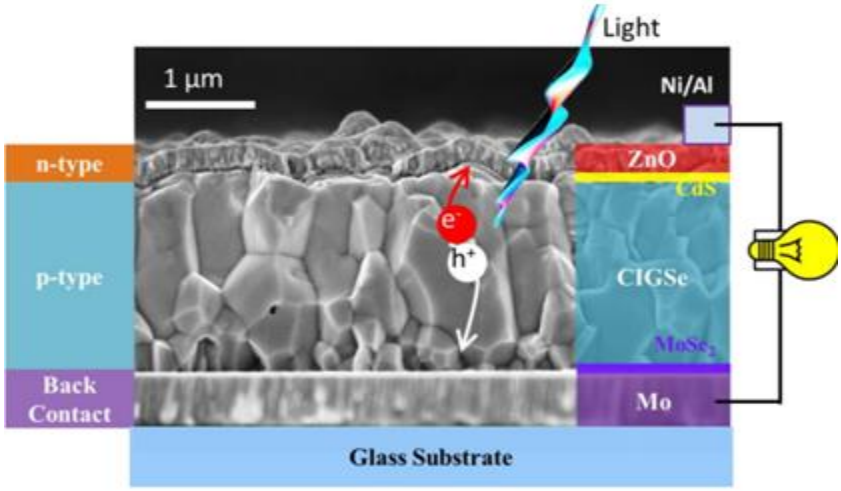

Figure 2.1: Device structure of a typical CIGS solar cell [49].

Most of the CIGS based solar cells use Mo as back contact. Nevertheless, more advanced applications require wide band gap CIGS such as for the use as top cell in multi-junction devies, semi-transparent or transparent solar cells for BIPV / BAPV, or bifacial solar cells for highly reflective environments (snow, deserts). All of these devices require a transparent back contact [50][51], and transparent conductive oxides (TCOs) are currently the best candidates. Figure 2.2 presents different applications that require transparent substrates.

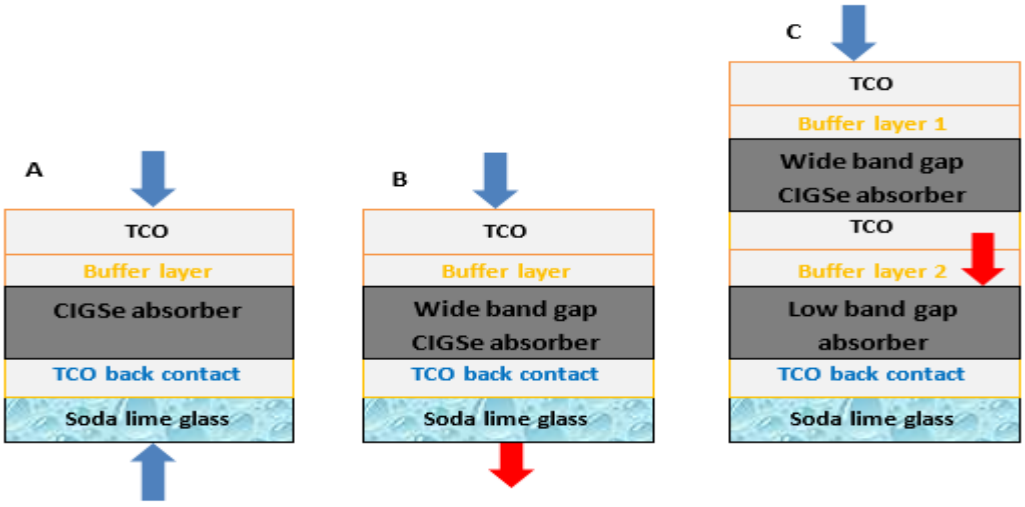

Figure 2.2: Device structures of (a) bifacial, (b) semi-transparent, and (c) tandem CIGS-based TFSCs fabricated using TCO contacts.

The most commonly transparent conducting electrodes (TCEs) used as a back contact, are indium tin oxide (ITO), fluorine-doped tin oxide (FTO) and aluminum-doped zinc oxide (AZO), due to their high optical transparency and low electrical resistivity [50]. Table 2.1 shows record efficiency of CIGS using an opaque and transparent back contact.

Table 2.1: Record efficiency of CIGS using an opaque and transparent back contact.

Back contact	**Eff (%)**	**FF (%)**	**Voc (mV/cm^2)**	**Jsc (mA/cm^2)**	**Ref**
Mo	23.3	79.7	734	39.6	[42]
ITO	15.2	68.2	651	34.4	[52]

FTO back contact

Tin oxide (SnO_2) is a wide band gap (3.6 eV) N-type semiconductor that exhibits high optical transparency to the visible light ($T \geq 85\%$) and low electrical resistivity due to the presence of oxygen vacancies in the lattice [53]. Substituting oxygen atoms in the SnO_2 structure by fluorine SnO_2:F (FTO) largely enhanced the electrical conductivity [54] . FTO film possess the required features for being a good candidate as transparent back contact for PV applications such as low electrical resistivity, high optical transmittance, thermal and chemical stability, and low cost.

CIGS solar cells onto FTO back contact have been widely investigated. Nakada et al., showed that the efficiency of CIGS solar cell using FTO back electrode is the same as that of conventional CIGS using Mo, if the substrate temperature during the CIGS deposition is below 500°C. The degradation of the efficiency when the CIGS absorber is deposited at temperatures above 500°C is caused by the partial deterioration of the FTO substrate and in consequence the significant increase of the electrical resistivity of the back contact as it is shown in the figure 2.3, together with the possible formation of Ga_2O_3 at the FTO/CIGS interface [52][55][56].

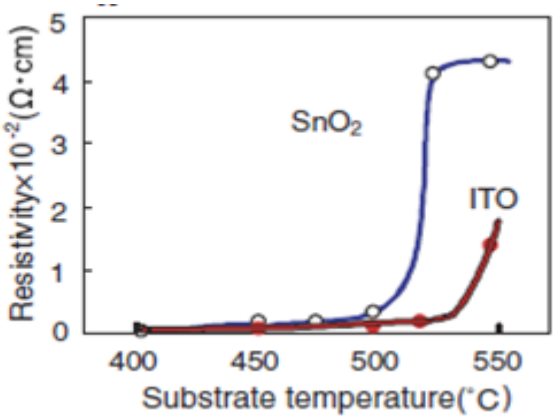

Figure 2.3: Resistivity of SnO_2:F measured after removing CIGS layers, using different substrate temperatures during CIGS deposition [52].

On the other hand, several studies have demonstrated that the transparent conducting oxides hinder the diffusion of Na from the glass substrate into the CIGS absorber layer, because these compact oxide layers act as very efficient chemical diffusion barriers [57][58]. Figure 2.4 shows the SIMS depth profiles of sodium in CIGS absorber, by comparing the sodium content diffusing from different substrates (using several TCOs and Mo as reference). Although the FTO was thinner than the Mo and ZnO, the amount of sodium diffusing through FTO was lower than in the other cases. We can also note that the amount of Na reduces as the ZnO thickness increases. One can thus conclude that a thin FTO layer act as a good diffusion barrier of Na.

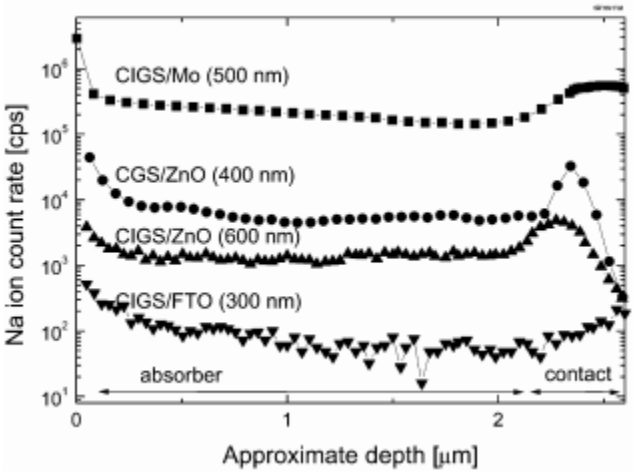

Figure 2.4: Comparison by SIMS of the amount of Na diffusing from SLG in CIGS through different transparent conductive oxides and Mo [58].

2.3 Effects of Ga contents on properties of CIGS thin films

Gallium incorporation in $CuInSe_2$ has been one of the most relevant strategies to increase the conversion efficiency of this technology to values well beyond 20%. The highest efficiency achieved for conventional CIGS devices is always obtained with 30% of gallium Ga/(Ga+In) (GGI of around 0.3). Despite this, highest Ga-contents are very interesting because can be useful to achieve the second theoretically ideal band gap for sunlight energy conversion at approximately 1.4 eV (the first maximum corresponds to 1.18 eV). In addition, even higher bandgaps are very relevant for the development of cost-efficient tandem concepts, where Ga-rich (GR) CIGS is a very interesting candidate as top cell. Nevertheless, we have to consider that Ga content in CIGS material influences its electrical, optical and structural properties [21] [22] [23].

A key part of a thin film solar cell device is the absorber layer; the structural, electrical and optical properties of a good absorber make the difference between photovoltaic materials. Therefore, the solar cells development in terms of efficiency, stability and cost is strongly related to the material used as an absorber layer. Consequently, a good understanding of the absorber material properties is essential.

A- Crystal structure

$CuIn_{1-x}Ga_x(S_{1-y}Se_y)_2$ is an I–III–VI_2 semiconductor material, which can crystallize in a tetragonal chalcopyrite structure similar to that of the $CuInSe_2$ structure, obtained by doubling the zinc-blende structure along the z-axis, as shown in Figure 2.5 (A). The Zn sites are occupied in an ordered manner by atoms of groups I (Cu) and III (In or Ga) (cations) elements and the other sites occupied by atoms of group VI (Se) (anions) elements. The ordered occupation of metals could result in tetragonal or rhombohedral structures with three crystal structures: chalcopyrite, CuAu and ordered vacancy compounds (OVC). The chalcopyrite structure has a specific metallic order and produces a tetragonal ($I\bar{4}2d$) mesh, in which Cu^+ occupies the (0,0,0) site and In^{3+} or Ga^{3+} occupies the (1/2,1/2,0) site in metallic subnets, as shown in Figure 2.5 (A). The CuAu type structure has a tetragonal cell of ($P\bar{4}m2$), is distinguished from the chalcopyrite structure by the position of the cations (III), which are aligned on a plane while the chalcopyrite phase presents the two types of cations (I) and (III) ordered in each plane, as shown in Figure 2.5 (B). Su-Huai et al. [59] show that the formation of CuAu is more probable in Ga poor CIGS than in Ga rich CIGSe. The ordered vacancy compound OVC structure is distinguished from the chalcopyrite, that in the chalcopyrite structure, each selenium atom is bonded with two copper atoms and two indium atoms, while in the OVC structure, a fraction of copper atoms is replaced by vacancies or indium atom, as shown in Figure 2.5 (C), the OVC including $Cu(In,Ga)_5Se_8$, $Cu(In,Ga)_3Se_5$, and $Cu_2(In,Ga)_4Se_7$). Nishimura et al. reported that the OVC layer formation is easy on the surface of Ga poor CIGS [60] [61].

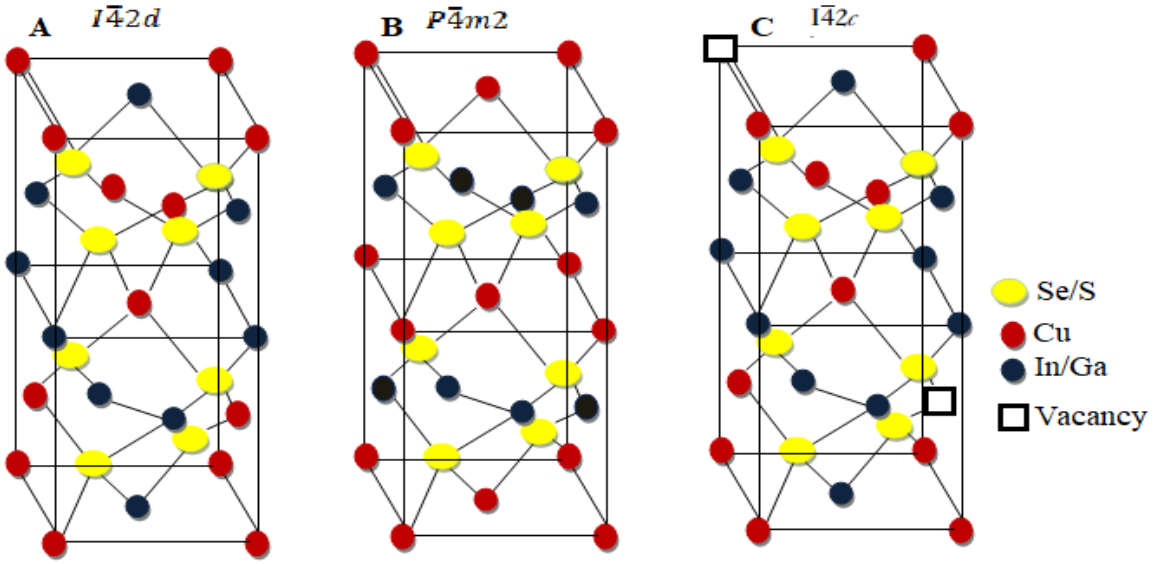

Figure 2.5: Crystallographic structure of $CuGaInSe_2$. (a) The Chalcopyrite, (b) the CuAu and (c) the OVC compound.

Substituting Gallium for Indium should result in a change of the structure; especially, lattice parameters c and a. The ratio of the tetragonal chalcopyrite lattice parameters c/a distortion is slightly different from 2 and it decreases with the GGI ratio from 2.01 in $CuInSe_2$ (a_{CIS} = 5,777 Å, c_{CIS} = 11,590 Å), to 1.96 in $CuGaSe_2$ (a_{CGS} = 5.604 Å, c_{CGS} = 11,009 Å). The lattice constants of $CuIn_{1-x}Ga_xSe_2$ variation as functions of x are described by the following equation [62].

$$a_{CuIn1-xGaxSe2} = (1 - x)a_{CuInSe2} + xa_{CuGaSe2}, \qquad 2.1)$$

$$c_{CuIn1-xGaxSe2} = (1 - x)c_{CuInSe2} + xc_{CuGaSe2}\ . \qquad (2.2)$$

Figure 2.6 (A) shows the relationship between the tetragonal $Cu(In_{1-x}, Ga_x)Se2$ lattice parameters (a and c) and the amount of Ga. It was observed that the unit cell parameters decrease linearly with increasing gallium amount, due to the different bond lengths between ionic bonds In-Se (2,598 Å) and Ga-Se (2,417 Å) result of the difference in ionic radius between In^{+3} (0.62 Å) and Ga^{+3}(0.47 Å), as shown in Figure 2.6(B) [63][64].

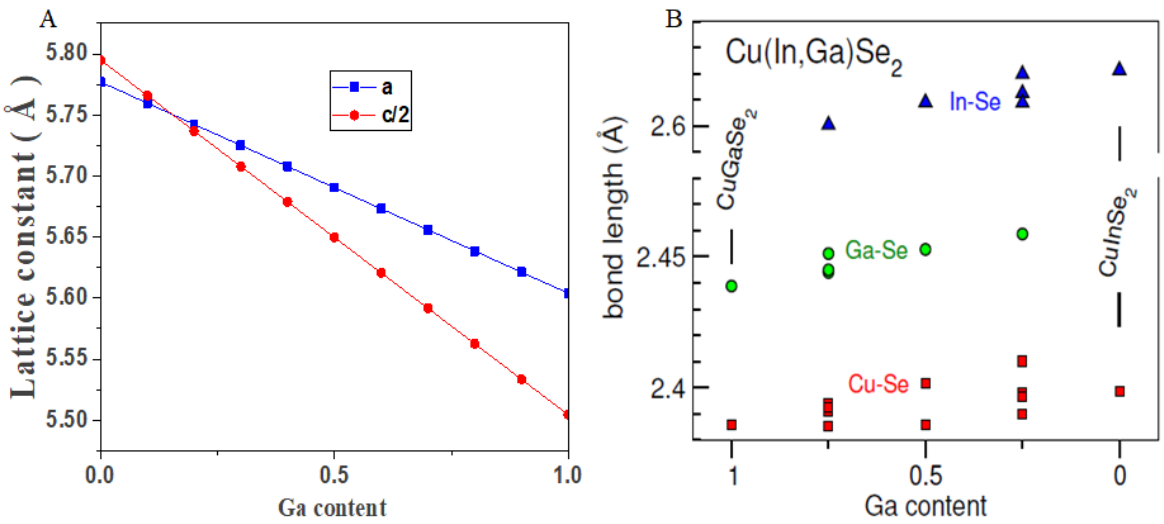

Figure 2.6: (a) Variation of lattice parameters a and half of c and (b) Element-specific In-Se , Ga-Se and Cu-Se bond lengths as a function of Ga content [65] .

B- CIGS phase diagram

According to the deposition conditions of the absorber layer, especially the deposition temperature and the chemical composition, different phases can be formed in addition to the α phase which is the chalcopyrite phase which results in p-type CIGS used for the highest efficiency CIGS thin-film solar, which in addition has a similar structure like β-$Cu(In_{1-x}, Ga_x)_3Se_5$ and δ-phase $Cu(In_{1-x}, Ga_x)_3Se_8$ are n-type. Other phases like Cu_2Se are n-type as well.

B- 1 $Cu_2Se - X_2Se_3$ ternary phase diagram

Figure 2.7 (a) shows an equilibrium phase diagram of the Cu-X-Se ternary system, the most probable formed phases are located in the pseudo-binary tie-line between Cu_2Se and X_2Se_3.

Figure 2.7 (b) and (c) show the temperature-composition phase diagrams for pure In and pure Ga compounds. In the Cu_2Se-In_2Se_3 pseudo-binary system in figure 2.7(b), observed phases are indicated as a function of composition and growth temperature: α phase is the chalcopyrite, β order defect compound (ODC) phases, δ is the sphalerite and γ phase. α single-phase $CuInSe_2$ exists between 22 to 24 at. % Cu at the growth temperature above 700 °C. Substitution of indium by gallium widens the α phase region thus making it possible

to have α-single phase formation between 20-25 at. % Cu at room temperature in the Cu_2Se-Ga_2Se_3 pseudo-binary system, as shown in Figure 2.7(b) and (c). In the Cu-rich side of both pseudo-binary systems, two-phase mixture α and Cu_2Se forms. Cu_2Se phase is highly conductive in nature and its presence on the CIGS surface reduces the efficiency of the solar cell. In the other hand, in the Cu-poor side we find mixture of α+ β, β + γ and + stages (δ phase being found only at high temperatures).

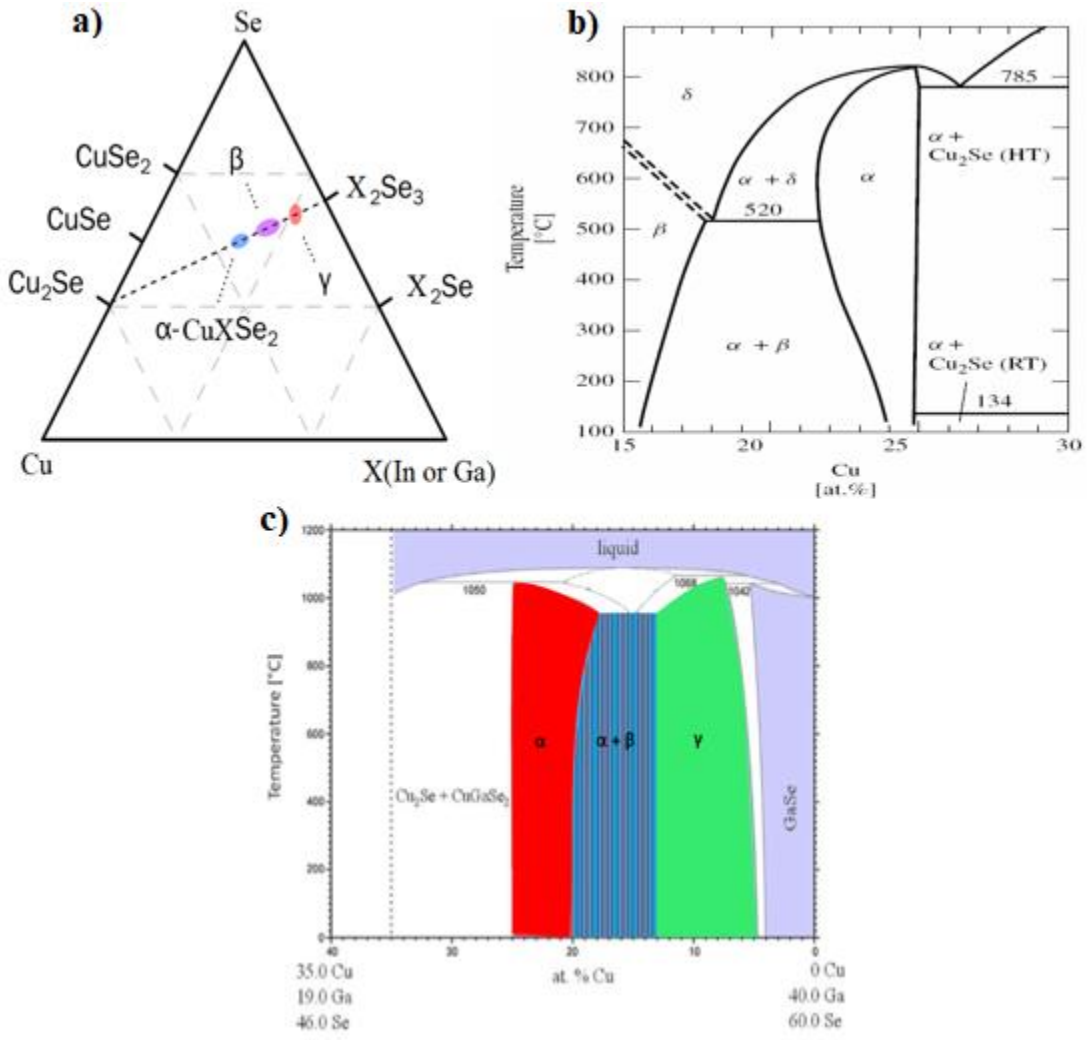

Figure 2.7: Phase diagrams of the (a) Cu-X-Se ternary system, (b) phase equilibria diagrams of Cu_2Se-In_2Se_3 and (c) Cu_2Se-Ga_2Se_3 pseudo-binary systems [66][67] [68] .

B-2 The quaternary CIGS compound

The pseudo-ternary phase diagram of the Cu_2Se-Ga_2Se_3-In_2Se_3system shown in figure 2.8 (a), correspond to the general formulation of $Cu_{1-z}(In_{1-x}Ga_x)_{1+z/3}Se_2$. The red line which connects the binary compounds Cu_2Se and In_2Se_3 represent the $Cu(In_{1-x}, Ga_x)Se_2$, where the α –phase $Cu(In, Ga)Se_2$ is the most relevant one for PV application. Figure 2.8 (b) shows the main Cu-poor and Cu-rich CIGS phases and secondary phases that can be created. The width of the chalcopyrite single-phase region is increased with increasing gallium rate and/or doping with Na, which can be seen in a clearer way in Figure 1.8 (b) [69].

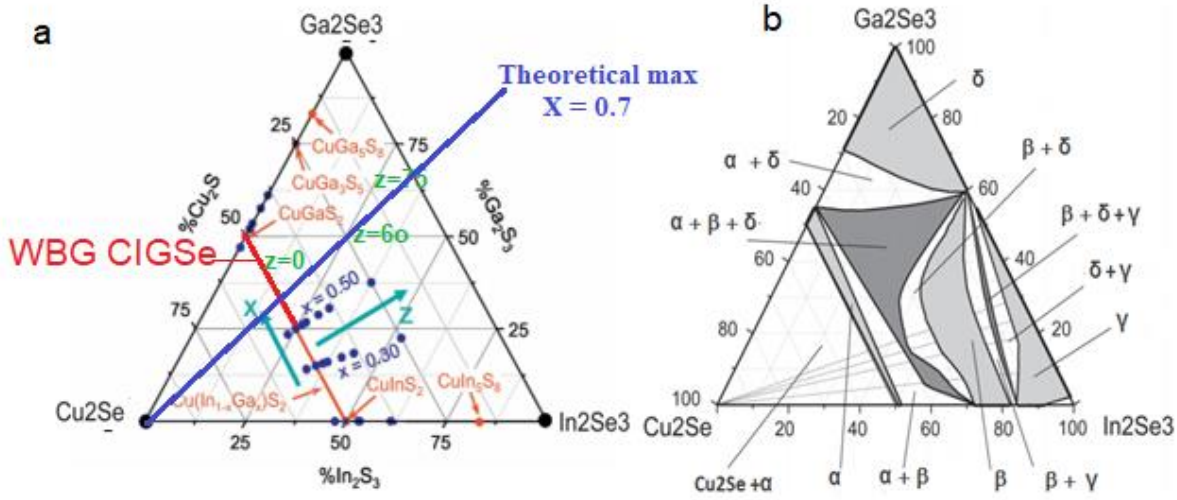

Figure 2.8: (a) $CuInGaSe_2$ quaternary phase diagram. (b) Pseudo-ternary phase diagram for CuInGaSe2 at room temperature [70] [69].

C- Opto-electrical properties.

$CuInGaSe_2$ is a direct band gap material with high optical absorption coefficient (~10^5 cm^{-1} for 1.5 eV), which makes it one of the most promising thin film solar cell materials, as only 1–2 µm is enough to absorb most of the light above the band gap from the solar spectrum [71]. Figure 2.9 shows the optical absorption coefficient of $Cu(In_{1-x},Ga_x)Se_2$ materials as a function of x. Figure 2.9 presents the variation of the absorption coefficient α with the photon energy (hv) for the various polycrystalline $Cu(In_{1-x},Ga_x)Se_2$ films. The figure depicts

that the all the $Cu(In_{1-x},Ga_x)Se_2$ films exhibited a high absorption coefficient and the absorption coefficient decreased with increase in the gallium content.

$$\alpha = \frac{4\pi k}{\lambda} \qquad 2.3)$$

$$\alpha\,(cm^{-1}) = \frac{4\pi k.E(eV)}{1239.8}\,.10^7 \qquad 2.4)$$

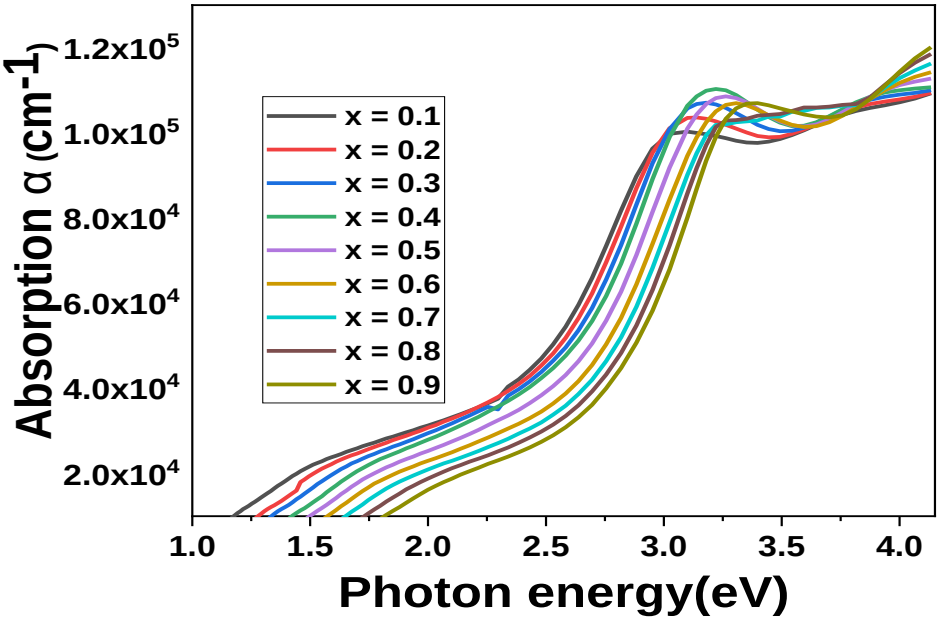

Figure 2.9: Absorption coefficient of various gallium content CIGS materials, the optical constants are extracted from [72].

One of the most interesting properties of CIGS material absorbers is the possibility to tune its bandgap by substituting In by Ga or Se by S as it is schematized in Figure 2.10, which can be optimized to match the solar spectrum by controlling the compositional ratios and providing high light absorption [73]. The variation of the bandgap with the In to Ga ratio, can be expressed as follow:

$$E_{g.CIGS}(eV) = 1..01(1-x) + 1.65x - 0.15x(1-x) \quad 2.5)$$

Where x = [Ga]/[In+Ga] represents the Ga content of CIGS, and b is an empirical constant b = 0.15-0.24 eV [74].

Figure 2.10 shows the high flexibility in the optical properties of $Cu(In_{1-x}, Ga_x)(S_{1-y}, Se_y)_2$ compounds by substituting indium with gallium or/and substituting selenium with sulfur , e.g. the band gap varies from 1.0 eV ($CuInSe_2$) to 1.68 eV ($CuGaSe_2$) and from 1.53 eV ($CuInS_2$) to 2.5 eV ($CuGaS_2$), Incorporation of Ga leads to an increase in the conduction band (CB) level without changing the valence band (VB) level. Incorporation of S has an impact on both the CB and VB levels, the VB change is somewhat larger than the CB change [75]. According to the detailed balance limit, the optimal band gap energy for single-junction cells is in the range of 1.1 - 1.4 eV. The band gap energy of the record CIGS solar cell is around 1.08 eV.

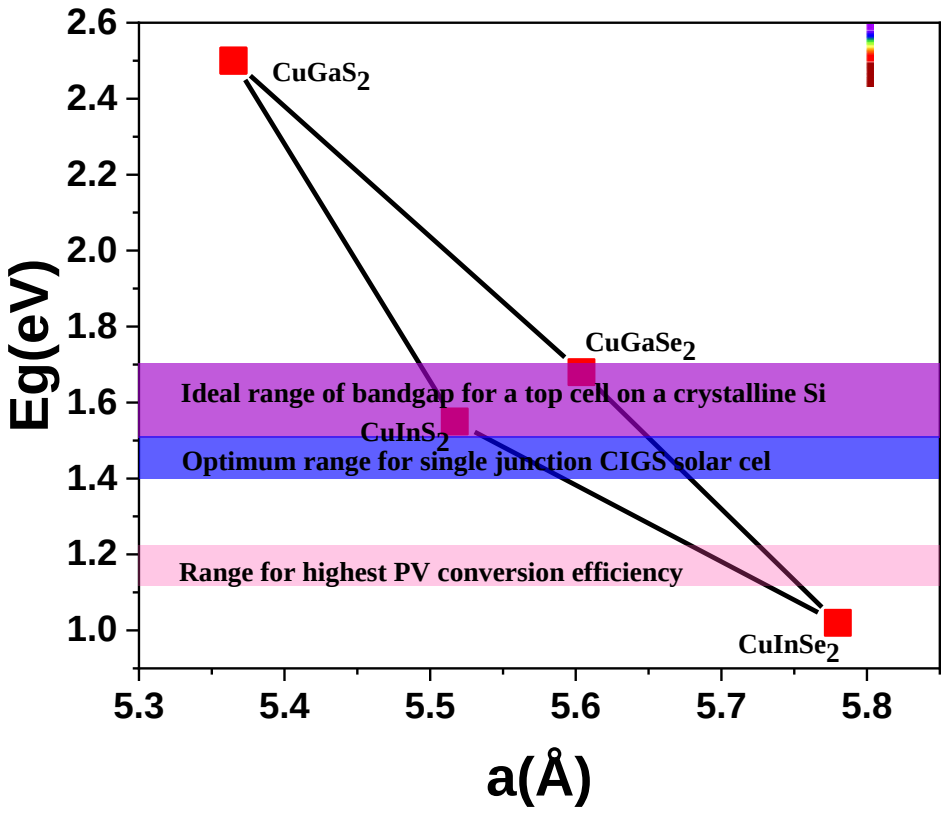

Figure 2.10: Band gap energies versus lattice constant a in the CIGSSe system.

D- Defects in CIGS

The CIGS electrical properties strongly depend on the presence of intrinsic defects in the structure, such as vacancies, interstitials and antisites ones. If we consider vacancies, antisites and interstitial sites for all of the constituent atoms of CIGS we find 20 possible intrinsic defects. Table 2.2 summarizes the most relevant intrinsic defects in CIGS with their formation energies [17]. From the defect formation energies V_{Cu}^{-} , V_{In}^{-3} and V_{Ga}^{-3} are shallow acceptors, while that In_{Cu}^{+2} and Ga_{Cu}^{+2} act as shallow donors.

Table 2.2: The defects in the CIGS compounds and their electronic character [76].

	Defect	**Electronic character type**	**Formation energy eV**
Vacancies	V_{cu}	Acceptor	2.6
	V_{In}	Acceptor	2.8
	V_{Ga}	Acceptor	2,8
	V_{Se}	Donor	2.4
Interstitial	Cu_i	Donor	4.4
	In_i	Donor	9.1
	Ga_i	Donor	3.0
	Se_i	Acceptor	22.4
Antisite	Cu_{in}	Acceptor	1.5
	Cu_{Ga}	Acceptor	1.4
	In_{cu}	Donor	1.4
	Ga_{cu}	Donor	1.9
	Cu_{Se}	Acceptor	7.5
	Se_{Cu}	Donor	7.5
	In_{Se}	Acceptor	5.0
	Se_{In}	Donor	5.5

V_{Cu}^{-} is the dominant defect in p-type material, which in the right amount can create a carrier density of the order of 10^{16} cm^{-1} . On the contrary Se vacancy (V_{Se}^{+2}) and In_{Cu} and Ga_{Cu} antisites act as donor defects. One peculiarity of CIGS system is that the formation of electrical neutral defect complexes such as $2V_{Cu}^{-} + In_{Cu}^{+2}$ or $2V_{Cu}^{-} + Ga_{Cu}^{+2}$ is possible, which can lead to a self-compensation effect, rendering donor defects less active. In terms of possible compositional regime, and according to the Cu⁄In and Se⁄(Cu+In) ratios, the $CuInGaSe_2$ material can be synthesized either under Cu-rich or In-rich conditions. The Cu-rich material is highly conductive; mainly due to the presence of copper selenide phases ($Cu_{2-x}Se$) at the surface, the defects related to Cu rich compositions like Cu_{III} *or* Cu_i are deep defects which will degrade the electronic quality of the crystal [77]. The In-rich material has a n-type conductivity, and when the material becomes very In-rich the formation of OVC compounds is possible. It is important to notice that selenium excess in the absorber layer is necessary in order to avoid selenium deficiency and in consequence the formation of very detrimental V_{Se}, also the material formed under Cu-rich composition and Se vacancy (V_{Se}^{+2}) since the V_{Se}^{+2} and Cu interstitial Cu_i defects act as donors has a n-type conductivity. Tables 2.3 and 3.3 show defect activation energies and transition energy, respectively. in CIS and CGS.

Table 2.3: Defect activation energies in $CuInSe_2$ and $CuGaSe_2$ [48].

Defects	Charge state	$CuGaSe_2$ (M=Ga)	$CuInSe_2$ (M=In)
$\mathbf{V_{Cu}}$	(-/0)	$E_v + 0.01$	$E_v + 0.03$
V_M	(-/0)	$E_v + 0.19$	$E_v + 0.17$
V_M	(2-/-)	$E_v + 0.38$	$E_v + 0.41$
V_M	(3-/2-)	$E_v + 0.66$	$E_v + 0.67$
Cu_M	(-/0)	$E_v + 0.29$	$E_v + 0.29$
Cu_M	(2-/-)	$E_v + 0.61$	$E_v + 0.58$
$\mathbf{M_{Cu}}$	(0/+)	E_c - 0.49	E_c - 0.25
$\mathbf{M_{Cu}}$	(+/2+)	E_c - 0.69	E_c - 0.34
Cu_i	(0/+)	E_c - 0.21	E_c - 0.20

Table 2.4: Charge transition levels (eV) above the valance band maximum[48].

$CuInSe_2$	Transition energy (eV)	$CuGaSe_2$	Transition energy (eV)
$\mathbf{V_{Cu}}$	shallow	$\mathbf{V_{Cu}}$	shallow
$\mathbf{In_{Cu}}$	shallow	$\mathbf{In_{Cu}}$	shallow
$\mathbf{Ga_{Cu}}$	shallow	$\mathbf{Ga_{Cu}}$	1.26 (+2/+1), 1.33 (+1/0)
$\mathbf{Cu_{In}}$	0.14 (0/-1), 0.62 (-1/-2)	$\mathbf{Cu_{Ga}}$	0.20 (0/-1), 0.75 (-1/-2)
$\mathbf{Cu_i}$	shallow	$\mathbf{Cu_i}$	shallow
V_{Se}	0.08 (+2/0), 0.98 (0/-1)	V_{Se}	0.34 (+2/0), 1.26 (0/-1), 1.66 (-1/-2)
V_{In}	0.03 (0/-1), 0.42 (-1/-2)	V_{Ga}	0.01 (0/-1), 0.34 (-1/-2)
V_{In}	0.69 (-2/-3)	V_{Ga}	0.82 (-2/-3)
In_i	0.34 (+3/+2), 0.48 (+2/+1)	Ga_i	0.05 (+3/+2), 0.39 (+2/+1)
Se_i	0.19 (+2/+1), 0.20 (+1/0)	Se_i	0.15 (+2/+1), 0.48, (+1/0),
Se_i	0.64 (0/-1)	Se_i	1.08 (0/-1), 1.32 (-1/-2)

Effect of Ga content on the defect's levels

Figure 2.11, Shows the defects energies evolution in CIGS by increasing gallium content. The depth of Ga_{Cu}^{+2} compared to In_{Cu}^{+2} is considered one of the cause of the open-circuit voltage loss for wide band gap CIGS [78] and act as a recombination center in Ga rich CIGS [79] [80] [81].

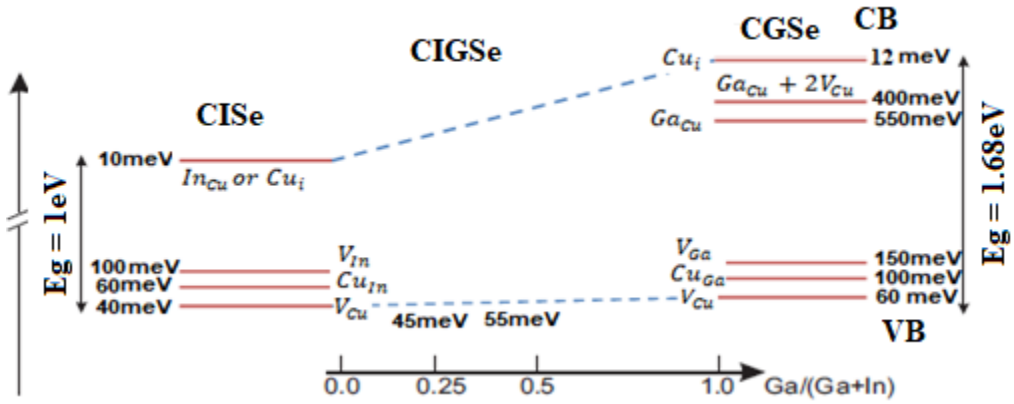

Figure 2.11: Defect model for Cu(In,Ga)Se₂.

Effect of copper content

The copper content (Cu/III) has a strong influence on the microstructure, optical, and electronic properties of CIGS films. Chalcopyrite phase is well known for accommodating large stoichiometric deviations, in particular large Cu-concentration variations, and can exist in Cu-poor CIG <1, Cu-stoichiometric CIG = 1 and Cu-rich CIG > 1 regime. The Cu content undergoes various phase compositional changes of the CIGS material microstructure. With CIG ratios below 1.0, the chalcopyrite phase can coexist with the OVC compounds depending on the Cu content. For CIG above 1.0, it has been widely reported the presence of Cu2-xSe secondary phases, which use to exhibit a relatively low melting point (< 500 ºC), and then can promote the growth of large grains in CIGS [82].

The Cu-rich CIGS absorber materials show better semiconductor properties with lower defect concentrations and better transport properties. On the contrary, Cu-poor composition show higher defects densities and lower mobility. Furthermore, Cu-rich CIGS based solar cell achieves higher open circuit voltages than Cu-poor ones, predicted by the observation of larger splitting of quasi-Fermi level. In spite of the better potential of Cu-rich absorbers, the performance of Cu-rich devices is always inferior compared with Cu-poor devices. The main reason for the lower performance of Cu-rich devices is the recombination at or near the interface in the device. The electrical properties of wide band gap CIGS are extremely sensitive to the Cu content of the absorber [83] [79].

As shown in Figure 2.12, in CIGS materials the valence and conduction band vary with the CIG and GGI rates, the valence band depends on Cu content as derived from the cation (Cu 3d) and anion (Se 4p) states, whereas the conduction band depends on the III element In 5s and Se 4p states in the CISe as shown in figure 2.12(b) and Ga 4s and Se 4p states in CGSe as shown in figure 2.12 (a). This means that a variation in the Cu concentration would influence the position of the E_V and thus the band gap energy Eg. The strong repulsion of the (Cu 3d) and (Se 4p) orbitals pushes the valence band maximum towards the conduction band and results in a lower band gap energy. Therefore, a reduction of the Cu content leads

to an increase in Eg by lowering the p-d repulsion. As a result, the CIGS compounds with a high amount of Cu vacancies V_{Cu}^{-} exhibit a higher band gap energy [84].

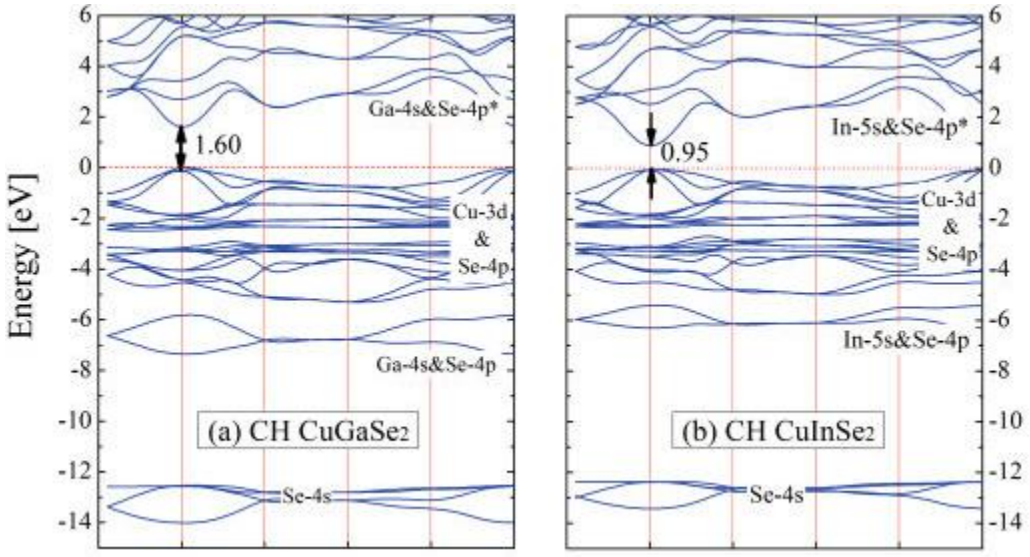

Figure 2.12: Band structures of (a) $CuGaSe_2$, (b) $CuInSe_2$.

Among all these possible compositional regimes, the highest efficiency CIGS solar cells are always fabricated under Cu-poor composition. In particular, the high efficiency obtained with Cu-poor material is due among others to the low recombination at the CIGS/CdS interface. By contrast in Cu-rich CIGS, higher recombination rates and the formation of $Cu_{2-x}Se$ secondary phases on the surface with is highly conductive, degrade the cell performance [85].

2.4 Deposition methods

The deposition method has a significant impact on the film properties as well as on the production costs of solar cells. CIGS absorbers have been widely fabricated by various methods vacuum and non-vacuum [86][66]. Nevertheless, high efficiency CIGS solar cells are mainly based on vacuum methods. A wide range of vacuum methods have been employed to fabricate CIGS films. Table 2.3 summarize various methods used for the fabrication of CIGS films, and their advantages and disadvantages.

Table 2.5: List of various methods used for the preparation of CIGS films, and their advantages and disadvantages [87].

Methods	Advantages	Disadvantages
Co-evaporation	Well established technique for lab-scale devices	Simultaneous control of sources is difficult and results in variation in stoichiometry, poor reproducibility and uniformity over large area
Sputtering	Controlled deposition rate and better crystallinity	High operational cost, produces multiple phases, *viz.* CIS, CGS
Selenization/sulfurization	Large area deposition, established technique can be used for precursor deposition and reaction	Toxic gases (H_2Se), additional processing step is required, poor adhesion with back contact
Electrodeposition	Low cost method, room temperature deposition	Process optimization is difficult
Screen printing	Little material wastage, high packing density, high throughput	Control of Ga profile is not possible, while drying, phase segregation and inhomogeneities occur
Spray coating	Scalable, high throughput and low cost	Precursor material wastage during spray coating
Spin-coating	Film uniformity (lab-scale), cost of equipment is low, easy operation	No uniformity over a large area, material wastage, roll-to-roll incompatible
Doctor's blade	Less material wastage, roll-to-roll compatible, better stoichiometric control	Solvent evaporation is slow which leads to accumulation
MBE	Minimum contamination due to ultra-high vacuum deposition, this method is good for basic studies such as defect studies and phase segregation	Large area deposition has not been reported, high efficiency not reported
MOCVD	Useful for basic studies, growth rate is faster than MBE	Not suitable for industrial processes, large area growth is not reported, process is not as abrupt as MBE
Electron beam deposition	Good stoichiometry and film purity	Large area deposition not reported, not compatible with industrial processes
Pulsed laser deposition	Target composition can be transferred to films and yield good stoichiometry in the film, CuSe binary phase can be avoided	Not suitable for large area, large area stoichiometry has not been reported
Inkjet printing	Mask-less patterning simplifies processing steps, compatible for roll-to-roll technology	Low efficiency

Among all these previous methods, there are only two dominant methods both at the laboratory scale and at the large scale, for high efficiency cells, co-evaporation and sequential processes [87][88] [89][90].

2-4-1 Co-evaporation process

Co-evaporation process is the most commonly technique used to fabricate high-quality CIGS-based thin films [66][91]. Several record efficiencies for CIGS solar cell have been achieved with this process, by NREL with 19.9% [92], ZSW with 20.3% [93] and NREL with 20.8% [94]. This technique is based on simultaneous evaporation of the elements copper, indium, gallium and selenium onto a heated substrate in a high-vacuum chamber prepared by coevaporation from elemental sources, the process requiring a substrate temperature of 550°C [95]. The atomic CIG and GGI ratios are determined by evaporation rates and deposition times. Based on the flow distribution of constituent elements different co-evaporation processes are encountered:

I) Single-stage: This is the easiest process, the constituent elements Cu, In, Ga and Se being evaporated at constant evaporation rates at the same time. CIGS films deposited by this method are always Cu-poor. A schematic representation of this process is given in figure 2.13 (A).

II) Two stage: called also (bilayer process or Boeing process) [96]. It consists on a Cu-rich growth in the first stage and a Cu-poor growth in the second stage. A schematic representation of this process is given in figure 2.13 (B).

III) 3-Stage Process: The record efficiency CIGS devices fabricated by co-evaporation have been obtained with the three-stage process, where in the first and third stages In and Ga elements are evaporated, and Cu is evaporated in the second stage. This allows to control the composition by changing the element flux during the deposition of the absorber [66], leading to the formation of a grading of the band gap along the thickness, by varying the ratio of the Ga/In during the process and considered to be the main driver of high production costs [97][98]. A schematic representation of this process is given in figure 2.13 (C).

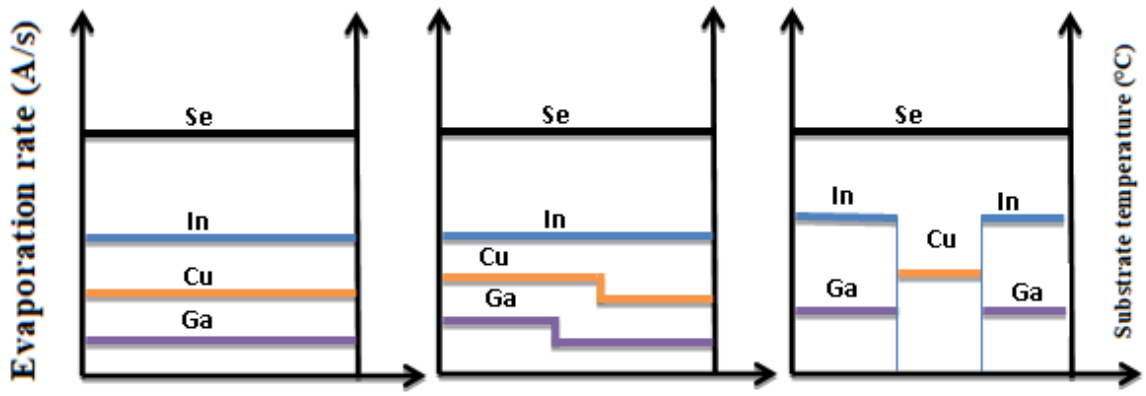

Figure 2.13: Various types of co-evaporation processes [90].

2- 4-2 Sequential processes

several records efficiencies for CIGS have been reached by two step process, e.g., current record reached by Solar Frontier 23.35% [42]. The two steps are the deposition of the precursor followed by selenization.

The first step is the metallic precursor copper, indium and gallium (CuInGa) at room temperature, several vacuum and no-vacuum processes have been demonstrated including sputtering, electron beam evaporation, screen printing, thermal evaporation and electrodeposition. However, the most common technique is sputtering or thermal evaporator. Then secondly, this precursor is annealed at high temperature under Se or S atmosphere using quartz tubular furnace or rapid thermal processing (RTP) system to form the quaternary Cu(In,Ga)Se_2 film. An alternative approach is, depositing Se on top of the precursor, followed by an annealing step [99] [100].

The advantages of this method are low-cost high-throughput production of CIGS solar cells and suitability for large area scalability [101][96]. Figure 2.14 shows the deposition methods that have been used in the manufacture of CIGS solar cell and which have allowed reaching several records [92] [102] [103] [104] [105] [42].

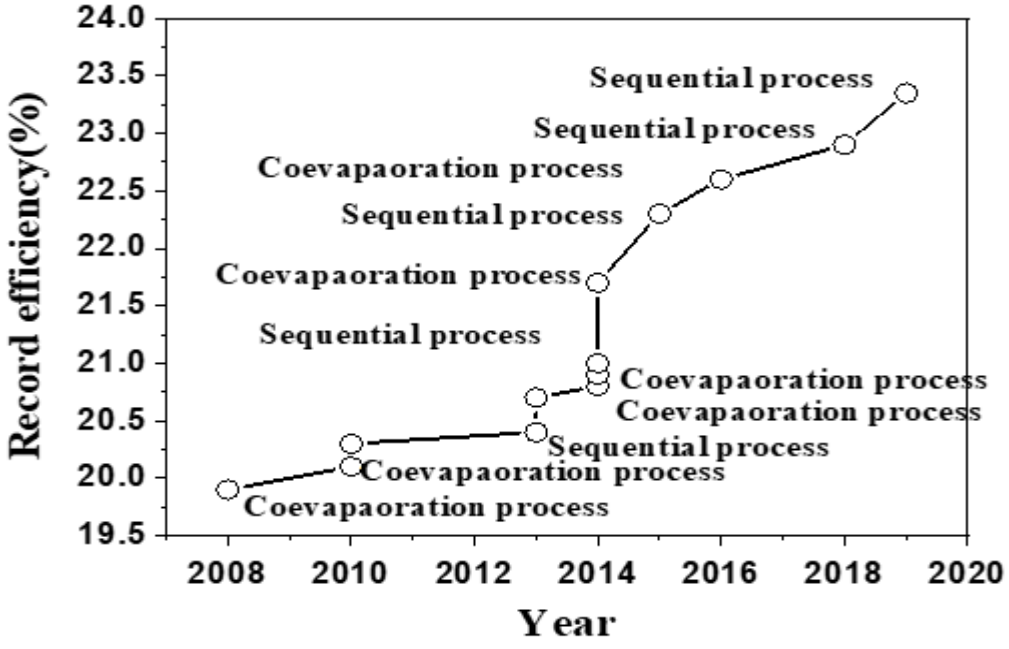

Figure 2.14: Deposition methods of the cells reaches the latest record efficiencies of CIGS [106].

2.5 Evaluation of different buffer materials for Ga rich CIGS solar cells

Recombination at the absorber/buffer layer interface is considered as one of the main factors limiting the performance of the Ga-rich CIGS device[106] [107]. Ga rich CIGS absorber requires a wider bandgap buffer layer than CdS to maximize photons reaching the absorber layer especially at short wavelengths, to avoid undesirable absorption of the solar spectrum, and to get a good band alignment with the absorber. Improving the electronic properties of interfaces formed in a solar cell and regions close to the interfaces represents a key aspect of the strategy to achieve high GR-CIGS solar cells efficiency.

In 1974, Bell Laboratory fabricated the first $CuInSe_2$ thin-film solar cells, using a Cadmium - sulfide (CdS) buffer layer deposited by evaporation [108]. Since that date, the fabrcation of CIGS TFSCs require a buffer layer to address problems related to the bandgap difference between the CIGS absorber layer and the TCO window layer [109][110]. The Buffer layers widely used in CIGS solar cell is a thin CdS layer deposited by chemical bath deposition (CBD) at both the laboratory and industrial scale, owing to the good conduction band alignment both to absorber material and window layer, low interface recombination, high resistivity, good device stability [111][109]. Several alternative buffer materials and deposition techniques have been investigated. Among the commonly used buffer layer materials, ZnS has been investigated extensively owing to its low cost, non-toxicity, and good transparency at short wavelengths [112]. The current record CIGS solar cell with 23.35% efficiency has been achieved through the use of a Cd-free buffer layer $Zn(O,S,OH)/Zn_{0.8}Mg_{0.2}O$ [85]. Table 2.4 shows the buffer layers that have been used in the record solar cells and the deposition method.

Table 2.6 : list of buffer layers that have been used in the record solar cells and the deposition method.

Buffer layer	Deposition technique	Efficiency (%)	V_{OC} (mV)	J_{SC} (mA/cm^2)	FF (%)	Ref
Zn(O,S,OH)/$Zn_{0.8}Mg_{0.2}O$	CBD/ALD	23.3	734	39.6	80.4	[42]
CdS	CBD	22.9	746	38.5	79.7	[85]
Zn(O,S,OH)x	CBD	22.0	717	39.4	77.9	[113]
ZnSnO	ALD	14.7	666	31.7	69.3	[103]
Zn(O,S)	CBD	21.0	717	37.2	78.6	[114]
ZnS	CBD	18.1	671	34.9	77.6	[115]
ZnSe	CBD	15.7	570	35.2	72.3	[116]
$Zn_{1-X}Mg_XO$	Sputtering	16.2	632	37.6	68.1	[117]
In_2S_3	ALD	18.1	668	35.7	75.7	[114]
Zn(O,S,OH)x	Sputtering	19.7	683	37.1	77.8	[118]
CdS	Co-evaporation	20.3	740	35.4	77.5	-
Zn(O,S)	ALD	18.5	689	35.5	75.7	[119]
In_2S_3: Sn^{4+}	Spraying	14.5	660	29.7	73.8	[120]
In_2S_3	Evaporation	17.1	655	34.8	74.9	[121]
$Zn_{0.8}Mg_{0.2}O$	ALD	16.4	624	35.4	74	[122]

Band alignment of Ga rich CIGS/ buffer layer interface

CIGS/buffer layer interface is critical for the minority carrier's transport. Therefore, the band alignment of wide bad gap CIGS/Buffer layer interface has a strong effect on CIGS device efficiency. As shown in Figure 2.15, there is always a discontinuity in the conduction band (ΔE_C) at the CIGS/buffer layer interface.

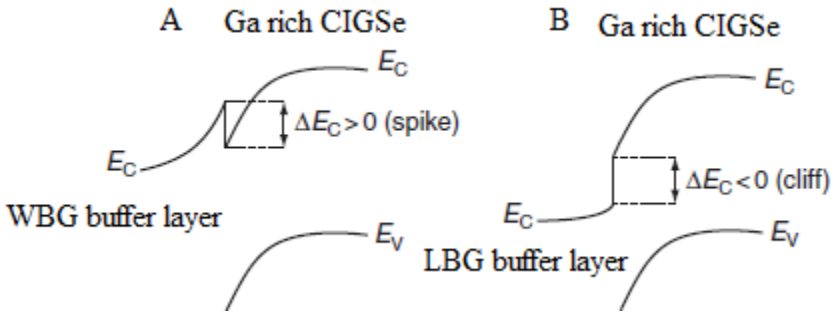

Figure 2.15: Band diagram of a CIGSe-based thin film solar cell. (A) Spike for ΔEC >0, (B) cliff for ΔEC <0.

In the CIGS/buffer layer interface, if the conduction band minimum of the buffer layer is higher than that of CIGS absorber a spike conduction band offset is formed in CIGS/CdS interface, this band structure being the most efficient standard CIGS solar cell. In the spike structure the optimal conduction band offset (ΔE_c) can range from 0.1 to 0.4 eV [123]. If the spike exceeds 0.4 eV, a barrier is formed which inhibits the transport of electrons from the CIGS absorbers to the buffer layers in the other hand, when the conduction band minimum (CBM) of the CIGS absorber is lower than that of buffer layer a cliff structure is formed. The conduction band offset (CBO) can be estimated by [124]:

$$CBO = \chi_{Absorber} - \chi_{Buffer\ layer} \quad 2.6)$$

The following equation calculating electronic affinity of $CuIn_{1-x}Ga_xSe_2$ as functions of x. Figure 2.16 shows allows the variation of electronic affinity as a function of Ga content.

$$\chi e = 4.61 - 1.162x + 0.034x^2 \quad 2.7)$$

The electronic affinity decreases as the gallium content increases.

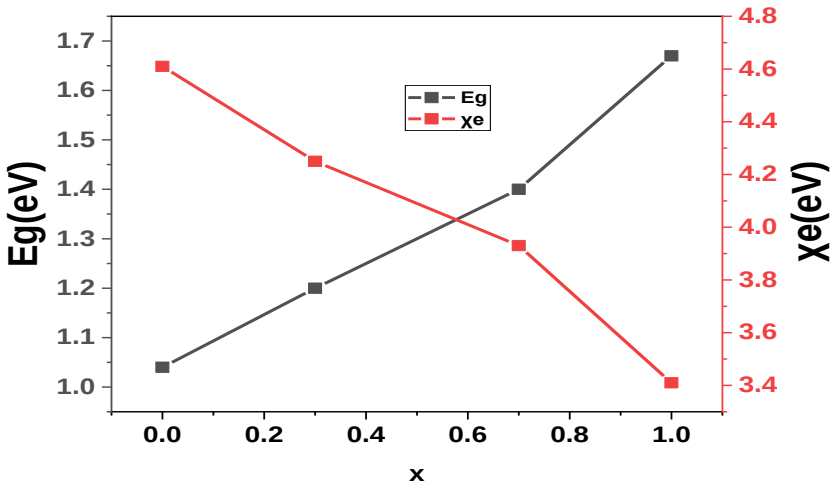

Figure 2.16: Electronic affinity of CIGS as a function of Ga content.

Figure 2.17 shows the conduction band offset at the buffer layer/CIGS interface for four buffer layers as a function of Ga content in CIGS absorber, when the gallium content is less than 0.35 the CBO is spike for all buffer layers except In_2S_3 buffer layer, and the resulting

electron barrier is too large to allow any significant current flow. In the opposite direction, high gallium content produces a cliff structure. The green box in figure 2.17 where the optimal CBO (between 0.1 and 0.4 eV) is also shown. For Ga rich CIGS it is less than the optimal values, thus implying that the GR-CIGS needs a buffer layer having a greater bandgap than the bandgap of the tested buffer layers.

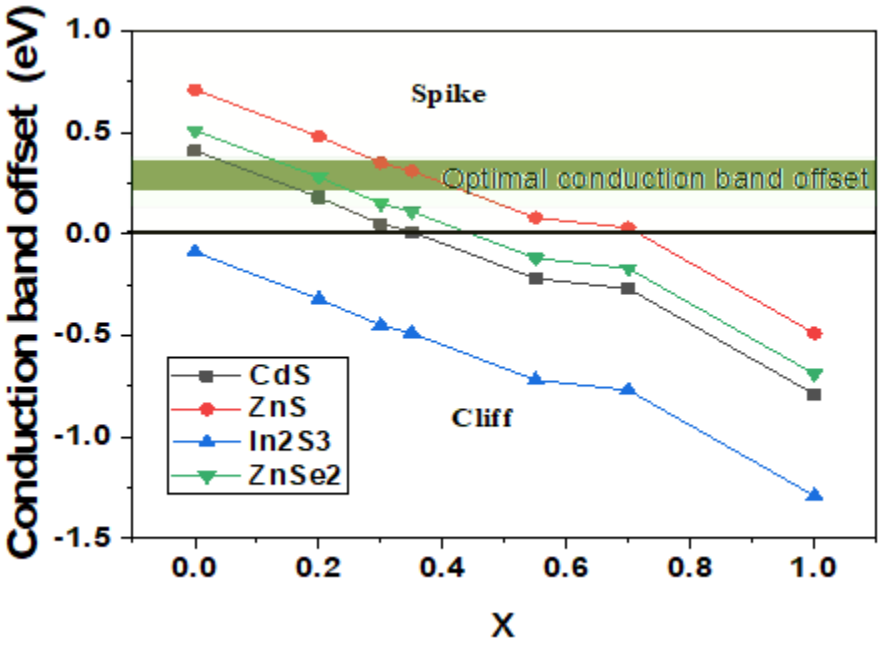

Figure 2.17: Conduction band offset of CIGS as a function of Ga content.

2.6 Window layer

Transparent front contact, called the window layer, needs to be both transparent to the photons in the convertible energy range (400-1300 nm), and conductive enough (i.e., with low electrical resistance) to permit the photocurrent generated to the external circuit with a minimal loss. This window layer typically consists of a transparent conductive oxide (TCO) which has a high band gap over 3.3 eV, a small thickness, and a low series resistance. Various transparent conducting oxides (TCO) films are used as window layers in CIGS thin film solar cells, ITO and AZO being the most common transparent ones used for CIGS.

2.7 Performance limitations in Ga-rich CIGS-based solar cells

Ga-rich CIGS devices have consistently underperformed that the Ga-poor ones (GGI ≤0.4). Several factors are considered responsible for this difference. Based on the preceding discussion, the most important factors are:

- Recombination due to deeper defects: in Ga-rich CIGS materials, the defect level such as Ga_{Cu} is located around the middle of the band gap, this results in a significant bulk recombination. The bulk recombination defects result in lower carrier concentration, reduction of Voc and FF, and consequently lower PCE.
- Discontinuity in the conduction band (ΔEc) increases as the gallium content increase from a small spike to a cliff which increases the recombination at absorber/buffer layer interface and its impact on device performance.
- Difficulty to control the Ga profile due to the faster reaction of indium with Se than gallium with Se, leads to accumulation of gallium at the backside of the CIGS absorber increasing the recombination at back interface and decrease the band gap at the absorber surface, thus the open circuit voltage does not increase in proportion to increasing gallium content as required.
- In addition to the above factors, we can also mention: decrease of the unit cell parameters linearly with increasing gallium amount, reduction in the depletion region.

2.8 Strategies for high efficiency CIGS solar cells

One of the main goals of worldwide photovoltaic research is to develop high efficiency solar cells while reducing production costs. For chalcopyrite thin film technology, the efficiency has increased dramatically, from 9% In the 1980s to over 23% today. Several strategies have been used to achieve this current record efficiency. Basically, nine approaches to improve the efficiency of chalcopyrite -based TFSCs can be encountered. Figure 2.18 summarizes them with the reached record efficiency associated to these different steps.

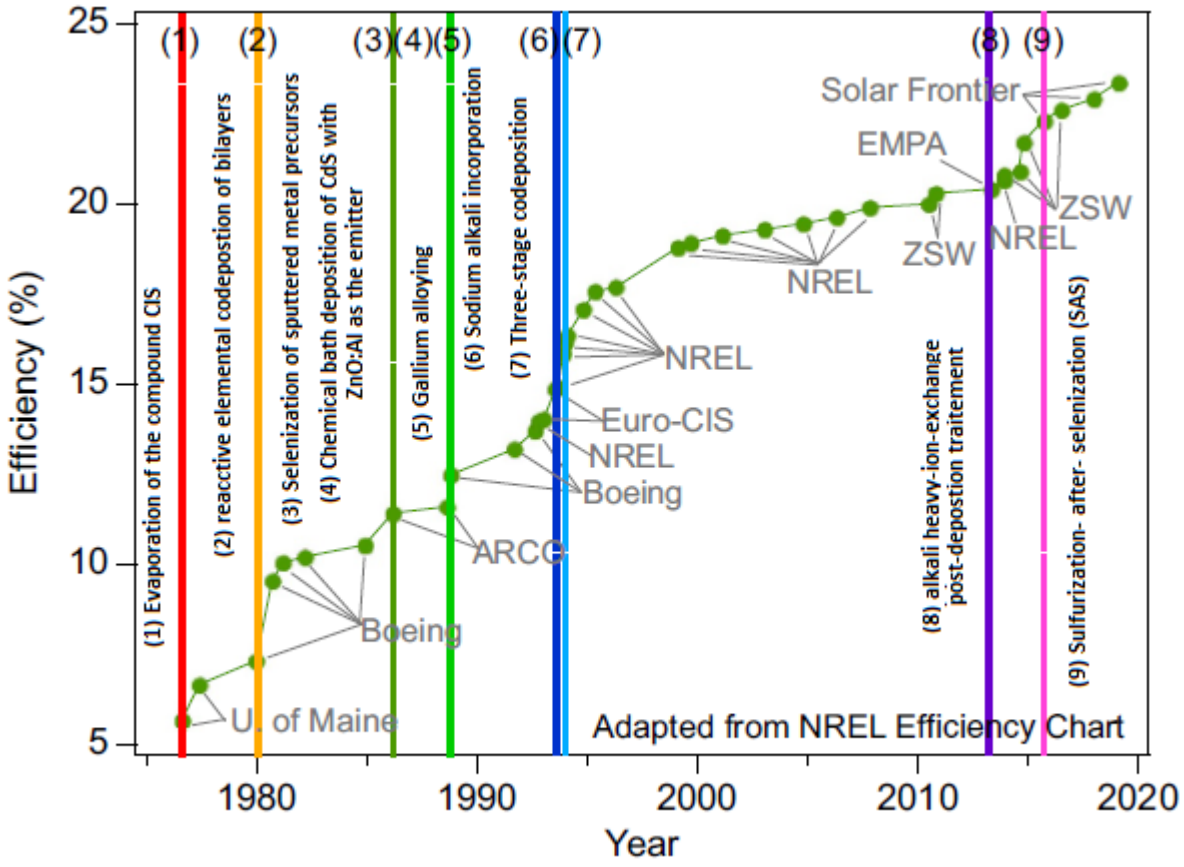

Figure 2.18: Annotated history of record CIGS cell efficiencies and key innovations [24].

Among the strategies that made CIGS one of the best thin-film solar cells over the past decades, gallium alloying, alkali (mainly sodium) incorporation, graded (both with Ga and S) band gap, and postdeposition treatment are the most effective in term of performance increase. In the following, a brief summary of each strategy is presented.

A- Band-gap grading in CIGS absorber layer

The first CIGS band gap grading was given by Contreras el al in 1993, by Ga-grading profile [36]. Since then, band gap grading at different depths of CIGS absorber film has been widely investigated in the CIGS community as an effective strategy to reduce the Voc deficit in single junction low band gap CIGS thin film solar cells. Band gap grading through the absorber film essentially affect the collection and recombination of photocarriers [125]. The Voc is mainly determined by the minimum bandgap. The Jsc also correlates with the minimum bandgap of the entire film. However, an excessive abrupt front grading will lower FF and Jsc because it acts as a barrier to prevent the minority carriers from diffusing into the buffer layer [98]. Figure 2.19 shows the profiles of composition and bandgap in the CuIn1-xGax(S1-ySey)2 absorber layer.

Therefore, three different band gap grading approaches in CIGS solar cells. Those include:

1- Uniform grading (UG)

2- Front grading, characterized by increasing the band gap towards the front surface.

3- Back grading called also back surface grading (BSG), characterized by increasing the band gap towards the back surface.

4- Double grading called also double sided grading (DSG), this is a bandgap U-shaped, created by increasing the band gap both towards back and front surfaces, leading to its minimum in between [126].

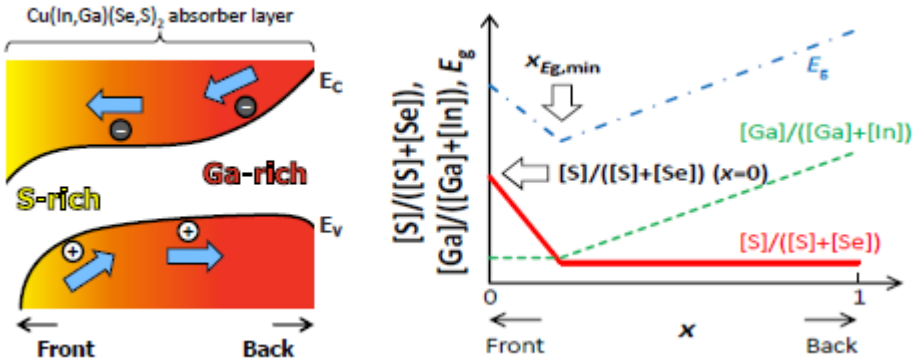

Figure 2.19: Schematic band diagram typically used for high efficiency graded CIGS with corresponding bandgap [113].

The main goal of back grading is to create a back surface field (BSF), helping decreasing the possible recombination at the back interface and pushes the minority carriers towards the space charge SCR. This improves the short circuit current density (Jsc). In the back graded CIGS absorber it has been reported that the optimum difference between the minimum band gap and the band gap close to the back interface ΔEg is in the range 0.2 - 0.4eV and the thickness of back grading in the range 0.1 - 0.5 µm. Front grading increase the Voc due to widening the band gap and lowering the valence band then repels the holes from the SCR and reduced interface recombination[127] [128][129]. Another advantage in the double graded absorber consists in the presence of a low-bandgap ('notch') region close to the front surface, enhancing the absorption of low energy photons [130] [41].

Several approaches have been employed to create a graded band gap in the CIGS absorber, based on the establishment of a compositional gradient absorber of Ga/In at different depths of absorber or S/Se by surface sulfurization of CIGS, as shown in Figure 2. 19 [131]. Gallium incorporation affects the level of the conduction band minimum [130] and sulfur incorporation affect the level of the valence band maximum. Multi-stage coevaporation process is the suitable deposition technique [132], which renders possible the control of the composition by modifying the flow of the elements during the deposition of the absorber.

B- Sodium incorporation

The beneficial effect of the sodium presence during the CIGS growth was first observed in 1993 by Hedström et al. [133], wherein they compared the growth of CIGS solar cells on SLG, borosilicate, sapphire, and alumina substrates [133]. They found that when grown on soda-lime glass substrate, higher CIGS device efficiencies (mainly due to the increase in FF and V_{OC}) were achieved than when grown on borosilicate substrate. This improvement was explained by the sodium diffusion from the substrate through the Mo back contact into the CIGS absorber layer. The amount of Na diffusion from SLG into CIGS absorber depends on the selenization conditions and the microstructure of the Mo back contact, and it has been estimated in the range of 10^{19}–10^{20} cm^{-3} [134][135]. In 1997, Granata et al. estimated the

optimal Na concentration in the CIGS absorber being of 0.1% [136]. A variety of external Na incorporation methods have since then been used, allowing to control the amount of Na being incorporated.

Methods for Na incorporation into CIGS absorber layer

Figure 2.21 shows the commonly alkali incorporation methods: pre-deposition, during co-evaporation, and post-deposition treatment.

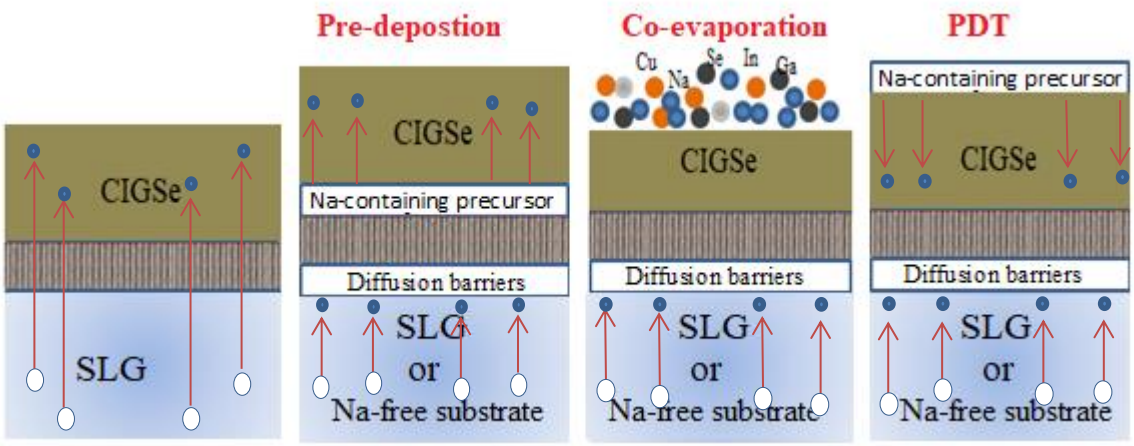

Figure 2.20: Schematic illustration of the most commonly used methods for Na incorporation into CIGS.

1- **Pre-deposition treatment:** among the advantages making SLG the most commonly used substrate to fabricate high efficiency CIGS device, Na diffusion from SLG through the Mo back contact into the CIGS absorber layer, during CIGS growth, is considered the easiest way to introduce it. However, for large area scale, the Na content inhomogeneity in SLG has a deteriorating effect on module efficiency. Several alternatives methods have thus been tested, consisting in using Na-free substrates such as borosilicate or SLG with diffusion barriers, like SiO_2, SiN_x, TiO_2, or Al_2O_3 to prevent Na diffusion from SLG to the CIGS absorber, and then deposit a thin Na-containing precursor (in form of NaF or even Na-doped Mo) prior to the CIGS growth), which allow controlling the Na amount at large area scale.

2- **Co-evaporation incorporation:** Incorporation of sodium in CIGS by co-evaporation method was first studied by Güttler et al. (2010), by evaporation of NaF during three stages

process onto SLG with Si_3N_4 sodium barrier and polyimide foils [137]. This method led to high efficiency devices [138].

3- Post-deposition incorporation: The PDT consists in the deposition of a thin layer of NaF onto CIGS absorber film, followed by an annealing in order to promote the Na diffusion into the CIGS. More details are given in the next section (3.3).

Effect of Na incorporation strategies on Cu(In,Ga)Se2 absorbers

Na effect in the CIGS absorber has been widely investigated and is well known as beneficial for the enhancement of crystal structure, electronic characteristics and photovoltaic device properties. The main effects of the Na incorporation into CIGS absorber include: (1) p-type conductivity improvement due to the increase in the carrier concentration attributed to suppression of antisite defects such as In_{Cu} and Ga_{Cu} donor type by forming electrically passive Na_{Cu} and reduction of the compensating donors by filling selenium vacancies (V_{Se}); (2) creation of acceptor-type Na_{In} defects, Na substituting on a Cu site resulting in the formation of a stable compound $NaInSe_2$, which has larger band gap energy [138][139][140]. In 1994, H. Ruckh et al, noticed that the sodium incorporation led to reduce the width of the space charge region, as the depletion region in Na-doped CIGS solar cell was 3 times smaller compared with undoped CIGS solar cell [135]. (3) Increase in grain size and a strong (112) orientation of the CIGS film [141][142], and impede the interdiffusion of In and Ga [143]. Na incorporation into CIGS films act on the grain boundaries rather than in the bulk [144]. In the other hand, S. Zahedi-Azad et al. [145], have shown that the incorporation of sodium into GR-CIGS creates a pronounced gradient that is detrimental for carrier collection.

C- Post-deposition treatment (PDT)

As briefly seen previously for Na, post-deposition treatment is a method to incorporate alkali elements (Na, K, Rb, Cs, and Li) into absorber layer. Heavy alkali treatment on CIGS absorber has become an indispensable requisite to produce high efficiency CIGS solar cells of all polycrystalline solar cells. In 2005, Rudmann et al. achieved efficiency above 14 % with CIGS TFSCs on PI substrate and doped by Na-PDT. In 2013, Chirila et al. improved the

efficiency of flexible CIGS solar cells on a PI substrate up to 20.4% by simultaneous evaporation of KF under Se atmosphere onto the CIGS absorber heated at 350 °C. Surface modification using PDT using heavy alkalis (K, Rb, and Cs) on CIGS thin film has been the main strategies to recently increase the record efficiency of CIGS solar cell (from 20.3% to 23.4%) from 2011 to 2019 [146]. The current world record efficiency of 23.35% was achieved by applying the postdeposition treatment of CsF (CsF-PDT) on a CIGS thin-film solar cell absorber together with a sulfurization of the surface, Figure 2.22 shows the high CIGSe solar cells made from heavy alkyls PDTs [42] [147] [148].

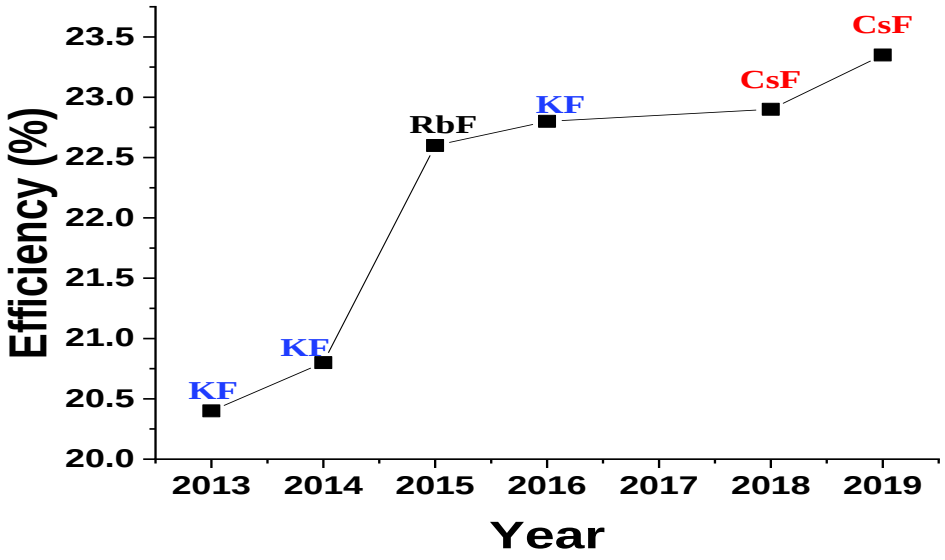

Figure 2.21: High-efficiency CIGS solar cells made from KF-, RbF- and CsF-PDTs on CIGS.

Effect of Heavy alkyls PDT strategies on Cu(In,Ga)Se2 absorbers

Heavy alkyli PDT change the surface morphology, band alignment at the buffer / CIGS interface and grain boundaries (GBs) [149] [150], increase the net charge carrier concentration, decreases recombination at the interface and enhances the diffusion of Cd atoms into the CIGS absorber improved junction quality, are noticed in many research [151] [152] [153]. A. Laemmle et al., have noticed an increase in J_{sc} due to higher carrier collection in the infrared region [153]. Moreover, the PDT treatment allows to use a thinner CdS layer,

which promotes large coverage of the buffer layer and reduces optical losses [150] with a widening of the band gap at the absorber surface [154]. A. Vilalta-Clemente et al., showed that the incorporation of Rb resulted in significant changes in the chemical composition at GBs and improved the efficiency. The postdeposition treatment of CsF (CsF-PDT) exhibited further reduction in the bulk recombination [150]. H. Lee et al., showed that the CsF-PDT on CIGS reduced the number of deep donor type defects such as V_{Se} and In_{Cu} and deep level acceptor type defects such as V_{In} or Cu_{In}, thus improving the p-type characteristics of CIGS [155]. Furthermore, the formation of wide band gap secondary phases $KInSe_2$, $RbInSe_2$, and $CsInSe_2$ at the CGISe/CdS interface improved the electrical properties, surface morphology and band alignment of the device[156].

In summary, the main beneficial effects of PDT can be summarized as follow: increase of the holes concentration in the absorber, improving of the quality of the PN heterojunction, reduction of the recombination at the CdS / CIGS interface, better recrystallization, improved band alignment, and change of the grain boundary composition. All these changes generally result in Voc, FF and Jsc increases than enhance the efficiency.

3 Experimental and methods

3.1 Structure of the solar cells

All solar cells investigated in this thesis work were fabricated at the Catalonia Institute for Energy Research (IREC). The solar cell consisted of a multilayer stack onto a fluoride doped tin oxide (FTO, SnO_2/F) back contact, purchased from Sigma-AldrichTM (reference #735183) and coated on glass slide 100 mm × 100 mm × 2.3 mm with a surface resistivity of ~7 Ω/sq and a transparency of ~82% (for visible light). A thin Mo layer (<15nm) was first deposited by DC magnetron sputtering. Then Cu–In–Ga alloy precursors were deposited on FTO/Mo substrates using a DC magnetron sputtering system and thermal evaporator at room temperature. The GIG rate was controlled by X-ray fluorescence (XRF) analysis to produce CIGS absorbers with high gallium content GIG = 0.7 (Eg ≈ 1.5 eV), to obtain a suitable bandgap for top-cell application and the thickness of precursor films was controlled to 700 nm to produce CIGS films with a thickness of 1.5 um. Subsequently, the metallic precursors were selenized to form the CIGS films (see details in the next section). Before the buffer layer, the CIGS absorbers were chemically etched in 2% KCN solution for 10 min. A layer of CdS was deposited by chemical bath deposition (CBD) for p-n junction formation, the window layers i-ZnO and ITO being deposited using DC magnetron sputtering. No anti-reflection coating (ARC) nor metallic grid have been used in the devices preparation. Finally, the different CIGS solar cells were defined with an area of 3×3 mm^2 using a mechanical scriber. devices preparation. Finally, the different CIGS solar cells were defined with an area of 3×3 mm^2 using a mechanical scriber.

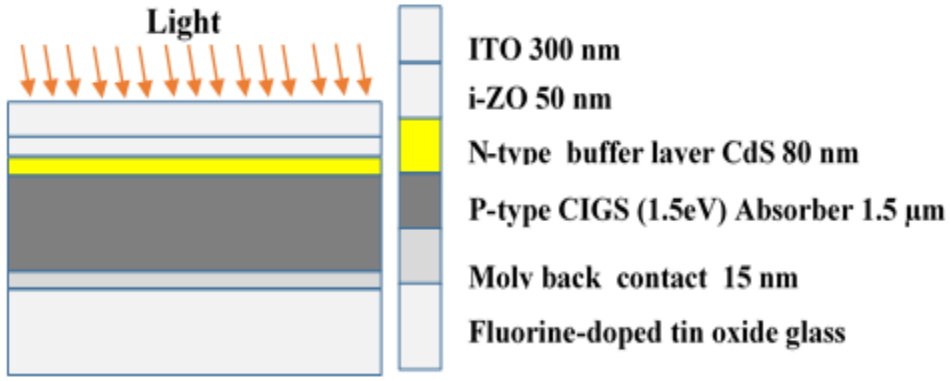

Figure 3.1: Solar cells configuration.

3.2 Solar cells fabrication

A- Magnetron sputtering

Magnetron sputtering is a physical vapor deposition (PVD) widely used in thin film deposition. This process involves the generation of a plasma in a vacuum chamber from an ionized gas (usually argon) by applying a DC voltage between two electrodes, the substrate being placed on the anode and the target mounted on the cathode (being cooled with circulating water). Accelerated argon ions in the chamber bombard the target materials, material is detached from the target then deposited on a substrate producing a thin film (Figure 3.2). DC is generally used for conductive materials like metals while DC-pulsed or RF is preferred for non-conductive materials like oxides. Several parameters affect the sputtering deposition, such as the working pressure, the power supply, the substrate temperature and the target-to-substrate distance, and have a strong effect on the electrical, structural and morphological properties of films. Their control is primordial to tune the properties of the sputtered films.

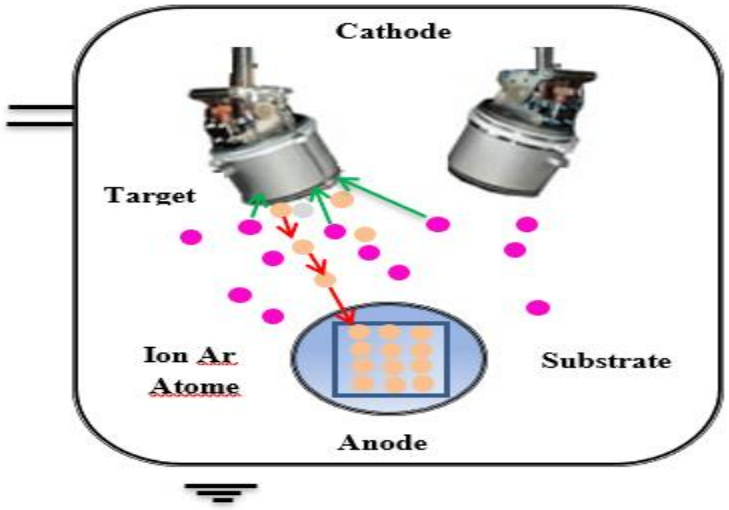

Figure 3.2: Schematic diagram of magnetron sputtering system.

Magnetron sputtering has many advantages: (1) high deposition rates, (2) ease of sputtering any metal, alloy or compound, (3) high-purity films, (4) extremely high adhesion of films, (5) excellent coverage of steps and small features, (6) ability to coat heat-sensitive substrates, (7) ease of automation, and (8) excellent uniformity on large-area substrates [157].

Figure 3. 3 shows the two sputtering systems used in this Thesis, the DC-pulsed **Alliance CT100** Cluster (A) and DC **Alliance Ac450** (B), used respectively to deposit TCOs and metal layers required for the fabrication of CIGS solar cell. In the Alliance Ac450 chamber, three cathodes Cu, CuGa and CuIn targets can be installed for the deposition of Cu-In-Ga metallic layers. In the cluster Alliance CT100, there are two chambers, the first (left) one with Mo target installed inside (for the deposition of the back contact) and the other (right) one with ITO and i-ZnO targets (for the deposition of the window layers). Table 3.1 summarizes the deposition parameters of all the layers made using these sputtering machines.

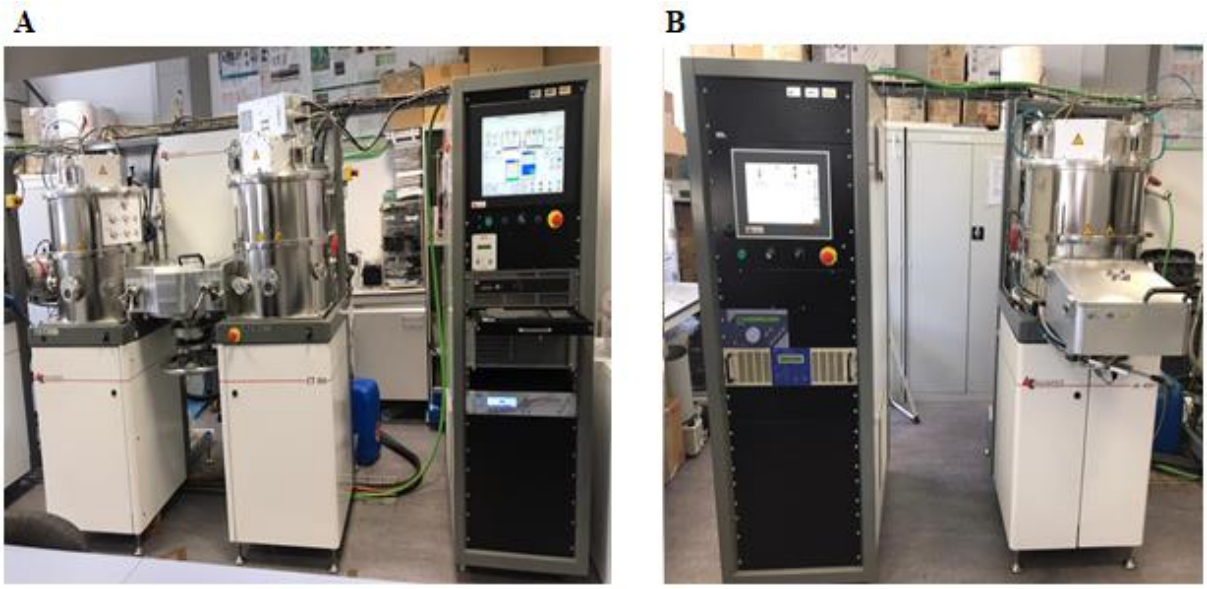

Figure 3.3: (A) sputtering Alliance CT100, and (B) sputtering Alliance Ac450.

Table 3.1: Deposition parameters for each layer.

Mo	Time (min)	Pressure (mbar)	Tension (V)	Intensity (A)	T(°C)
MOA	0.5	$1{,}3.10^{-3}$	377	0.87	-
CuGa	60	$1{,}.10^{-3}$	550	0.15	-
Cu	10	$1{,}.10^{-3}$	400	0.25	-
i-ZnO	10	$5.24.10^{-4}$	482	0.15	25
ITO	20	$1{,}.670^{-3}$	371	0.35	200

B- Thermal evaporator

Thermal evaporation consists in heating a solid material by applying an electrical current in a high vacuum chamber, until evaporation of the source material occurs and it condenses on a cold substrate to form the film. The quality of the deposited thin film depends on several parameters, such as the applied power, the vacuum base pressure, the deposition rate or the purity of the source material. As the substrate is not heated, the films are generally no crystalline, but amorphous.

An Leybold UNIVEX 250 system has been employed throughout this thesis in order to deposit Indium and the different alkalis for the post and pre deposition treatments. The system is comprised by an evaporation chamber connected to a mechanical and a turbomolecular pump, a DC generator (PCM lambda) and a multi-channel quartz crystal sensor (SQM-160) used to control the thickness and layer growth rate. Table 3.2 summarizes the deposition parameters for the materials deposited by thermal evaporation.

Figure 3.4: UNIVEX 250 thermal evaporator.

Table 3.2: Various deposition conditions for In and alkali fluoride layers.

layer	Rate (A°.s^{-1})	Power (W)	Pressure (mbars)
In	0.5	22	10^{-5}
NaF	0.2	12	10^{-5}
CsF	0.2	11	10^{-5}
RbF	0.2	15	10^{-5}
KF	0.2	20	10^{-5}

C- Selenization and sulfurization furnace

Reactive annealing is a frequently used technique for the manufacture of thin film solar cells. During the process, pressure and temperature in the reaction chamber, amount of Se or S, and time are the variables through which the process can be tuned.

Reactive annealing process

A two-step reactive annealing under Se atmosphere is performed by placing the metallic precursor samples in a graphite box together with an optimized amount of elemental Se (50 mg in the small graphite box and 100m g in the big box), the semi closed box was then introduced into a three-zone quartz tube furnace (figure 3.5 (A)). In a first step, the temperature is increased from room temperature to 400°C at a heating rate of 20 °C.min^{-1} and maintained for 30 minutes at constant 1.5 mbar pressure under a constant Ar flow (pump valve open). In a second step, the temperature is increased with the same 20 °C.min^{-1} heating rate to 550°C, then maintained for 15 minutes at constant 1 bar pressure without flow (pump valve closed), as shown in figure 3.5 (B).

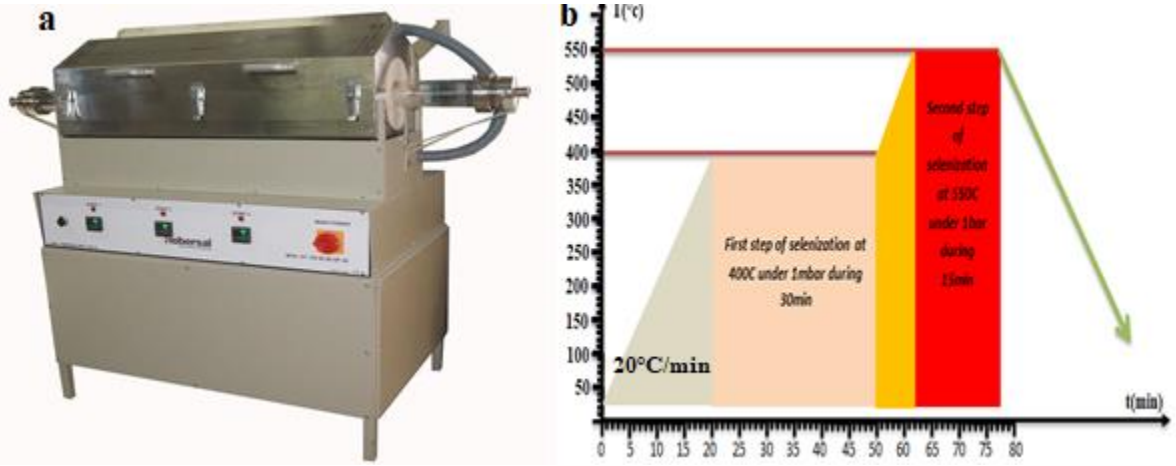

Figure 3.5: a) Three-zone tubular furnaces. b) Temperature profile of the two-step annealing process from IREC's.

D- Chemical bath deposition

Chemical bath deposition technique (CBD) is known to be a very simple and inexpensive technique and has been widely used in the fabrication of TFSCs to deposit the CdS buffer layer. Before the deposition of the buffer layer, the surface of the absorbers is generally cleaned to remove possible secondary phases, via a solution of KCN (especially Cu ones). The samples are then fixed on a glass support and vertically immersed in the beaker containing the solution, as shown in figure 3.6. The deposition time was 45 min. After CdS deposition, the samples were washed with water to remove loosely adhered sulphur particles on the film and finally dried in air. The parameters employed during the deposition of CBD CdS films are summarized in Table 3.1.

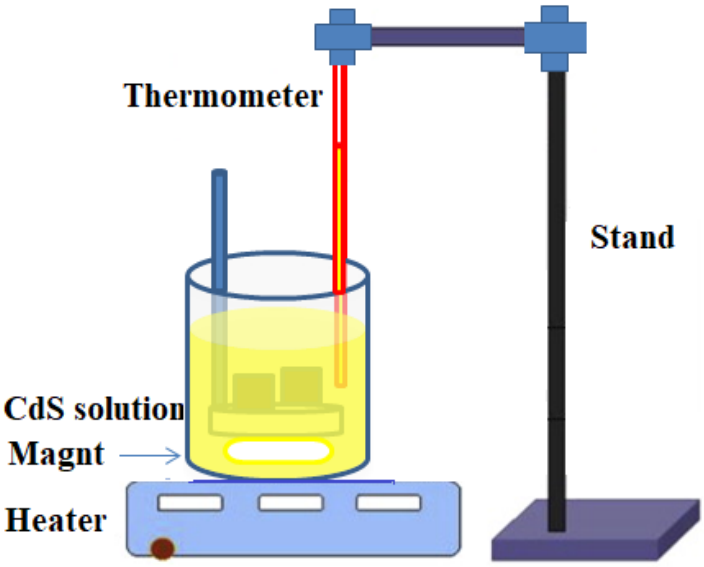

Figure 3.6: Chemical bath deposition.

Table 3.3: the depositions and preparation parameters of the buffer layer.

Reaction temperature	**75°C**
Cadmium Nitrate	0.1 M
Thiourea	0.05 M
pH in solution	9.5 ~ 10
Reaction time	40 min
Thickness	50~60 nm

3.3 Material Characterization

A- X-ray fluorescence spectrometry (XRF)

X-ray fluorescence spectrometry (XRF) is a quantitative technique of elemental analysis using physical properties of the material to determine the elemental composition. The working principle is detailed in the figure 3.7, when a sample is bombarded by primary radiation emitted by an energetic excitation source, one or more electrons can be ejected from their electron shells. Thus, an electron from a higher electronic shell replaces the ejected electron and in turn releases energy in the form of X-rays. This secondary radiation constitutes the phenomenon of Fluorescence, and XRF peaks with different intensities are obtained depending on the atoms. Analyzing the XRF spectrum (the graphical representation of the peak intensities as a function of energy) allows not only identifying the elements present in a sample but also determines their concentrations.

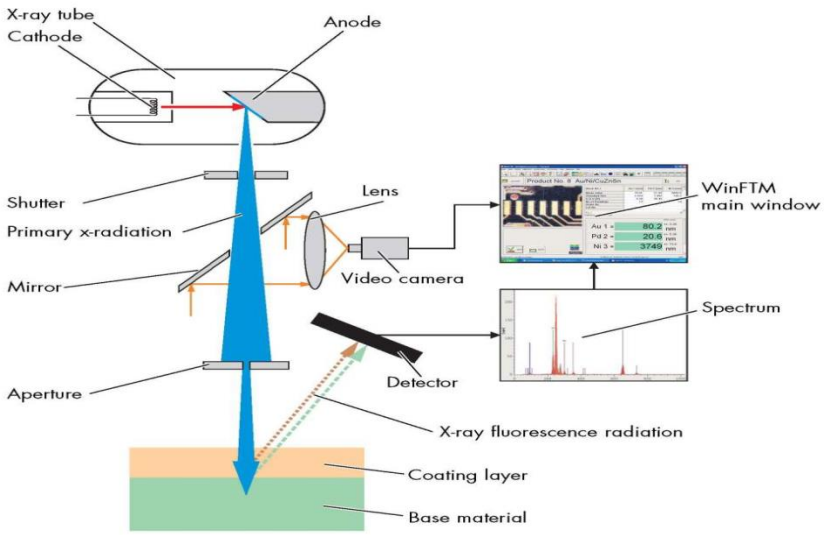

Figure 3.7: X-ray fluorescence principle.

A X-fluorescence XDV Fischerscope (Figure 3.8) was employed to measure the chemical compositions and thicknesses of all the layers and samples prepared. For this, the XRF was previously calibrated using inductively coupled plasma mass spectrometry (ICP), Scanning Electron Microscope (SEM) and Confocal microscope, for the composition and thickness.

Figure 3.8: X-ray fluorescence.

B- X- Ray Diffraction (XRD)

X-ray diffraction (XRD) is an analytical technique that provides information on the different crystalline phases present in the material synthesized, the preferred orientations of the crystals, the size of the crystallites and defect structure, based on coherent X-ray scattering through a crystal lattice. Bragg diffraction occurs when a crystal is bombarded with X-rays of a wavelength comparable to the atomic spacing incident on a crystalline sample. As shown in figure 3.9 Waves 1 and 2 constructively interfere giving rise to a diffraction peak on the detector, varying the orientation of the crystal relative to the x-ray beam step by step and measuring the diffracted intensity for each angular step. The position of the peaks and their relative intensity makes it possible to trace the nature of the crystal thanks to databases.

$$2dsin\theta=n\lambda \qquad \textbf{(3.1)}$$

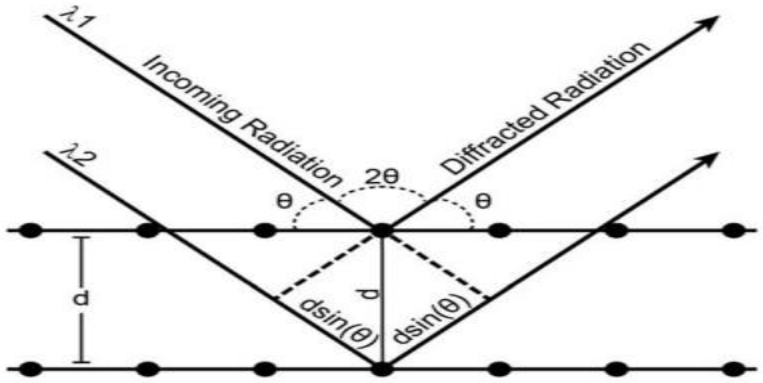

Figure 3.9: Schematic illustration of Bragg condition and Bragg's law [158].

Table 3.4: Joint Committee of Powder Diffraction Standards (JCPDS) references of most phases in CIGS.

Compound	**Structure**	**Reference JCPDS**
FTO	Tetragonal	77-0452
Mo	Cubic	42-1120
$MoSe_2$	Hexagonal	29-0914
In	Quadratic	05-0642
Cu	Cubic	04-0836
CuGa	Quadratic	25-0275
CuIn	Monoclinic	35-1150
Se	Hexagonal	06-0362
Cu_2In	Hexagonal	42-1475
$Cu_{11}In_9$	Monoclinic	41-0883
$Cu_{16}In_9$	Orthorhombic	26-0523
Cu_9In_4	Cubic	71-0458
Cu_9Ga_4	Cubic	42-1476
Cu_2Se	Orthorhombic	371187
α- CuSe	Hexagonal	06-0427
β- CuSe	Orthorhombic	27-0184
γ- CuSe	Hexagonal	27-0185
$CuInSe_2$	Quadratic (chalcopyrite)	40-1487
$CuInSe_2$	Quadratic (chalcopyrite)	23-0208
$CuIn_{0.7}Ga_{0.3}Se_2$	Quadratic (chalcopyrite)	35-1102
$CuIn_{0.4}Ga_{0.6}Se_2$	Quadratic (chalcopyrite)	35-1101
$CuIn_{0.34}Ga_{0.66}Se_2$	Quadratic (chalcopyrite)	51-1222
$CuIn_3Se_5$	Quadratic	51-1221
$CuGaSe_2$	Quadratic (chalcopyrite)	35-1100

The films are analyzed to determine phase and crystal structure, using a Bruker D8 Advance (Figure 3.10), scanning rate of 0.6° min^{-1}, a step size of 0.010°, and 2θ range from 10 to 120°, using Cu Kα radiation (λ = 1.5406 Å) operating at 40 kV and 40 mA. Table 3.4 summarizes JCPDS references of most phases in CIGS and which are used to identify the presence of possible other phases.

Figure 3.10: D8 ADVANCE X-ray diffraction.

C- Raman spectroscopy

Raman spectroscopy has been used to study the crystalline quality of the material and the presence of secondary phases. This technique is based on the inelastic scattering of photons produced by their interaction with the material, which results in the appearance of vibrational bands that constitute the Raman spectrum. These band include internal modes (related to atomic buildings) and external modes (related to the symmetry of the crystal lattice).

A Raman spectroscopy setup developed at IREC was employed. It consists of a Raman probe coupled by optical fibres to two spectrometers: a Horiba Jobin Yvon FHR640 (optimised for the ultraviolet-visible spectral region) and a Horiba Jobin Yvon iHR320 (optimised for the near infrared-infrared region) which are coupled, in turn, to cooled CCD detectors. Several lasers with wavelengths ranging from 325 to 1024 nm were available as excitation sources. Lower laser power densities (< 25W/cm^2) were employed to avoid any substantial heating of the samples. To reduce the uncertainty originating from punctual measurements in the Raman spectra, a large spot diameter (of the order of 100 um) was used, allowing to reduce the impact of the micro-crystalline inhomogeneities

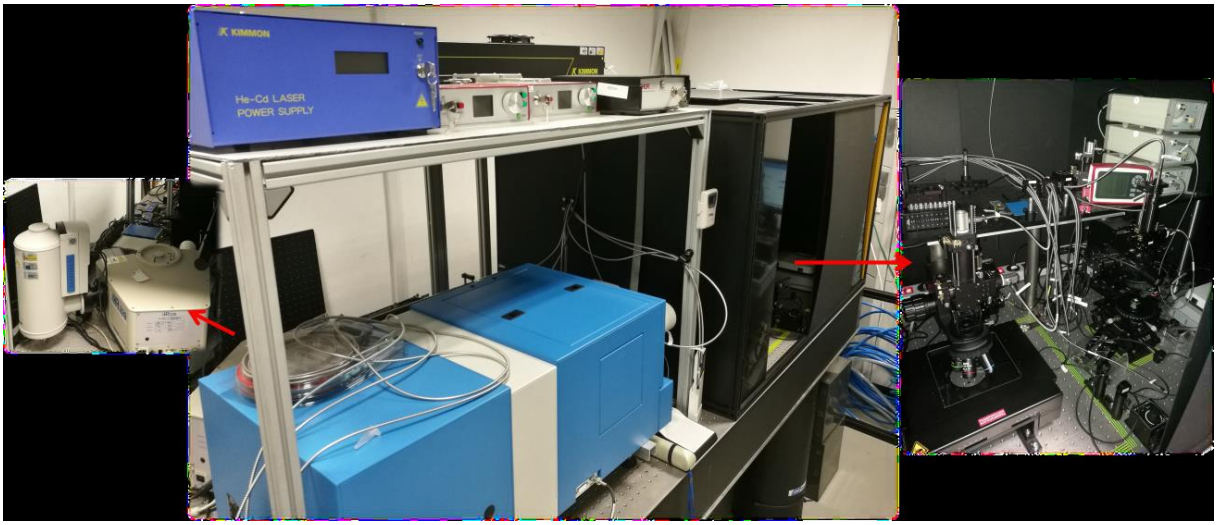

Figure 3.11: Raman spectroscopy system at IREC.

D- Scanning electron microscope (SEM)

The scanning electron microscope (SEM) is the most widely used instrument to obtain information about the morphology, microstructure, and chemical composition of the materials. In this study, a ZEISS Series Auriga microscope (figure 3.12) using accelerating voltage (5-10 kV) with a working distance of 5-8 mm and a magnification range from 10000 x to 50000 has been employed to characterize the devices investigated in this thesis.

Figure 3.12: The scanning electron microscope.

3.4 Solar cells characterizations

A- J-V characterizations

The current-voltage curve of a solar cell represents the relationship between the flowing current and applied voltage and is the main electrical characteristic of a diode, usually measured both under light and dark. From the J-V curve the main figures of merit characterizing the solar cell can be extracted: short circuit current (Jsc), open circuit voltage (Voc), fill factor (FF), efficiency (η), series resistance (Rs), and shunt resistance (Rsh). The current density-voltage (J-V) dependency of a solar cell can be expressed as:

In Dark: $$J(V) = J_0 \left[exp\left(\frac{q}{k_B T}\right) - 1 \right] \quad (3.2)$$

Under Light: $$J(V) = J_0 \left[exp\left(\frac{q}{k_B T}\right) - 1 \right] - J_{ph} \quad (3.3)$$

The illuminated J–V curve of a solar cell with Rs and Rsh is given by

$$J(V) = J_{ph} - J_0\left[exp\left(\frac{V+VJR_S}{\frac{k_BT}{q}}\right) - 1\right] - \frac{V+AJR_S}{AR_S} \quad (3.4)$$

Where A is the total area of a solar cell.

Where J_0 is the reverse saturation current of the diode, q is the elemental charge, k_B is Boltzmann's constant and T is the temperature, J_{ph} is the photocurrent generated density.

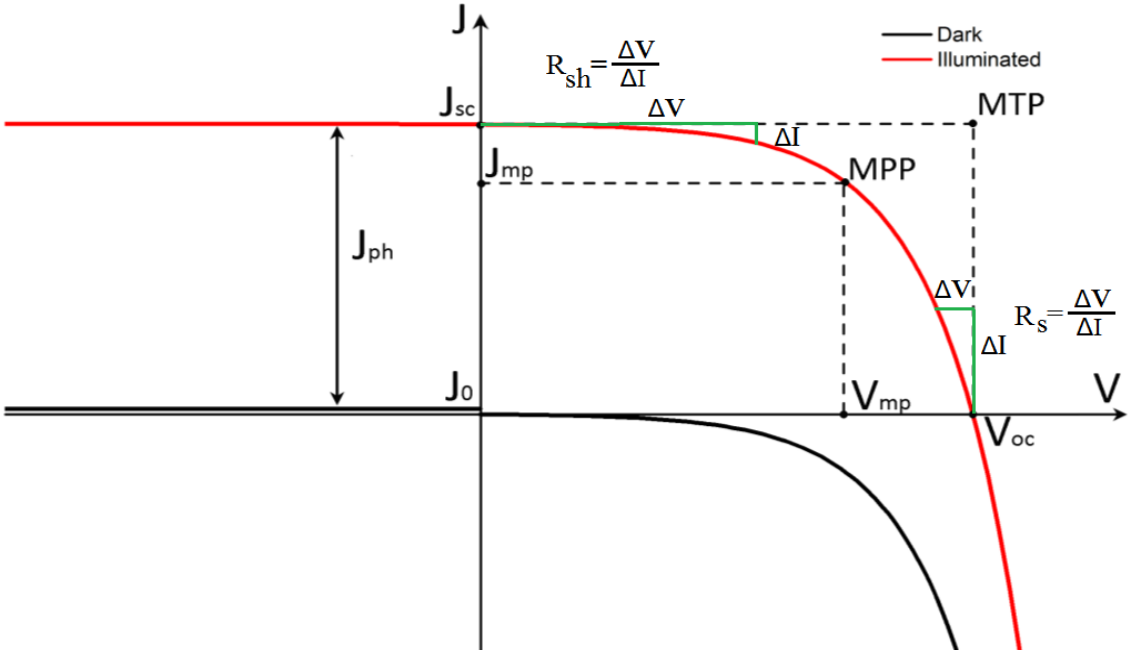

Figure 3.13: I-V characteristics of an ideal diode solar cell in dark and under illumination [159].

A setup consisting of a pre-calibrated Sun 3000 Class AAA solar simulator by Abet Technologies (Figure 3.14) coupled to a Keithley 2400 source was employed to characterize the devices fabricated in this thesis. The efficiency was measured under Standard Test Conditions (STC), at normal illumination of 1000 Wm^{-2}, at the temperature of 25 ° C and under an AM1.5 spectrum.

Figure 3.14: ABET TECHNOLOGIES Solar simulator.

B- External Quantum Efficiency (EQE)

External Quantum Efficiency (EQE) is another important method that is commonly implemented to observe solar cells' behavior in a specific range of wavelength. EQE takes into account all possibilities of photon interaction including reflection, absorption and transmission, hence given by:

$$\boldsymbol{EQE} = \frac{\textbf{number of charge carriers collected}}{\textbf{number of incdent photons}} \tag{3.5}$$

$$\boldsymbol{EQE(\lambda)} = \frac{\textbf{Electrons out}(\lambda)}{\textbf{Incident photons}(\lambda)} = \frac{\mathbf{J_{SC}}(\lambda)}{\mathbf{q\Phi}(\lambda)} = \frac{\mathbf{hc}}{q} \times \frac{\mathbf{J_{SC}}(\lambda)}{\lambda \mathbf{P_{in}}(\lambda)} = \mathbf{1240}\frac{\mathbf{J_{SC}}(\lambda)[\text{Å}\mathbf{cm^{-2}}]}{\lambda[\mathbf{nm}] \times \mathbf{P_{in}}(\lambda)[\mathbf{Wcm^{-2}}]} \tag{3.6}$$

Where J_{SC} is the short circuit current density, Φ is the photon flux, Pin is the light intensity at a certain wavelength λ, q the elementary charge, and h and c are the Planck's constant and speed of light.

The second type of quantum efficiency is the internal quantum efficiency (IQE) which is the EQE corrected by the cell's reflectivity, that is the ratio of the number of charge carriers collected by the solar cell to the number of photons absorbed by the cell.

In this study, a Bentham PVE300 system (figure 3.16) has been used for EQE measurement and IQE calculation with the help of reflectance and transmittance measurement. Benwin+ is a control software which provides user friendly interface between optical and electronic components. The system consists of monochromatic, dual light source with Xenon and QTH lamps, phase-insensitive lock-in amplifier, chopper, current pre-amplifier, integrating sphere for reflectance/transmittance measurements and Si and Ge detectors for calibration.

Figure 3.15: Spectral response system used for EQE measurements.

4 Development of a sequential process for Ga-rich CIGS on FTO substrate

4.1 Introduction

In recent years, the development of efficient wide band gap CIGS solar cells has gained interest due to the flexibility in term of cost-performance of the CIGS technology and especially the ability of tuning the bandgap by controlling the composition. Consequently, the fabrication of high efficiency GR-CIGS TFSCs on transparent substrates is critical in that regard. Therefore, in this chapter, the primary focus was to develop a baseline process based on sequential deposition to fabricate GR-CIGS solar cells on FTO substrates with an efficiency close to the state of the art on Mo. In order to achieve this general objective, this chapter focuses on three different aspects:

- Preparation and characterization of GR-CIGS absorbers by focusing on the influence of the chemical composition, in particular copper to group III and gallium to group III ratios in the realization of high efficiency solar cells, focusing their influence on the microstructural, optical and electronic properties of the compound. A systematic analysis has been performed by varying both ratios during the synthesis of CIGSe and using FTO substrates.
- Optimizing the selenization process in order to minimize the possible gallium accumulation at the back interface, focusing on the effects of the processing temperature on the crystallization, composition and performance of GR-CIGSe devices.
- Development of other possible wide band gap buffer layers for GR-CIGS solar cells including, especially CdZnS, ZnS, In_2S_3 which are expected to improve the pn interface band alignment with wide bandgap absorbers.

4.2 Substrate preparation and characterization

The SLG/FTO (FTO substrates) used in this thesis are purchased from Sigma-Aldrich™ (reference #735183) (10 x 10 cm^2, 2.3 mm), sheet resistance of R□ = 7 Ω/sq). First, the substrates are mechanically cleaned with distilled water to remove all dust particles from the surface, then ultrasonically cleaned using acetone for 10 min, isopropanol-2 for 10 min, and distilled water for 10 min, and then dried with a nitrogen gas (N2). A thin layer of molybdenum Mo (15nm) is then deposited on the cleaned substrates by DC-magnetron sputtering, to obtain ohmicity at the CIGS/FTO back interface with the formation of interfacial $MoSe_2$ during the Se reactive annealing step of the precursor. The deposition parameters of Mo layer are summarized in the Table 3.1. Sheet resistivity of the Mo+FTO back contact measured by four points probe was typically around 5 Ω/sq, a value close to that of the bare FTO. In order to investigate the effect of the formation of $MoSe_2$ on the rear contact transparency, and because FTO naturally acts as a sodium barrier, two substrates FTO/Mo (15nm) without and with 15 nm of NaF were selenized at 550°C for 30 min.

Figure 4.1 shows the treated Raman spectra measured from these samples, under two excitation wavelengths (532nm and 785nm). In the 532 nm spectra (A), the peak at 254 cm^{-1} is higher for undoped samples. So, the increase of this peak could be related to the formation of some defect in the $MoSe_2$ structure due to the Na doping. Some selenium phases also have a peak at that position, which could have indicated the presence of elemental selenium and a lower selenization of Mo due to the Na doping; however, the absence of peaks around 100 cm^{-1} discards this possibility. In fact, the $MoSe_2$ peak at 248 cm^{-1} is reported in Ref, which was ascribed to $E_{2g}{}^2$ shear mode at the M point. Since the shift difference is the same for both samples, this shift is not an effect of the Na doping. For 785 nm excitation wavelength (B), the spectra of both samples are very similar. This could indicate that the Na doping does not affect the $MoSe_2$ bulk.

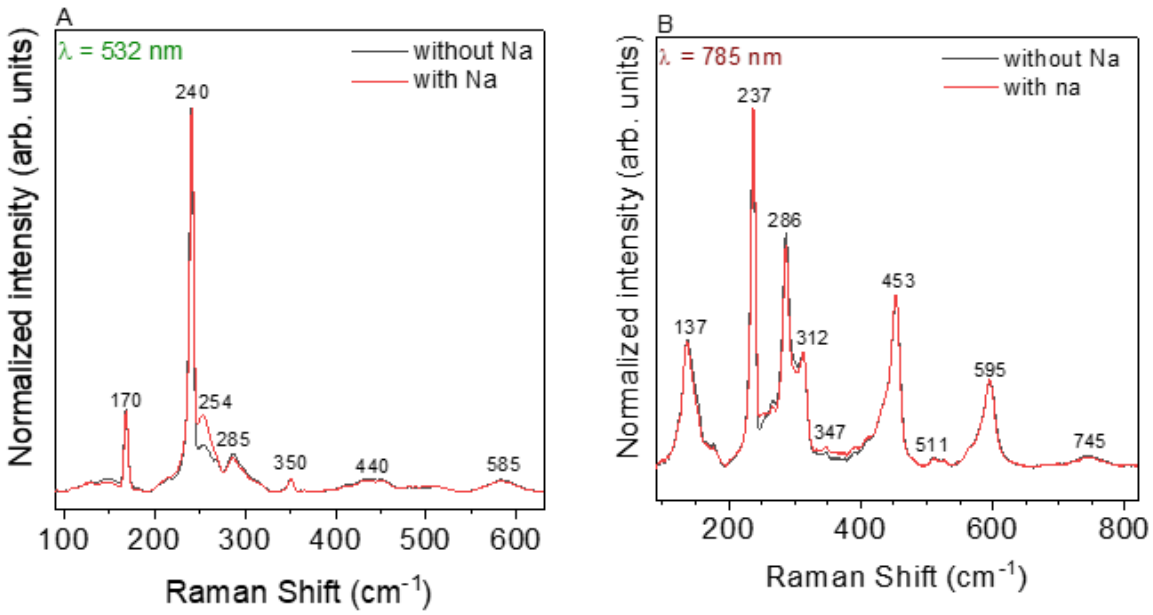

Figure 4.1: Raman spectra of selenized FTO/Mo and FTO/Mo/Na samples obtained using 532 nm and 785 nm excitation wavelengths.

Figure 4.2 shows the experimental optical transmission for different substrate configurations. Due to the relatively narrow bandgap of $MoSe_2$ (1.4eV), the transmission of the samples is significantly reduced as compared to that of bare FTO in the visible range especially, with values ranging from about 5% (400nm) up to 40% (800nm). It should be noted that Na has a limited effect on the transmission, with a 5-10% improvement especially in the infrared region.

While those value indicate a substrate rather “semitransparent” than “transparent”, it should be noted that in the frame of an application to tandem solar cell, the transmission which matters the most is in the infrared region. The samples presented here have a transmission well above 50% after 900nm, and while improvements are still needed, such transparency is already sufficient for a proof-of-concept demonstration.

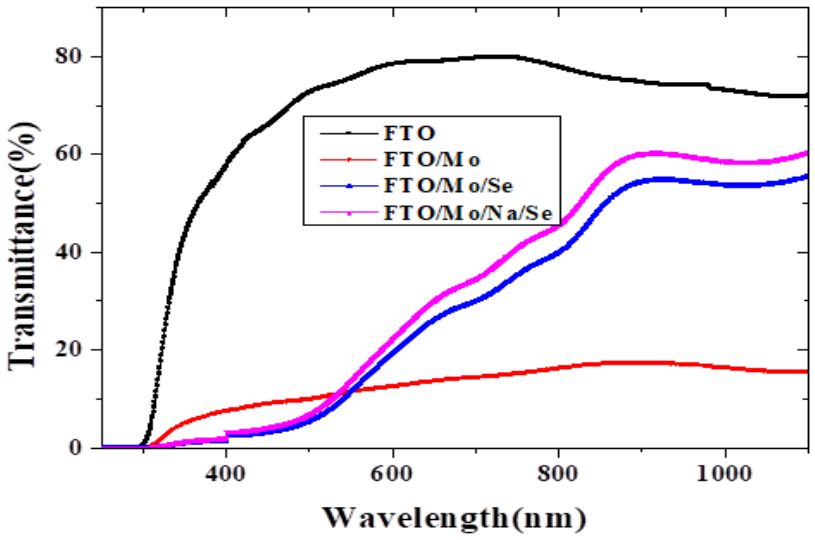

Figure 4.2: Experimental optical transmission for different substrate configurations.

4.3 Compositional Optimization of Ga rich CIGS

GGI and CIG ratios play an important role in the realization of high efficiency CIGS solar cells, influencing the microstructural, optical and electronic properties of the compound. We evaluated the impact of different copper and high gallium content in the GR-CIGS absorber layer on cell performance. Structural and electrical properties of Ga rich CIGS thin films have been studied by changing the CIG and GGI ratios in the films.

Samples fabrication

Ga rich CIGS thin films with various CIG and GGI ratios are grown on FTO substrates, as described in section 3.1. The overall Cu and Ga content in the absorber were changed by varying the Cu and CuGa thickness by adjusting deposition time. On the basis of the properties of CIGS presented in section 2.4, CIG ratio and GGI were controlled in the range of 0.6 to 1 and 0.7 to 1, respectively, as listed in Table 4.1. The solar cells were completed as described in section 3.1.

Table 4.1: Overall composition of samples with varying copper (CGI) and gallium (GGI) contents.

Sample	**Composition (at %)**				**CIG**	GGI
	Cu	**In**	**Ga**	**Se**		
CIG0.6	19.6	10.2	21.1	49.0	0.62	0.67
CIG0.7	20.7	10.1	20.2	48.8	0.68	0.66
CIG0.8	22.8	9.1	20.2	47.7	0.77	0.68
CIG0.9	24.4	9.2	19.0	47.2	0.86	0.67
CIG1.0	25.8	8.4	18.1	47.6	0.97	0.68
GGI1.0	24.3	-	27.0	48.6	0.87	1
GGI0.9	22.3	3.9	25.2	48.4	0.76	0.91
GGI0.8	24.2	7.3	22.4	45.4	0.84	0.78
GGI0.7	21.5	9.8	21.2	47.3	0.69	0.68

Results

A- Effect of copper concentration

Figure 4.3(a) shows the statistical data of the main electrical parameters from J-V characterization which was performed on several cells for Ga-rich (fixed at ~0.7) CIGS for different CGI values. A strong correlation between the CIG ratio and devices performance is observed, with a clear trend showing a maximum of efficiency for a ratio of 0.7, and a deterioration of the performance for CIG ratios over 0.8. Figure 4.3(b) and Table 4.2 shown the J-V characteristics and the main electrical parameters for the best cell of each sample. It is interesting to note that the V_{OC} and J_{SC} of the best cell in CIG0.6, CIG0.7 and CIG0.8 samples are maintained at the same levels of $\sim$ 550 mV and 21 mA/cm^2, respectively, and then dramatically drops. This limitation of the V_{oc} could be related to Fermi level pinning by bulk or interface traps. From the EQE measurements figure 4.3 (c), a similar trend can be observed with a strong deterioration for CIG0.9.

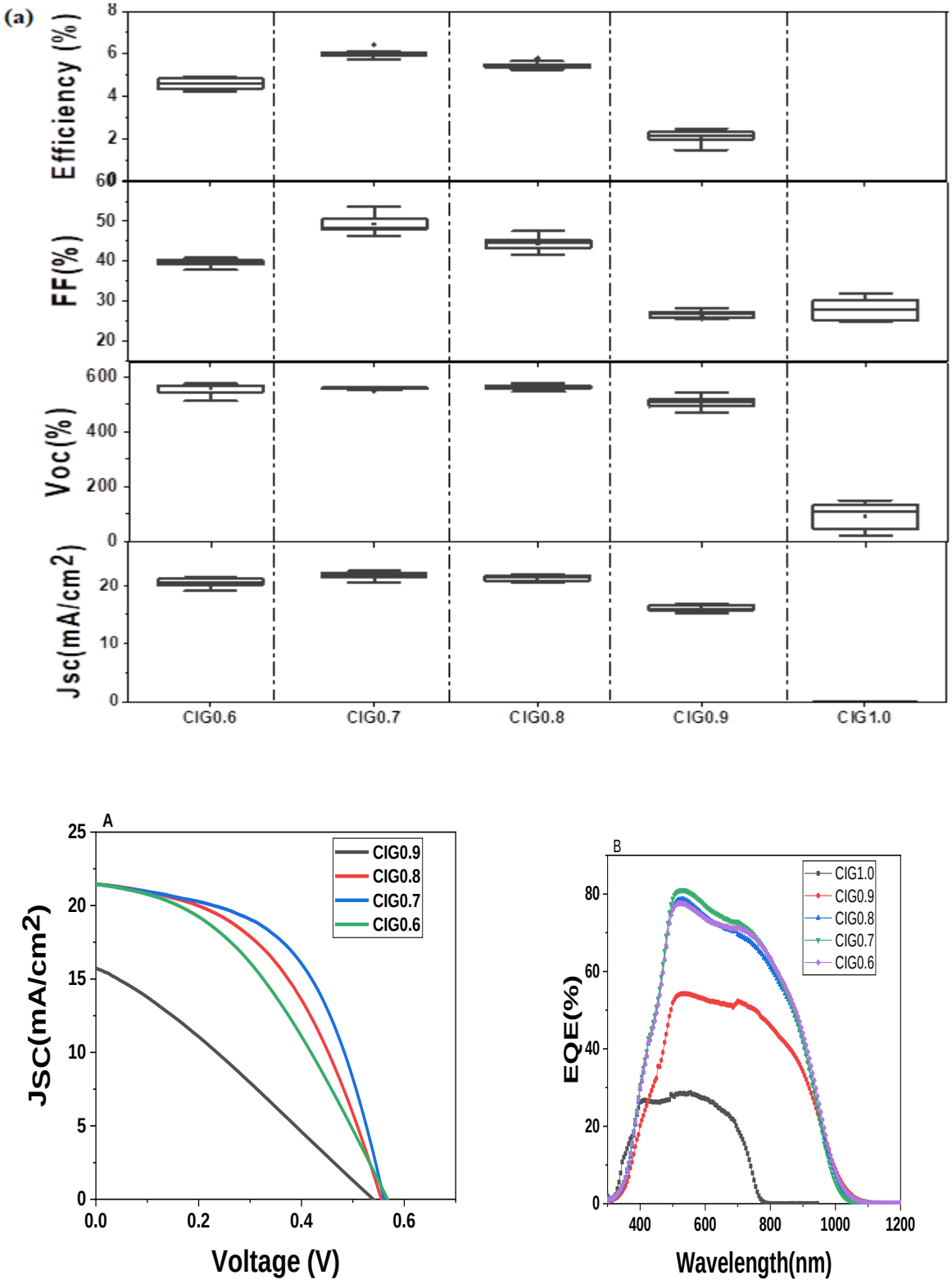

Figure 4.3: Boxchart of the main solar cell parameters cells varying the CGI content. (b) J–V and (c) EQE characteristics of the record cells obtained for each sample.

Table 4.2: Comparison of electrical parameters of the record cells obtained with varied CGI.

Sample	η (%)	FF (%)	Voc (mV)	Jsc (mA/cm^2)
CIG1.0	0	28.64	133	0.01
CIG0.9	2.40	28.17	539	15.82
CIG0.8	5.64	47.50	554	21.43
CIG0.7	6.43	53.63	559	21.43
CIG0.6	4.88	40.24	567	21.39

Figure 4.4 shows cross sectional SEM images of the Ga rich CIGS devices grown on FTO substrate with different Cu contents. A bilayer structure, typical for CIGS fabricated from sequential processing due to the gallium back interface accumulation[41], with large crystals at the top and smaller crystals at the bottom, is detected in all cases. For CIG contents comprised between 0.7 and 0.8, the grains exhibited bigger sizes towards the front, with smalls grains and porosities being observed at the back CIGS/FTO interface, especially for samples (A) and (D).

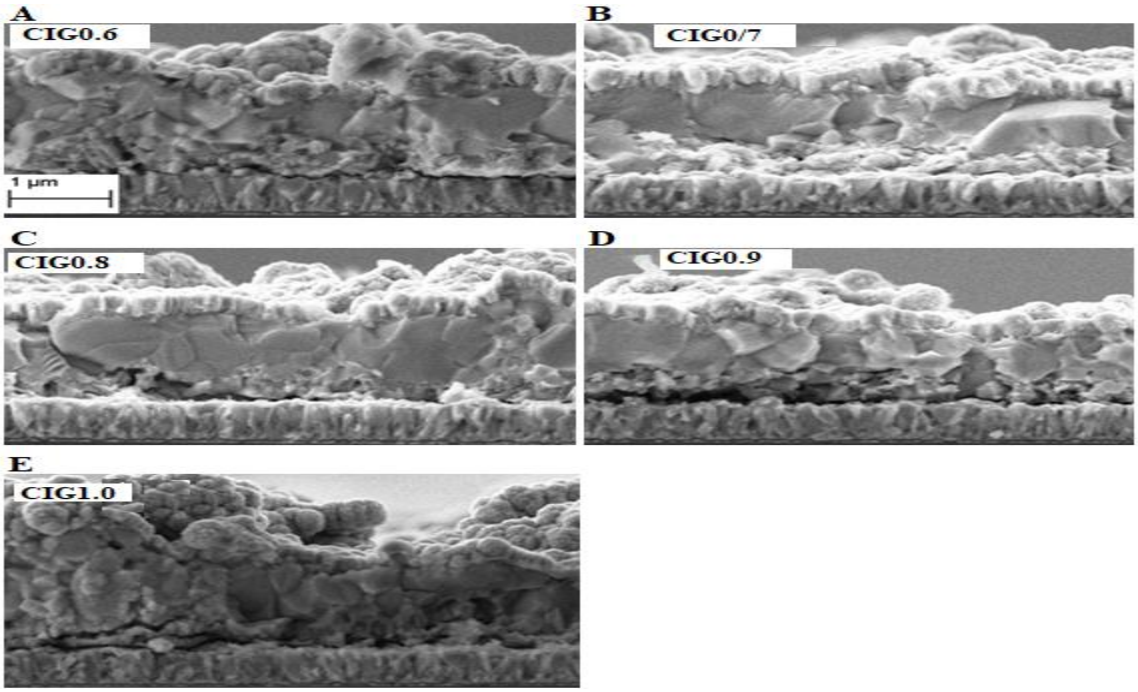

Figure 4.4: Cross sectional SEM images of GR-CIGS grown with CIG=0.6 (A) , CIG=0.7 (B) , CIG=0.8 (C) , CIG=0.9 (D) ,and CIG=1.0 (E).

B- Effect of gallium concentration

Figure 4.5 and Table 4.3 show the JV characteristics and the main parameters of the record solar cells obtained with different Ga contents. A clear relationship of the solar cell parameters with the Ga content is observed, especially for the Jsc and Voc, decreasing for high Ga contents. In contrast to what is expected, there is no correlation between the Ga content in the absorber and the Voc value. All samples suffer from low V_{OC} except GGI0.7 and GGI0.6 samples, low fill factor and low efficiency. The reasons of low efficiencies for Ga-rich CIGS are not yet completely understood and several models (either due to structural or electrical limitation) have been proposed to explain this drop of performance when GGI > 0.4. as reported in chapter 2, the high Ga content leads to the formation of Ga_{Cu} point defects which are much deeper than In_{Cu}. In addition poorer electronic properties of Ga rich CIGS film, increase of the recombination centers, high Ga inside the SCR impacts the Voc [160][161][66]. as well as high Ga content in CIGS absorber induce a buffer/CIGS band offset issue and leads to a degradation in cell performance manifested by a failure of the open circuit voltage (Voc) and a degradation in fill factor (FF). Regarding the Jsc, which is expected to decrease with high Ga content, it decreases effectively linearly with the Ga content, correlated to a loss of absorption in the long-wavelength portion of the spectrum is observed for almost all the cases, as shown in the EQE measurements (Figure 4.6). The electronic bandgaps were estimated from the fitting of the $h\nu \times ln(1 - EQE)^2$, as shown in the inset of Figure 4.6. Eg increased from 1.1 to 1.65 eV for GGI contents of 0.7 and 1.0, respectively. However, these values are lower than the expected ones for such Ga contents, which seem indicating that Ga has probably in part diffused and is not homogeneously incorporated to the matrix, leading to region with low Ga content in the chalcopyrite. Another observation is related to the low FF for samples with a GGI greater than 0.7, which could be also related to Ga diffusion issues at interface.

Table 4.3: Comparison of the main parameters of the record solar cells.

Sample	Jsc (mA/cm^2)	Voc (mV)	FF (%)	η (%)	Rsh ($\Omega.cm^2$)	Rs ($\Omega.cm^2$)
GGI1.0	11.3	472	38.16	2.03	100.78	13.35
GGI0.9	18.2	450	48.94	4.02	187.77	3.6
GGI0. GGI0.8	22.2	467	50.68	5.26	140.80	11,58
GGI0.7	23.8	559	61.62	7.61	523.12	1.14

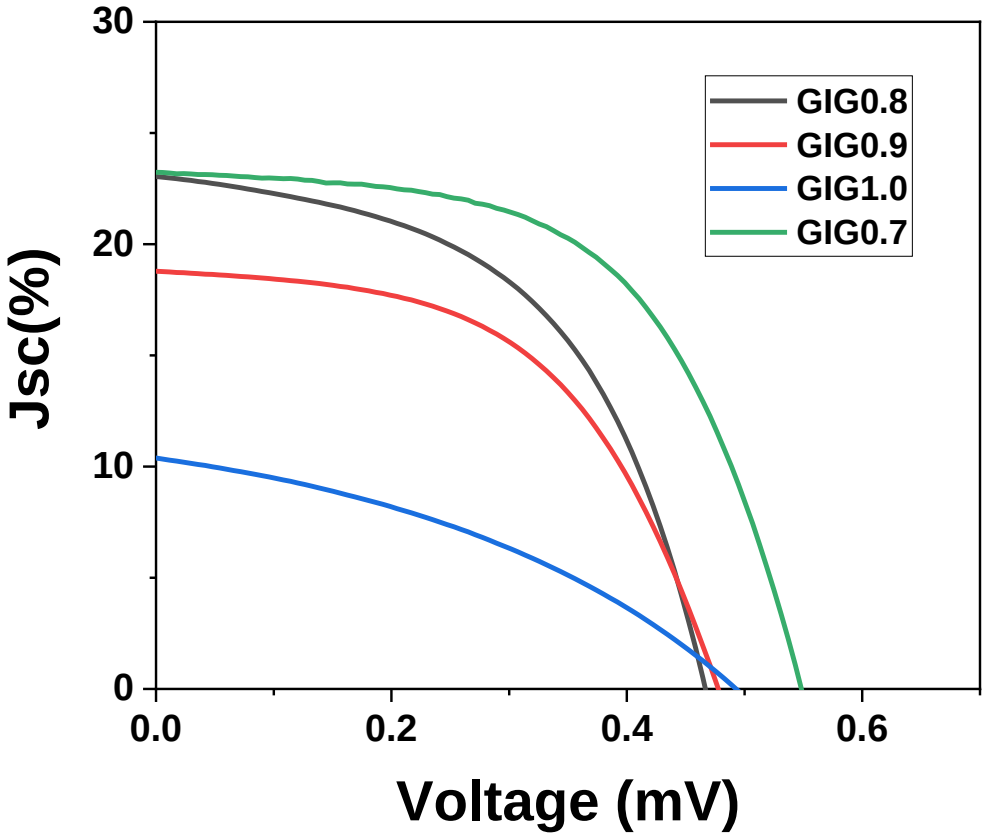

Figure 4.5: J-V characteristics of the fabricated solar cells with the CIGS absorber films prepared with different Ga contents.

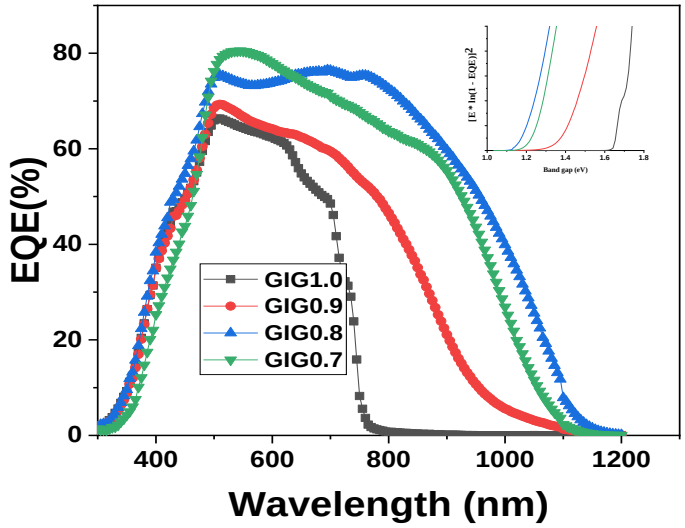

Figure 4.6: External quantum efficiency characteristics of CIGS thin films solar cells fabricated with different GGI ratios of 0.8, 0.9 and 1. Inset: bandgaps determination plot hv×ln(1-EQE)^2 against hv.

The SEM cross section images of samples are shown in Figure 4.7. Clear microstructural changes are observed with to the Ga content, with CIGS grain sizes decreasing with increasing GGI ratio. All the absorber layers also present a bilayer structure with a large-grained in the top layer and a small-grained bottom layer. The absorber layer with GGI contents of 0.7 and 0.8 present the highest grain sizes morphology. The highest Ga content CIGS film has a microstructure composed of small grains, thus increasing the grain boundaries (GB)

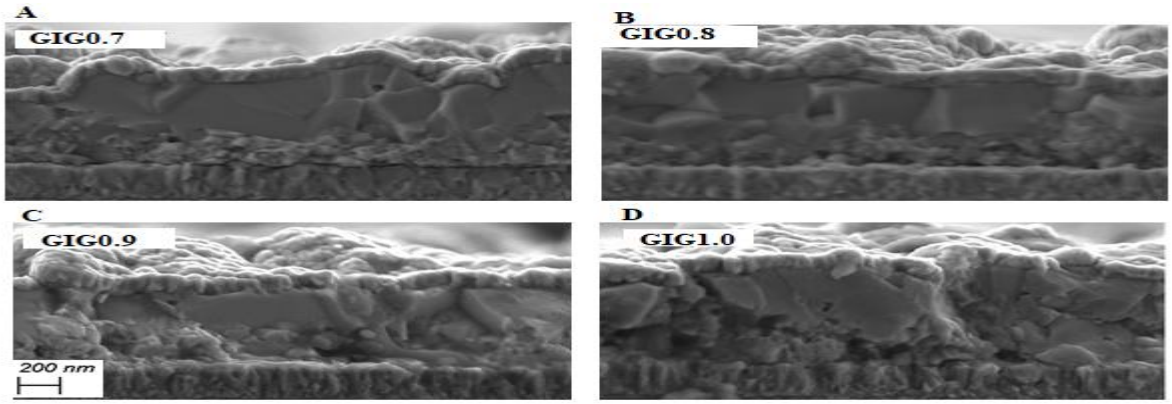

Figure 4.7: Cross section SEM images of Ga rich CIGS for different Ga ratios.

Figure 4.8 shows the typical Raman spectra measured at the surface of the CIGS absorbers under an excitation wavelength of 785 nm. The spectra are characterized by a dominant peak around 180 cm^{-1} and a lower one around 150 cm^{-1}.

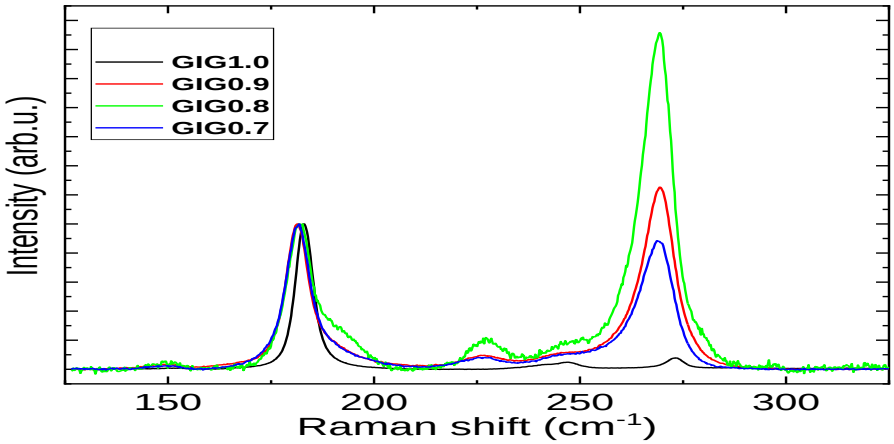

Figure 4.8: Raman spectra obtained using 785 nm excitation wavelength at the front interface of CIGS samples synthesized with different Ga contents.

The peak around 180 cm^{-1} corresponds to the A1 mode of the chalcopyrite $Cu(In,Ga)Se_2$ phase and results from the vibrations of the Se atoms with the Cu and In atoms at rest. The shift in frequency of the A1 mode seems indicating an increase of the Ga content in the CIGS structure, as it is expected for higher GGI ratios. The peak observed at 260 cm^{-1} has been reported to be related to either Cu selenide phases or OVC or defective CIGSe, and could be also related to the OVC peak identified at 150 cm^{-1} and the defective phase identified at 230 cm^{-1}. In any case, since the best results have been achieved for a GGI composition comprised around 0.7-0.8, the Raman measurements reveal the possible presence of secondary phases and/or defective CIGS which could be detrimental for the device performance. It is suspected that the Ga diffusion could be responsible of this behavior resulting in non-homogeneous layer, probably due to the conditions used for the absorber synthesis. For this reason, in the next section, the influence of the temperature is investigated for CIG and GGI ratios which have been optimized, i.e., around 0.7 for both, as

a way to improve not only the properties of the Ga-rich absorber but also the device performance.

4.4 Effect of the annealing temperature on Ga rich CIGS

In the sequential fabrication process, the annealing temperature of the precursors determines important features of the absorber properties. In particular, the temperature has a direct influence on the morphological, microstructural and elemental distribution of the absorber and on the electrical performance of the devices. Therefore, in this section the influence of the annealing temperature on Ga rich CIGS films and devices efficiency is investigated.

Samples preparation

For the sake of studying the effect of the annealing temperature on the properties of Ga rich CIGS films and on devices efficiency, the metallic precursors CuGaIn were prepared as described in section 4.2, with the same optimized CGI and GGI ratios ≈ 0.7. A two-step annealing process was implemented, with a first step at 400°C and under 1.5 mbar Ar dynamic pressure for 30 minutes, and a second step at 1 bar Ar static pressure for 15 min. The influence of the temperature on the performance parameters of the GR-CIGS solar cell is studied for temperatures in the second step ranging from 500 to 600 °C.

Results

Figure 4.9 and Table 4.4 show the statistical data for the electrical parameters, the elemental composition of the CIGS films measured by XRF, and electrical parameters of the best cell of each sample. The best efficiency obtained with the sample annealed at 500 °C is related to the better structural and electrical properties, as measured by XRD (Figure 4.12 (B)). We can find that the effects of annealing temperature on short circuit current and fill factor shows similar trends with cell efficiency. There is a strong enhancement in shunt resistance and an obvious drop in series resistance compared with results of previous experiments.

Table 4.4: CIGS films composition and the electrical parameters of the best of each sample.

T(°C)	d (µm)	Composition (at %)				CIG	GGI	J-V Parameters under AM 1.5 illumination			
		Cu	In	Ga	Se			Jsc (mA/cm)	Voc (mV)	FF (%)	η (%)
500	1,1	21,6	10,1	21,6	46,7	0,68	0,68	22,59	519	61	7,14
550	1,2	21,2	9,24	21,5	48,1	0,68	0,69	21,26	570	59	7,23
575	1,3	21,6	9,08	21,3	48	0,71	0,70	17,19	576	60	6,01
600	1,2	21,7	9,52	21,1	47,7	0,70	0,68	17,17	574	59	5,89

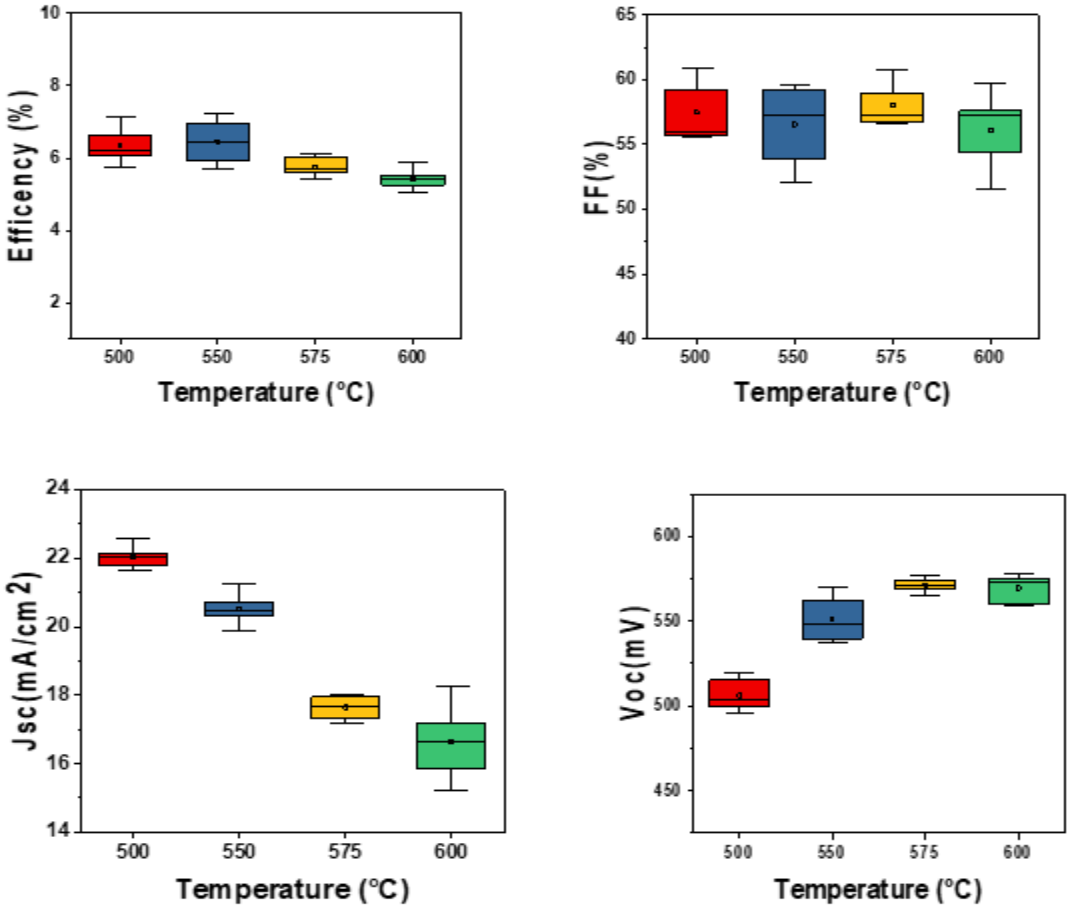

Figure 4.9: Boxplots of the electrical parameters of Ga rich CIGS absorbers on FTO grown at 500 °C, 550 °C, 575 °C and 600 °C.

The box chart diagram gives more information about the possible correlation between annealing temperatures and electrical parameters. The increase of the Voc and decrease of the Jsc with temperature could be related to a widening of the band gap at the surface, even if the efficiency seems here clearly limited by the FF. This assumption seems being confirmed by analyzing the EQE spectra (figure 4.10(A)) of the devices, where a change is clearly observed in the 700–1100 nm wavelength region when increasing the temperature. Indeed, while the GGI remains constant between each sample, the bandgap is visibly shifted toward higher energies when the annealing temperature is increased (figure 4.10(B)), which indicates that while the elemental content in Ga is similar, the Ga is more efficiently incorporated and distributed in the chalcopyrite and thus results is a wider bandgap material with improved optoelectronic properties and a reduced prevalence of Ga-related secondary phases.

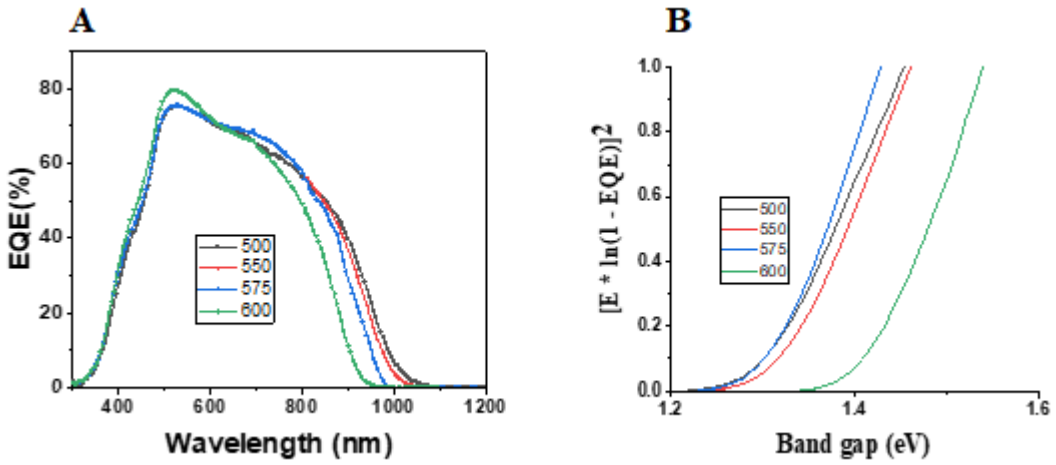

Figure 4.10: A) EQE spectra of devices annealed at various temperatures and B) band gap.

Figure 4.11 shows cross-sectional SEM images of Ga rich CIGS annealed at different temperatures. A bi-layer structure, typical for sequential processing and gallium accumulation, with large crystals at the top and smaller crystals at the bottom is detected in all cases. No clear difference can be observed between samples annealed at 500 and 550°C. However, much larger crystals are found in samples annealed at 575 and 600°C,

which is concistent with the hypothesis that increasing the annealing temperature improves the incorporation of Ga to the chalcopyrite and in returns enhances the cristallinity and reduces secondary phases.

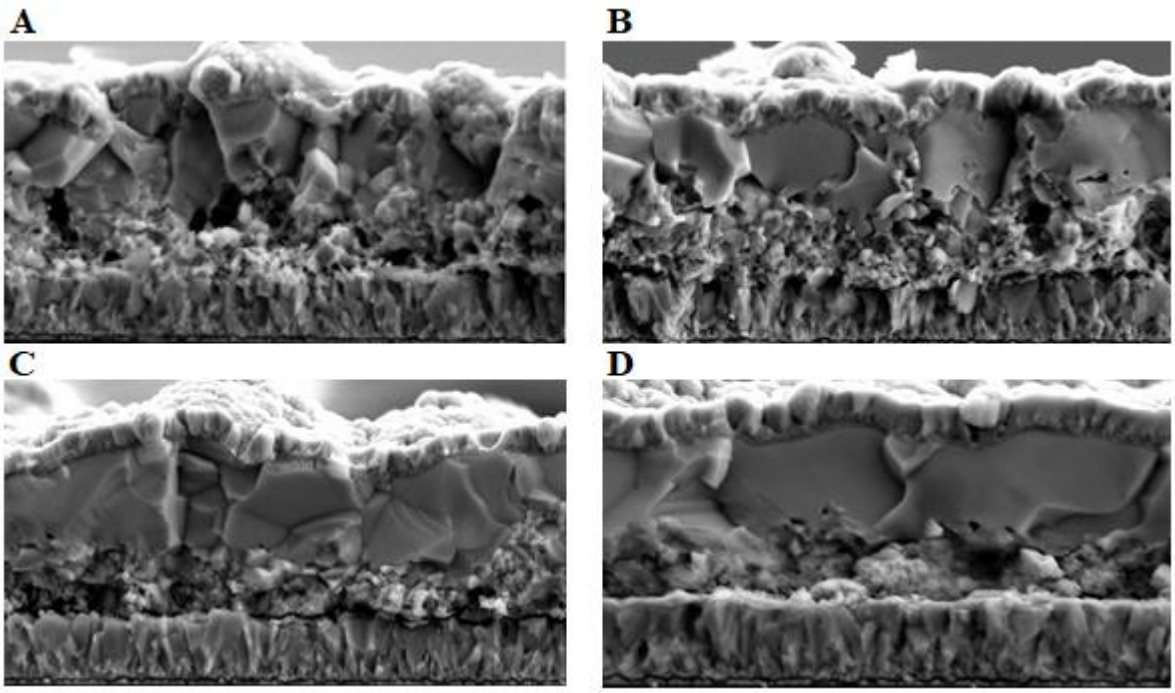

Figure 4.11: Cross section SEM images of Ga rich CIGS annealed at different temperatures (A) 500°C, (B) 500°C, (C) 500°C (D) and 600°C.

Figure 4.12 (A) shows XRD pattern of Ga rich CIGS thin films selenized at various temperatures from 500 to 600. All the CIGS films exhibit strong XRD peaks of (112), located at 2θ = 27.5°. The peak shift toward higher angles and the presence of two or three phases at low temperature is due to the formation of two or three phases with varying gallium content, Ga rich CIGS and CGSe. Ga rich CIGS seems forming in a more homogeneous way with a single phase when the absorber is annealed at 600 °C, which is again consistent with the previously discussed observations. Higher temperatures lead to a higher material quality and more Ga being incorporated to the CIGS.

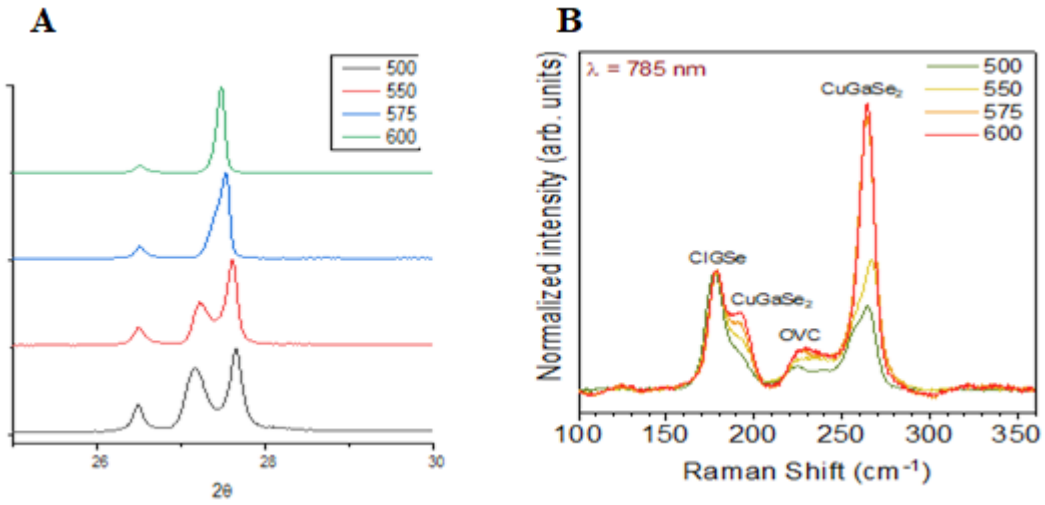

Figure 4.12: A) XRD patterns of CIGS film annealing at different temperature and B) Raman spectra.

The Raman spectroscopy Figure 4.12 (B) show that the Ga content in the CIGS structure at the front interface increases with the annealing temperature, as indicated by shift of 176 cm^{-1} peak and increase of 260 cm^{-1} peak. It also indicates that the OVC and CGSe also increase with the temperature.

SEM, XRD, and Raman indicate that the films are primarily Ga rich CIGS.

Raman spectroscopy shows that OVC and CGSe peaks increase with the annealing temperature, indicating an increasing formation of those phases at higher temperatures. In fact, the intensity of CGSe peak surpasses the one of CIGSe peak at 600 ^{o}C. XRD also shows an increase of CGSe phase (PDF 01-075-0104) with the temperature, while peak associated to CIGSe phase (PDF 00-035-1101) disappears at 575 ^{o}C. Thus, having a higher concentration of CGSe than CIGSe at temperatures above 575 ^{o}C could explain why solar cells annealed at 550°C show the highest efficiency.

All samples show reduced Jsc and Voc. Surface recombination in the interface is the parameter most affecting on Jsc and Voc. Therefore, the development of wide band gap buffer layers probably improves the efficiency of Ga rich CIGS solar cells.

4.5 Development of other possible buffer layers for Ga rich CIGS solar cells

As discussed in section 2.6, CdS buffer layer meet most requirements of a buffer layer in CIGS TFSCs. Therefore, highest efficiencies of CIGS TFSCs have been achieved when using CdS as the buffer layer. Nevertheless, wide band gap CIGS absorber could need a wider band gap buffer layer instead of the traditional CdS one, especially to reduce the cliff reported at WBG-CIGS/CdS. In this section, two different directions are investigated: (1) first the effect of alkali like Na, Li and K incorporation directly into the CdS during the chemical bath deposition is investigated, and (2) alternative buffer layers to CdS such as ZnS, ZnCdS, In_2S_3 and dual buffer layers (CdS combined with one of these previous buffer layers), are then investigated.

Samples preparation

In the first experiment, the alkali metals, Na, Li and K were introduced during the growth of the CdS buffer layer as well as on the Ga rich CIGS device. In a second experiment, the possible beneficial use of an alternative buffer layers is investigated. Towards this end, Ga rich CIGS absorber were prepared on FTO substrate as showed in section 4.2, the CGI and GGI ratios of the CIGS absorber were 0.7 for both respectively, annealed at 550°C. The absorbers were then divided into several samples, for the preparation of the different buffer layers. For all of them, absorbers were etched in KCN (2%) for 10 min, rinsed in deionized water and dried with nitrogen gas. The different buffer layers (CdS, CdZnS, ZnS, ZnS/CdS, In_2S_3, and In_2S_3/CdS) were deposited by chemical bath deposition, and Figure 4.13 summarized the different configurations.

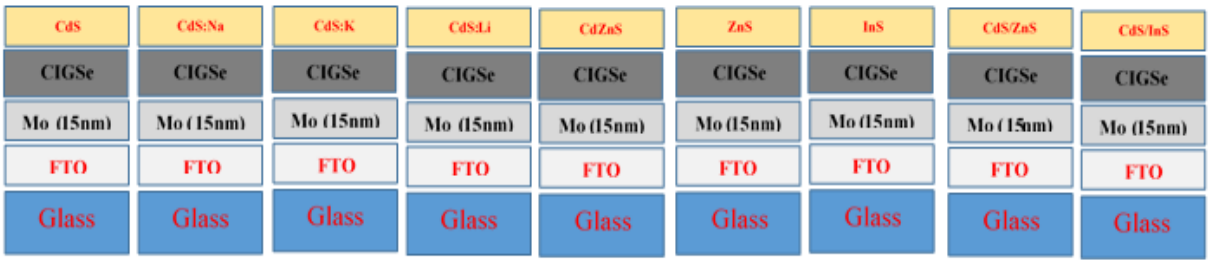

Figure 4.13: Scheme of CIGS on FTO substrate with different alternative buffer layers.

Result

In order to compare the photovoltaic parameters of the samples, figure 4.14 shows the box plots of the main electrical parameters Voc, Jsc, FF and η of the Ga rich CIGS devices fabricated using different CBD buffer layers, i.e., CdS, In_2S_3, ZnS or CdZnS and CBD double buffer layers CdS/In_2S_3 and CdS/ZnS. First, no efficiency was measured from the ZnS buffer. The data show that the cells fabricated with CdS exhibited the highest efficiencies due to the gain in Jsc. However, they suffer from low FF that reduces their efficiency, this drop in FF could be due to the interface recombination and increased series resistance. It is interesting to note that dual CdZnS/CIGS buffer layers shows a high FF around 60%, equivalent to that of CdS/CIGS devices. In contrast, for the doped-CdS there are not a clear improvement in the electrical parameters.

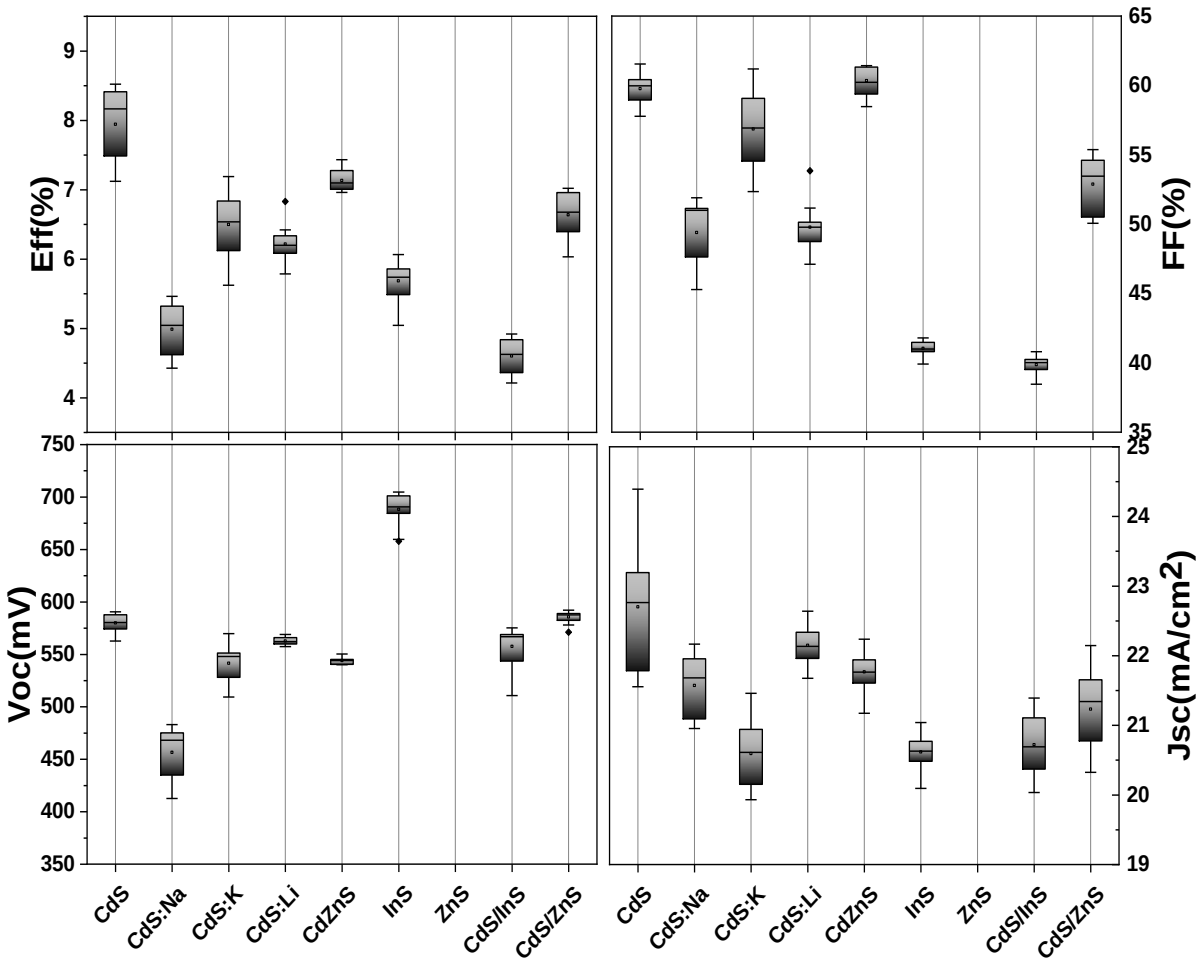

Figure 4.14: Illuminated parameters of the CIGS solar cells with deferent buffer layer.

Figure 4.15 shows the external quantum efficiency (EQE) spectra, comparing the EQE of the record cell obtained with different buffer layers with a cell with a reference CdS buffer. The most important observation is the clear EQE enhancement of the devices using In_2S_3 buffer, especially at region between 350 and 550 nm due to the decrease of absorption in the buffer at short wavelengths as the direct bandgap is much larger than that of CdS, rendering this potential buffer material appealing for the future substitute of CdS in Ga rich CIGS.

The different bandgaps between each sample cannot be related to the change of buffer layers. Therefore, it likely relates to sample variation, and a lack of reproducibility in the incorporation of Ga between the different absorbers. Hence, it is at this stage not possible

to draw conclusion on these EQE curves, and future experiments will need to firstly assess a perfect reproducibility in the absorber to properly comment on the effect of changing the buffer layer.

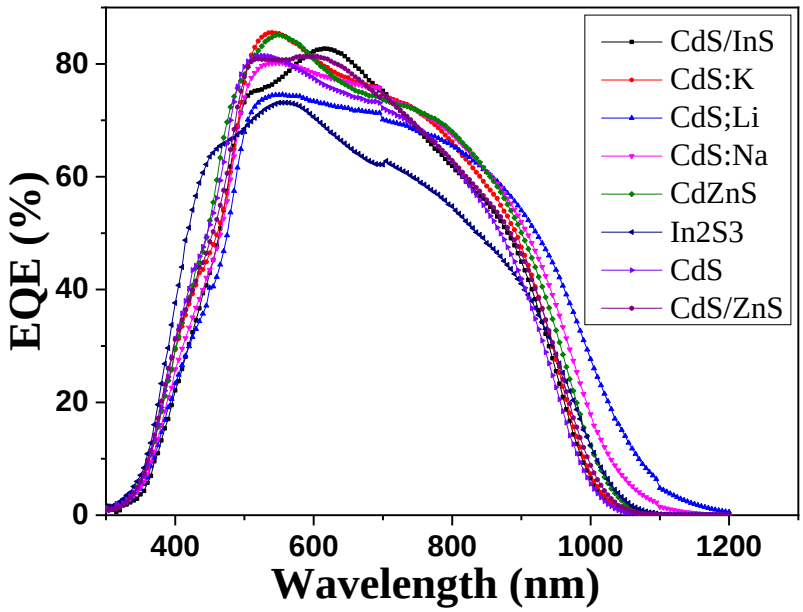

Figure 4.15: EQE for the Ga rich CIGS devices using different buffer layers.

4.6 Summary

In this chapter, a preliminary optimization of the GR-CIGS synthesis has been defined, the effect of the chemical composition was first investigated by varying the CIG and GGI ratios; the annealing temperature was then increased as a way to improve Ga incorporation and material quality; and finally different alternative buffer layers were considered to improve the band alignment and thus the device performance. All the materials have been prepared on transparent substrates based on FTO and a panoply of characterization techniques have been used (J-V characterization, XRD, Raman SEM) that lead to results that can be here summarized:

1- The optimal CGI range to obtain high conversion efficiencies Ga rich CIGS solar cells by sequential process was found to be comprised between 0.7 and 0.8.

2- The highest efficiency is obtained with devices annealed at 550°C. However, the best Voc is achieved with the absorber annealed at 600 °C correlated to a wider bandgap, which indicates a higher Ga incorporation to the chalcopyrite.

3- CdS buffer on Ga rich CIGS demonstrated higher efficiency than alternative buffers, however In_2S_3 on Ga rich CIGS demonstrated higher Voc.

Based on these previous results, a GR-CIGS-based TFSCs on FTO transparent substrate was optimized with an efficiency close to the state of the art on Mo.

Table 4.5: The main parameters of the record solar cell.

η (%)	V_{oc} (mV)	J_{sc} (mA/cm^2)	FF (%)	Rs [Ω.cm^2]	Rsh [Ω.cm^2]	*J0 (mA/cm^2)*	*n*
8.5	**588**	**24,3**	**60.2**	**1.75**	**533.35**	***2.3.10^{-4}***	***2.03***

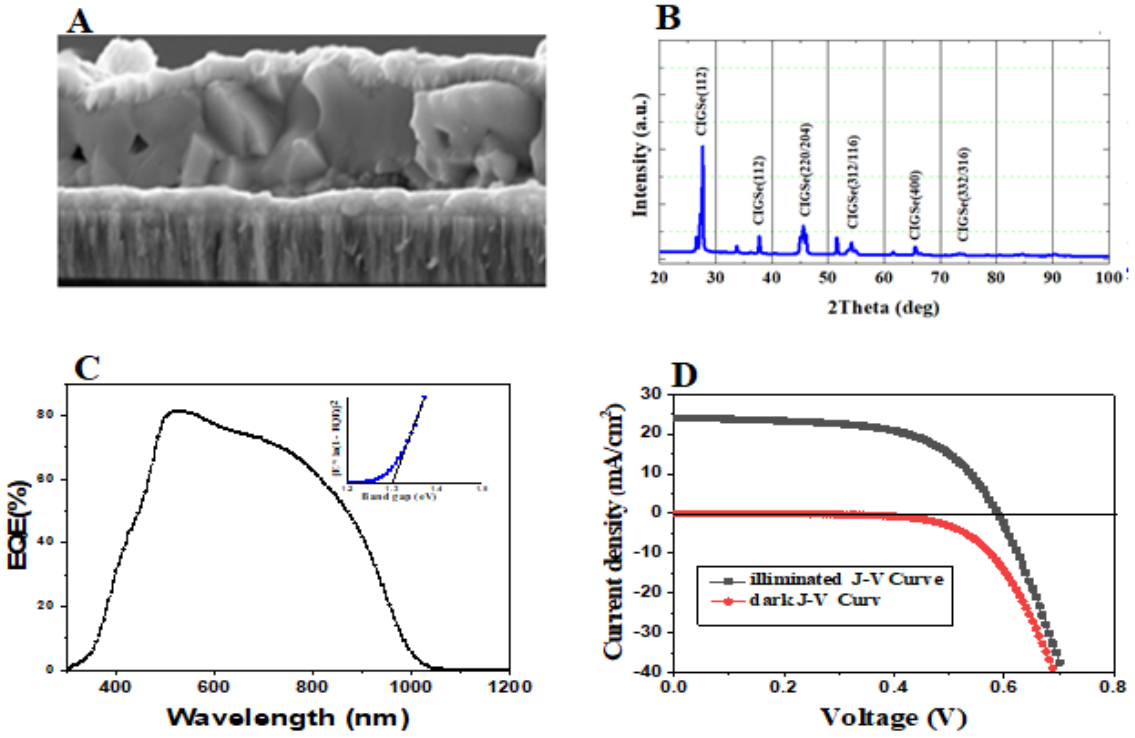

Figure 4.16: (A) Cross section SEM image, (B) XRD patterns, (C) EQE spectra, (D) characteristic for the best cell.

The experimental results of this chapter will serve as the baseline for future experiments aimed to further enhance the efficiency of GR-CIGS solar cells on transparent substrate, using strategies that enhance the efficiency of CIGS thin film solar cells.

5 Effect of alkali metal atom doping on Ga rich CIGS absorber

5.1 Introduction

The recent progress in the efficiency of CIGS technology up to 23.35% is mainly due to the application of several strategies, as previously shown in Figure 2.19, such as band gap grading, Na incorporation and heavier alkalis (Cs, Rb and K) PDT on CIGS absorber. Therefore, a similar approach is followed to improve the efficiency of Ga rich CIGS TFSCs on FTO. Taking into consideration that a uniform band gap grading approach is well suited for the top cell absorber in tandem solar cells, this chapter focuses only on the incorporation of alkali elements.

Since early 1990s[162] , alkali metal atoms (Na, Cs, Rb, and K) incorporation into the CIGS absorber has become essential in the fabrication of high-efficiency CIGS solar cells. In section 2.8, we have discussed the methods and utility of alkali elements doping on CIGS solar cell. In this chapter, we investigated the benefits of alkali elements incorporation on the electronic and structural properties of Ga rich CIGS absorber layers growth on FTO substrate, as introduced in the previous chapter. In a first section, we investigated the effect of a pre-deposition treatment using Na (Na Pre-DT) on the performance of Ga-rich CIGS solar cells through a complete characterization of materials and devices. In a second section, we investigated the effect of Cs and Rb post-deposition treatments (CsF-PDT and RbF-PDT) on both undoped or optimized doped Na Pre-DT Ga-rich CIGS, as a way to improve the Ga incorporation in the film and/or modify the species diffusion dynamics. Overall, the material and device properties were evaluated by using a complete panoply of characterization techniques: J-V and EQE for the device performance, X-ray diffraction (XRD) and Raman spectroscopy for the crystalline structure, scanning electron microscopy (SEM) for the film's morphology, and glow discharge optical emission spectrometry (GDOES) to determine the alkali depth profile in the CIGS layer.

5.2 Effect of Na Incorporation on Ga rich CIGS absorber

Since the first observation of the beneficial effects of Na Incorporation into CIGS absorber layer, several leading research groups have used this strategy in order to improve the photovoltaic performance of CIGS solar cells. As mentioned in chapter 2.8, the presence of Na during the growth of CIGS absorber induces beneficial changes in the material and device quality, including increases in the Voc, FF, grain size, conductivity and also preferential grain orientation, that results in an improvement of the efficiency. As already mentioned in section 2.3, the FTO acts as a barrier for Na diffusion from SLG; thus, in this section the influence of the Na has been investigated through the deposition of NaF layers prior to the CIG precursor deposition (Na-PreDT).

Sample preparation

In order to investigate the positive effect of Na presence on the performance of Ga rich CIGS solar cells, Ga rich CIGS thin film devices fabricated with optimized composition defined in the previous chapter, i.e., Cu-poor condition (GIG = 0.70 and CIG= 0.70) prepared onto FTO substrates, as described in section 4.2, with and without Na deposition treatment. The Na was incorporated through the deposition of an ultrathin NaF layer onto the metallic precursor. Different thicknesses of NaF layers were deposited but for lecture clarity of the effect of Na, only the optimized 15nm thickness is here reported. XRF analysis revealed CGI and GGI ratios of 0.7 and 0.68 respectively, corresponding to material bandgap of Eg = 1.45eV.

Results

First of all, the blocking behaviour of the FTO for Na diffusion is confirmed by the presence of Na only in the doped absorber, as shown in Figure 5.1.

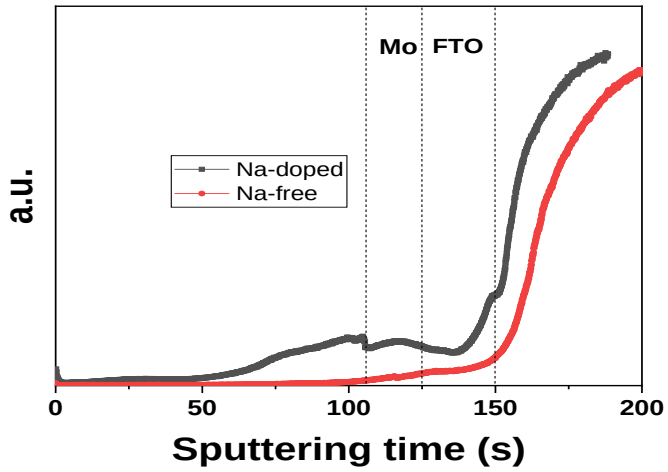

Figure 5.1: Sodium profile obtained from GDOES measurements of the devices without and with Pre-NaF.

Figure 5.2**Error! Reference source not found.** shows the SEM images of the doped sample and reference sample with a similar magnification. The morphology of both samples appears similar at first sight; both samples have a decrease in quality toward the back interface and a bilayer aspect is seen with much smaller grains. The back side of the absorber is where a Ga accumulation is expected [163]; those images hint at a possible phase segregation without the possibility to conclude on differences stemming from the presence of sodium.

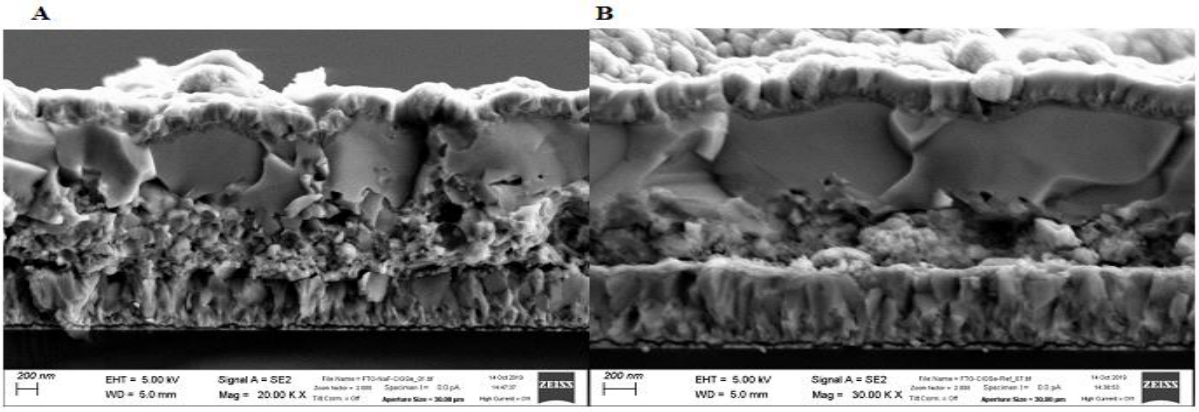

Figure 5.2: Cross-section SEM images of CIGS grown on FTO A) without and B) with Na/PreDT.

To complement the visual observation, doped sample and reference are analysed by X-Ray Diffraction, with a specific focus on the (112) and (220)/(204) peaks, as shown Figure5.3. A clear difference can now be made between both samples. Without Na, 2 different phases are observed, a feature particularly visible for the (112) peak with a Ga-poor and a Ga-rich contribution, indicating a strong inhomogeneity in the incorporation of Ga to the CIGSe matrix. In the presence of Na however, a well-defined single peak, a result consistent with a more homogeneous material and thus a better Ga incorporation to the CIGSe matrix. A phase segregation may still exist for this sample, but to a level low enough to be below the instrument's resolution. Regarding the (220)/(204) peaks, a peak splitting is expected for high Ga content samples due to the c/a axis distortion of the tetragonal structure rather than phase separation [164]; in the case of doped sample, 2 peaks are indeed observed, along with a much smaller shoulder at 45.55°; the latter could be attributed to a limited phase separation, which was not visible in Figure5.3. For reference sample however, 3 well defined peaks are visible, indicating again a clear phase separation between a Ga-poor and a Ga rich layer, much more pronounced than in the presence of Na.

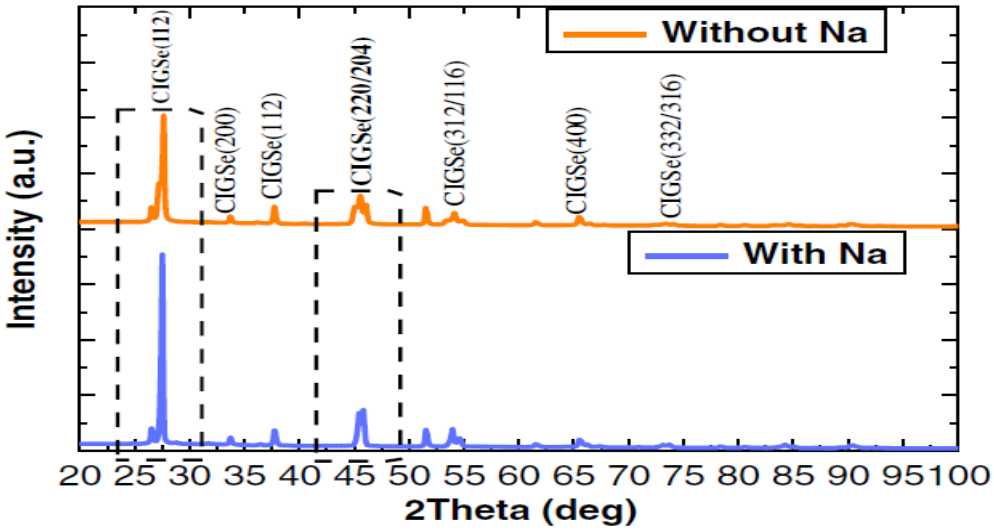

Figure 5.3: XRD pattern of CIGS films without and with Na incorporation.

The samples' depth composition is a critical parameter of this study, and specifically the Ga and Na profiles. Using the GDOES analysis presented in **Error! Reference source not found.**4, several remarks can be made: (1) for both sample, a Cu depletion is observed near the front interface, hinting at the presence of an OVC phase though not unequivocally demonstrating it; (2) both samples exhibit a single Ga grading profile, with a steep accumulation toward the back interface, and without appreciable difference between both samples; (3) very little differences are observed in the In and Se profiles, a result anticipated as both samples are processed within the same batch; (5) The Na element is as expected present throughout the absorber for doped samples, while the analysis of reference sample confirms that FTO is an efficient barrier for its diffusion from the SLG substrate. Finally, and as a general observation, it is interesting to note that no sample shows specific features from an elemental depth composition viewpoint.

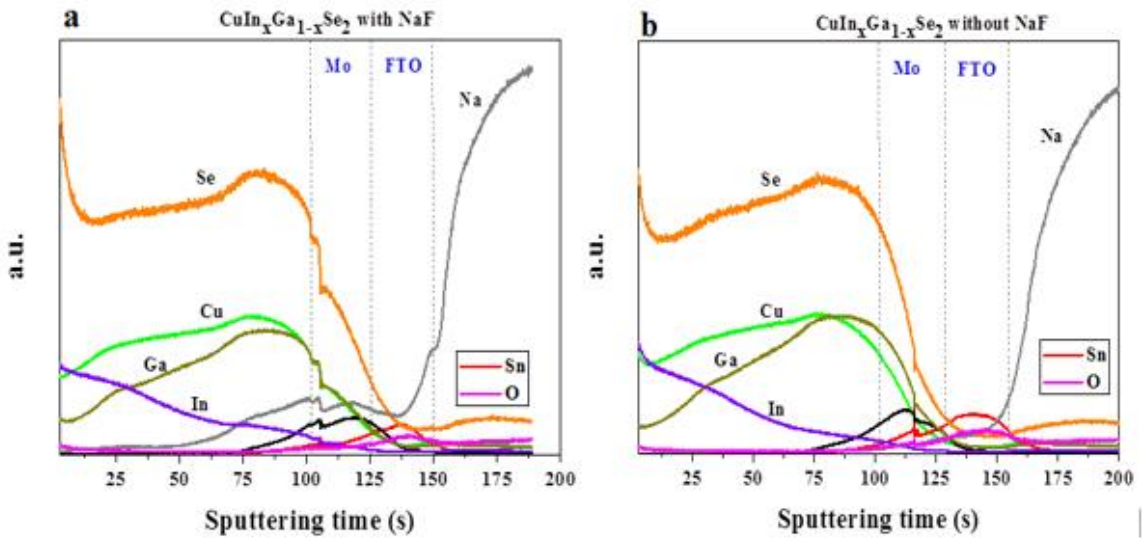

Figure 5.4: Depth Profile Analysis (GDOES) of a wide bandgap CIGS layer on FTO substrate, a) with sodium and b) without sodium.

Raman spectroscopy is a valuable tool to dwell in the Na-PreDT influence regarding the film properties, and we chose an approach based on 2 excitation wavelengths; a high energy excitation of 325nm extremely sensitive to the samples surface, and a more standard 532nm excitation allowing a deeper probing of the films. The Raman spectra are shown in Error! Reference source not found. for 325 and 532nm excitation wavelengths respectively, f or doped sample and no-doped sample . In both cases, the power density was kept below 25 W.cm^{-2} to avoid any substantial heating of the samples. The spectra were acquired on five different positions of a 1.25 x 2.5 cm² sample. It is important to note that these systems have not been previously studied under 325 nm excitation, and a direct quantitative spectra comparison between 532 and 325 nm is thus not possible. Our study focus then on comparing films with and without the Na PreDT under a similar excitation wavelength. For both wavelengths, the spectra are characterized by a dominant peak around 180 cm^{-1}

followed by smaller contributions. The peak at 180 cm^{-1} is identified with the A1 mode of the Cu(In,Ga)Se_2 in the chalcopyrite structure (space group $I\overline{4}2d$) with a [Ga]/([Ga]+[In]) ratio in the range of the 50-60%, consistent for both excitation wavelengths [165][166]; a value slightly lower than determined by XRF, but in line with the expectations, as it was shown that a significant part of the Ga is accumulated at the back side of the films. Additional weak contributions at 195, 223, 242 and 257 cm^{-1} are observed for the 532 nm excitation (**Error! Reference source not found.**b), and at 146 cm^{-1} for the 325 nm excitation specifically (Figure 5.5 a); identifying the origin of these contributions is not trivial. The 195 cm^{-1} contribution can possibly be attributed to the Cu-Au Cu(In,Ga)Se_2 structure (space group $P\overline{4m}2$), showing similitudes with the very cooper-poor $CuInS_2$ case [167]. This would however be, to our knowledge, the first time that such phase is reported in Ga-rich CIGSe samples, and caution should thus be exercised.

The 146 cm^{-1} peak observed under UV conditions only (325 nm excitation, Figure 5 5a) has several possible interpretations. It can firstly be ascribed to a resonant enhancement effect of the Cu(In,Ga)Se_2; however, one should note that it could also be associated with the presence of an OVC rich in Ga [168][169]. To unequivocally identify the origin of this peak, a more detailed analysis using a known reference samples would be necessary. Finally, the complex structure in the region of the 200-260 cm^{-1}, which is visible for both excitations, is associated with the E and B modes of the chalcopyrite structure of CIGSe and their variations are related to the ratio of the Ga/(Ga+In) in the CIGSe solid solution. However, the overlapping of the OVC and Cu-Au contributions cannot be discarded.

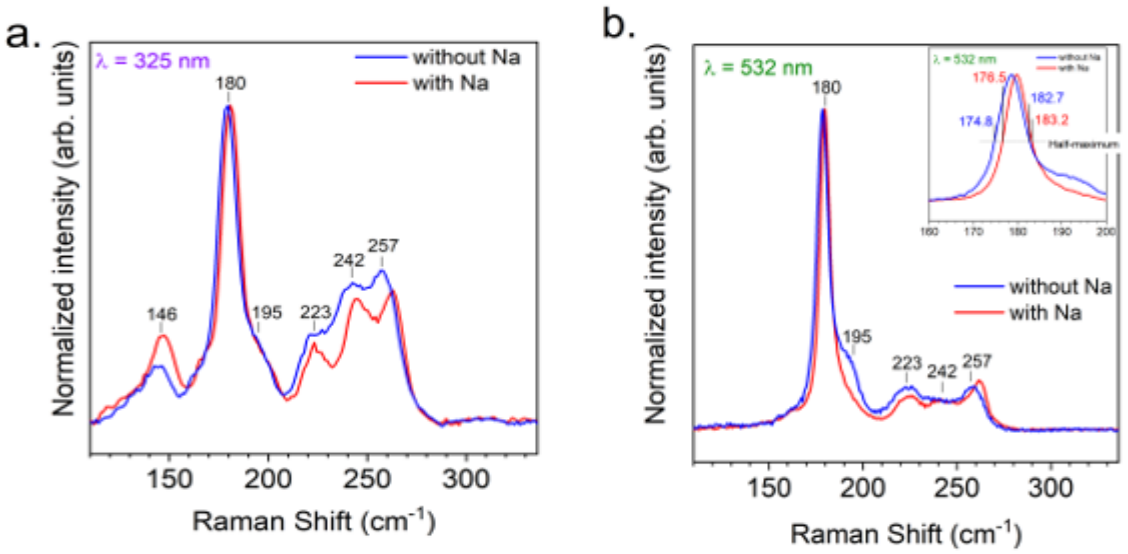

Figure 5.5: Raman spectra of doped sample and no-doped sample obtained using the 325nm (a) and the 532nm excitation wavelengths (b).

The comparison of the sample's spectra shows that clear differences exist between both. Focusing on **Error! Reference source not found.**b (532 nm excitation) only, the main peak of the CIGSe is slightly shifted, suggesting a higher Ga ratio in the Na-PreDT samples, possibly 5% to 10% higher. This agrees well with the shift and the relative intensity of the weak peaks in the 220-260 cm^{-1} region observed under 532 nm and the similar shift observed under 325 nm excitation. As the GDOES analysis showed a similar Ga elemental profile between both samples, this result tends to indicate a better Ga incorporation to the CIGSe matrix in the presence of Na close to the surface. This observation is consistent with previous work on Na doping of CIGSe absorbers. Remarkably, the 195 cm^{-1} contribution associated with the Cu-Au structure is absent in doped sample (Na-PreDT sample) under 532nm excitation, while it appears for both samples under 325nm excitation. While the presence of this phase has been associated with a degradation of the devices performance,

previous studies by our group on $CuInS_2$ device [167] showed an improvement of the J_{sc}, but a reduction of the V_{oc}, and R_s. This was ascribed to a reduction of the defect concentration in the Cu-poor $CuInS_2$ by the accumulation of these defects in the more disordered Cu-Au phase, hence allowing a better crystalline quality in the chalcopyrite $CuInS_2$. It is unconfirmed if a similar conclusion is applicable here.

Focusing again on 532nm excitation (**Error! Reference source not found.**b), the FWHM of the main 180 cm^{-1} peak is markedly reduced in doped sample (from 7.9 to 6.7 cm^{-1}). This indicates that the Na-PreDT is associated with an improvement of the crystal quality of the CIGSe, which would be in agreement with the reduction of the Raman contributions of the Cu-Au disordered phase. Finally, a small shoulder in the 155-165 cm^{-1} region is observed in doped sample Figure 5.5 b), and it is attributed to the presence of the OVC. This phase allows to accommodate the Cu-poor conditions of the absorber; the order of the defect in the structure allows to obtain an absorber with better optoelectronic properties [170].

As a summary of the Raman analysis of the samples, two main observations should be kept in mind. The most important one is that Na-PreDT significantly improves the Ga incorporation in the CIGSe structure (by 5% to 10% in our estimation), as shown by the peaks shift for both excitation wavelengths; and secondly, a possible improvement of the general crystalline quality of the films can also be attributed to the Na-doping, illustrated by the reduced FWHM of the 180 cm^{-1} peak in **Error! Reference source not found.**b. A similar observation can however not be made in **Error! Reference source not found.**a, and this should remain at this point an hypothesis as different interpretations (additional contributions) may exist for this FWHM difference.

Figure 5.6 and Table 5.1 show the JV characteristic of samples along with their respective photovoltaic and diode parameters of the best devices obtained from the reference and Na-PreDT GR-CIGS absorbers. No ARC has been used in the device fabrication. A remarkable improvement of the performance is observed for the device with a Na-PreDT; specifically, the Fill Factor jumps from 60.3% to 65.6%, and the V_{oc} is brought from 588 to 668mV. A similar observation was made in reference regarding the influence of Na on these two parameters. While a slight reduction of the current is observed from 24.3 mA.cm^{-2} without PreDT down to 23.2 mA.cm^{-2} for doped sample, the efficiency is markedly improved and reaches a record value of 10.15%. This value is the main result of this work, and it is to the best of our knowledge the highest reported efficiency for a CIGSe solar cell on transparent substrate with a bandgap larger than 1.4 eV, getting close to those obtained with similar absorbers fabricated on metallic Mo substrates. It should also be noted that it was obtained without an antireflection coating, and there still exists a straightforward margin for improvement in that regard. The fitting of the dark JV curves using a single diode model reveals that both the shunt resistance and reverse saturation current are improved by the Na-PreDT in doped sample. This observation is consistent with a possibly improved film morphology observed in the Raman analysis in Figure 5.5 b. The Na-PreDT, by improving the film crystallinity, would reduce both the shunt pathways along with the density of recombination centers, the latter being closely related to J_0 [171] yielding an overall superior diode performance.

Table 5.1: Comparison of cell parameters between the best cells achieved in the reference and doped samples.

Device	η (%)	V_{oc} (mV)	J_{sc}(mA/cm^2)	FF(%)	Rs [Ω.cm^2]	Rsh[Ω.cm^2]

Without NaF	8.51	588	24.3	60.3	1.75	533.35
With NaF	10.15	668	23.19	65.6	1.2	902.11

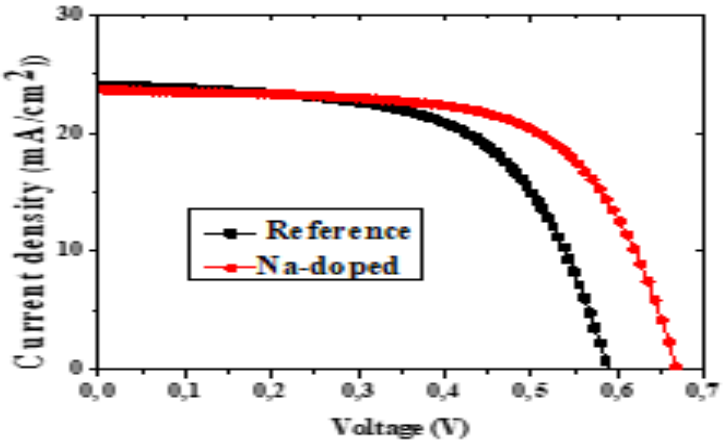

Figure 5.6: Current Voltage curves under illumination for the sample.

The EQE analysis of samples is presented **Error! Reference source not found.**. A clear d ifference in the bandgap between both samples is visible, and while the GDOES composition analysis indicated a roughly similar GA profile in the films, such difference comes to no surprise; the XRD analysis indicated a clear phase separation in reference sample (no Na), with a poor homogeneity in Ga incorporation and thus a Ga-poor phase reducing the bandgap of the absorber. Doped sample on the other hand exhibited a more homogeneous Ga incorporation, resulting in a material with an overall higher bandgap. The Raman characterization additionally confirmed this observation that Na-PreDT leads to a better Ga incorporation in the CIGSe. The normalized EQE onset at the vicinity of the bandgap is also steeper for doped sample, an indication of a better collection of charge carriers generated from low energy photons, and thus of an improvement of the back interface's quality of the absorber. A result consistent with a material with a lower level of phase segregation[172].

For a direct bandgap, the absorption coefficient depends on $\alpha h\nu \propto \left(h\nu - E_g\right)^{1/2}$. Hence, a plot of $h\nu \times ln(1 - EQE)^2$ against $h\nu$ gives a reasonable extrapolation of the electronic bandgap E_g, as shown in the inset of **Error! Reference source not found.**. Using Na-PreDT, E_g is increased from 1.32 to 1.41eV, an effect fully attributed to the better and more homogeneous Ga incorporation discussed during the XRD and Raman analysis [172].

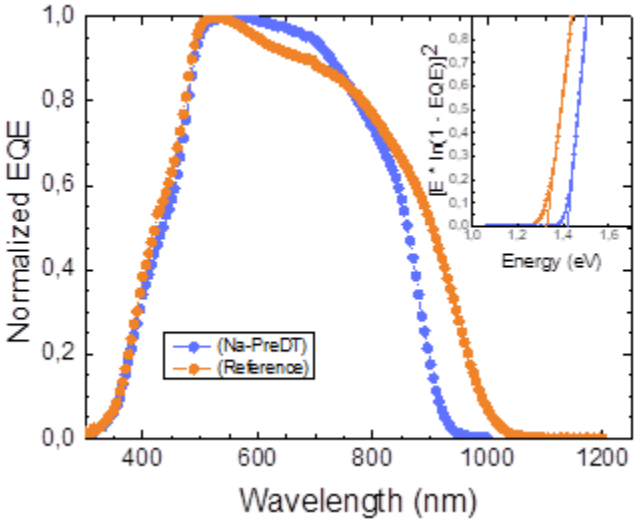

Figure 5.7: Compared Normalized External Quantum Efficiency of reference and doped samples. Inset: bandgap determination plot hv×ln(1-EQE)^2 against hv.

5.3 Influence of heavy alkali postdeposition treatment on Ga rich CIGS

Sample fabrication

In this section, we investigated the impact of heavier alkali metals (Cs and Rb) PDT on the material and device properties of Ga rich CIGS. For this purpose, two series of undoped and Na-doped CIGS absorbers were prepared as described in the previous section, both set of absorbers having similar chemical composition, as shown in Table 5.2. Figure 5.8 shows the procedure used for the preparation of these samples. The as-annealed CIGS absorbers were

first subjected to KCN etching to remove any possible secondary phases. A thin layer of RbF or CsF was then thermally evaporated on the absorber with different thicknesses (15, 20, and 25 nm). A soft thermal treatment at 350 °C at 1 bar (under Ar and Se atmosphere) for 20 minutes was then applied in order to diffuse the alkali elements into CIGS absorber film, and then letting it cooling down naturally. KCN etching was also realized again after the second selenization, and the solar cells completed as described in section 3.1.

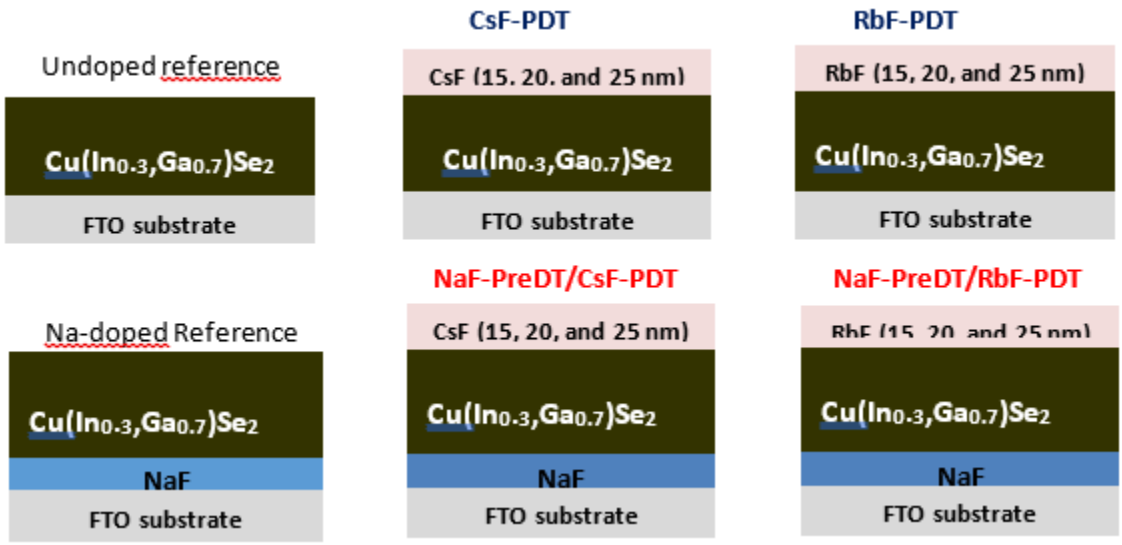

Figure 5.8: Schematic description of the PDT (for Cs and Rb alkali) process on undoped and Na-doped CIGS absorbers.

Table 5.2: Composition of the undoped and Na-doped absorbers measured by XRF.

Absorber	d(µm)	Cu(% at)	In(% at)	Ga(% at)	Se(% at)	CIG	GIG
Undoped reference	1.70	19.28	9.33	22.29	49.50	0.60	0.70
Na-doped	1.66	19.37	9.59	22.10	48.95	0.61	0.69

Results and discussion

A- Effect of CsF PDT on GR-CIGS absorber

Figure 5.9 shows the XRD patterns of all the processed samples. All the peaks positions corresponding to the crystalline orientations (112), (220)/(204), (312)/(116), (112),

(400/008), (332/316) of the chalcopyrite structure, the (101) one of the $MoSe_2$, and the (220) and (221) ones of the FTO, are shown in the figure. A strong preferred growth orientation (112) peak at around 27.6° and minor peaks (220)/(204) at 45° and (312)/(116) at 54° are observed in all the cases, with small differences between the samples. This indicates that the alkali PDT could have an effect on the preferred orientation of the CIGS.

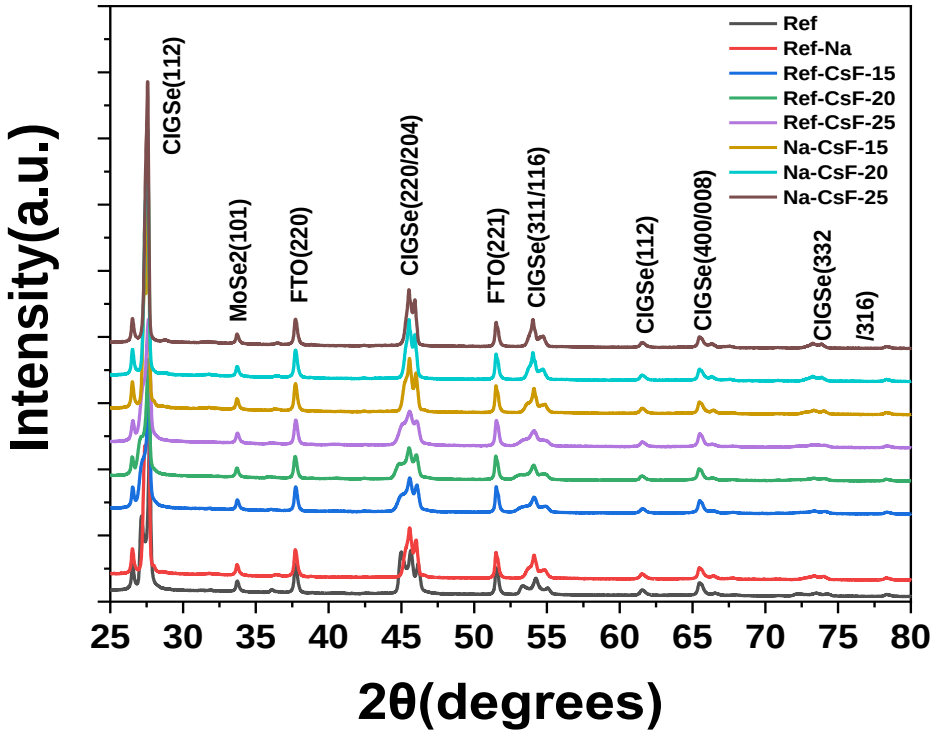

Figure 5.9: XRD patterns of CsF-PDT on Ga rich CIGS films onto FTO substrate without and with Na PreDT.

Figure 5.10 (A), (B), (C) and (D) show the XRD fine scans of the chalcopyrite (112) and (220)/(204) peaks of CsF-PDT on Ga rich CIGS films with and without Na-PreDT treated using different thicknesses of CsF layer. Table 5.3 summarizes the peak positions, peak intensities, ratios and FWHM derived from XRD measurements of the prepared films. (112) and (220)/(204) peaks shifted towards lower angles as the CsF thickness increased, indicating for a lattice constant enlargement. The smallest full width at half maximum (FWHM) value

in Table 5.3 of the films treated with NaF-PreDT and CsF-PDT are indicative of an improvement in crystal quality and consequently larger grain sizes. The formation of a single-phase CIGS compound was confirmed by the presence of a single peak (112) for the samples combining Na-PreDT and 20 or 25 nm of CsF-PDT, as shown in Figure 5.10 (B). The situation is different for the samples without Na and for large amounts of CsF (see below). These observations clearly demonstrate that the CsF-PDT treatment on Na-doped GR-CIGS absorbers lead to a better homogenization and high crystalline quality, and that there is probably a synergistic interaction between Na and Cs. An increase in the (220/204) peak intensity peak and shift of the (220/204) peak to lower angles was also observed. The intensity of (112) peak was obviously enhanced, indicating that the crystalline quality of CIGS films was improved when the CsF-PDT on Na-doped CIGS absorbers, as shown in Figure 5.9.

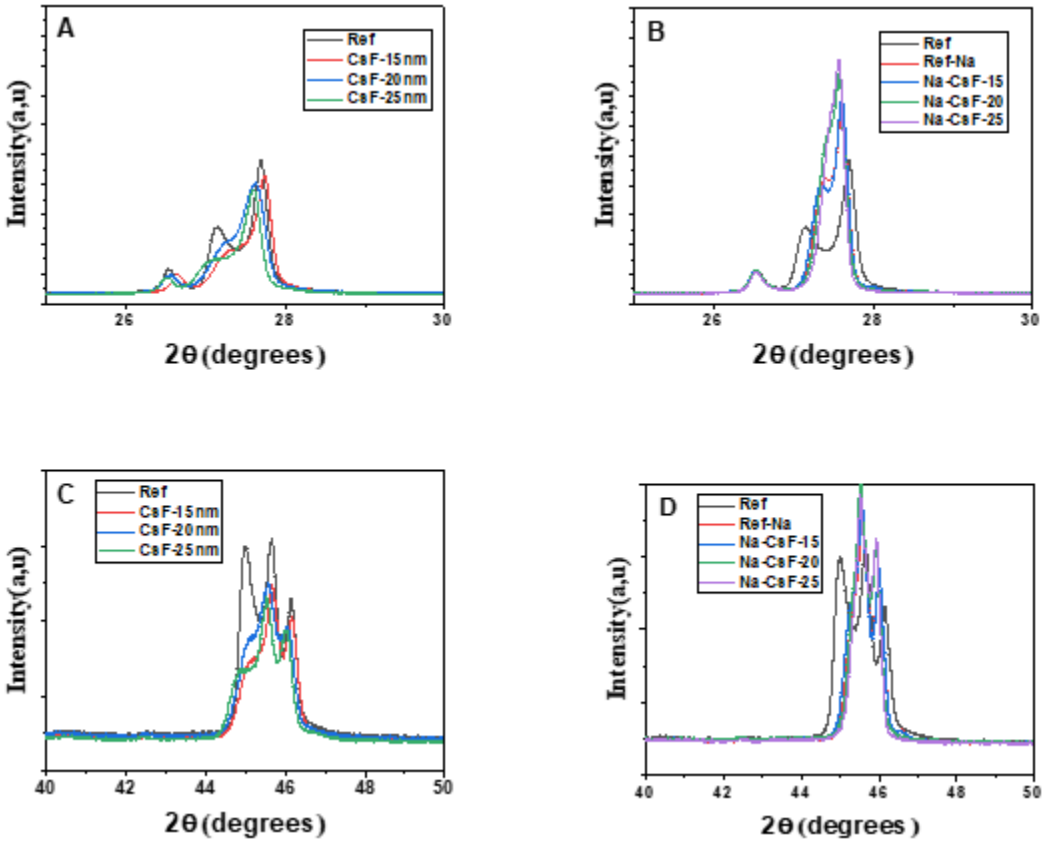

Figure 5.10: XRD diffraction patterns for (112) and (220)/(204) reflection peaks for the CsF-PDT samples. (A) undoped CIGS (112) peak, (B) Na-doped CIGS (112) peak, (C) undoped CIGS (220)/(204) peak, and (D) Na-doped CIGS (220)/(204) peak.

As already commented, the FWHM of (112) peak improvement for the films combining NaF PreDT and CsF-PDT indicating an increase in grain size could be related to an increased Ga diffusion favoring a single-phase formation. This improvement is linear with the thickness of the CsF layer until 20 nm, while for the CsF-PDT on undoped GR-CIGS films there is no clear correlation between the CsF thickness layer and the FWHM of the (112) peak. The I(220/204)/I(112) ratios were also calculated to evaluate the preferential crystal growth of the Ga rich CIGS films, confirming that the (112) orientation is someway improved when adding Na and CsF. The average sizes of crystallites in the Ga rich CIGS samples obtained by the XRD patterns were also evaluated and are shown in figure 5.11. In this case, the size is increasing with a maximum for the Na-CsF-20 sample. In the next section, it will be shown

that a correlation can be found between the I(220/204)/I(112) ratios, crystallites sizes and efficiency of the devices.

Figure 5.11 shows average sizes of crystallites in the Ga rich CIGS samples obtained by the XRD patterns, a clear improvement in the grain size for the samples treated with CsF-PDT and Na-PreDT, the biggest grain size obtained with Na-Cs-20 sample which presented the best efficiency.

Table 5.3: Peak position, peak intensity, ratios and FWHM derived from XRD measurements of CsF-PDT Ga rich CIGS films with and without Na-PreDT.

Film	**CIGS (112)**		**CIGS (220/204)**		**I(112)/I(220/204)**	**FWHM (112)**
	2θ[degrees]	I[counts]	2θ[degrees]	I[counts]		
Ref	27.69	48293	45.65	15546	3.10	0.79
Ref/15-CsF	27.74	43238	45.67	12428	3.47	0.63
Ref/20-CsF	27.62	40341	45.57	12596	3.20	0.66
Ref/25-CsF	27.60	38327	45.53	11554	3.31	0.61
Ref-Na	27.61	67038	45.57	17383	3.85	0.40
Ref-Na15-CsF	27.61	69242	45.55	18558	3.73	0.44
Ref-Na20-CsF	27.57	77703	45.51	20292	3.82	0.34
Ref-Na-25-CsF	27.56	82195	45.52	19311	4.25	0.61

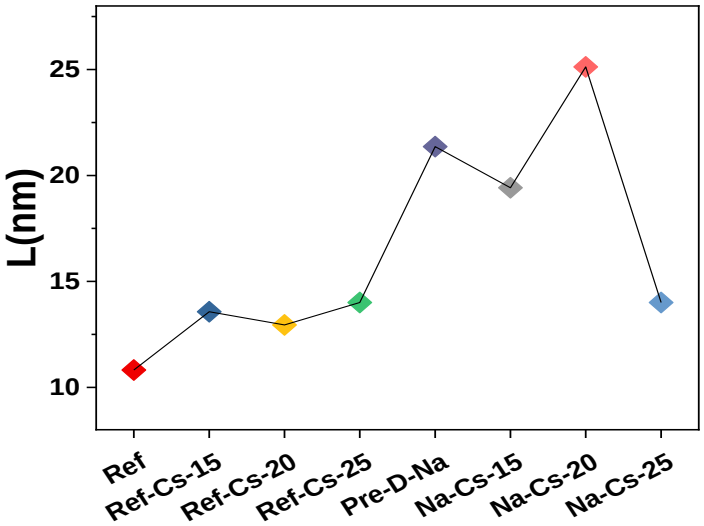

Figure 5.11: Effect of CsF-PDT on the crystallite size of Ga rich CIGS.

Effects of CsF-PDT on the performance of the devices

To compare devices photovoltaic parameters between them, the differences in the main photovoltaic parameters between the best cell of the reference sample and the best cell of each sample were calculated as listed in Table 5.4. The highest efficiency has been obtained using 20 nm CsF-PDT on Na-doped CIGS with 11% with a bandgap of 1,35 eV (figure 5.9). Figure 5.12 shows also boxplots of the electrical parameters of for the different solar cells. From these data, the first observation that could be made, is that all the sample fabricated with CsF-PDT on Na-doped CIGS (except for the highest CsF content) exhibited a higher performance than the undoped. As previously commented this electrical behaviour follows the same trend shown by the crystallite size.

Table 5.4: Relative comparison of the main photovoltaic parameters for the best cells obtained with the CsF-PDT

Device	**Jsc (mA/cm^2)**	**Voc (mV)**	**FF (%)**	**η (%)**	**Rsh ($\Omega.cm^2$)**	**Rs ($\Omega.cm^2$)**
Ref	**24.69**	**604**	**64.38**	**9.60**	**1010**	**1.8**
Ref-15-CsF	21.87	609	60.85	8.11	866	3.1
Ref-20-CsF	23.06	625	64.67	9.33	1340	1.93
Ref-25-CsF	23.45	603	61.96	8.77	1516	2.7
Ref-Na	24.33	623	62.66	9.78	1054	2.3
Ref-Na15-CsF	23.87	634	64.60	0.19	1276	3.3
Ref-Na20-CsF	25.72	658	64.91	11	2204	1.4
Ref-Na-25-CsF	23.57	606	61.13	8.74	944	2.9

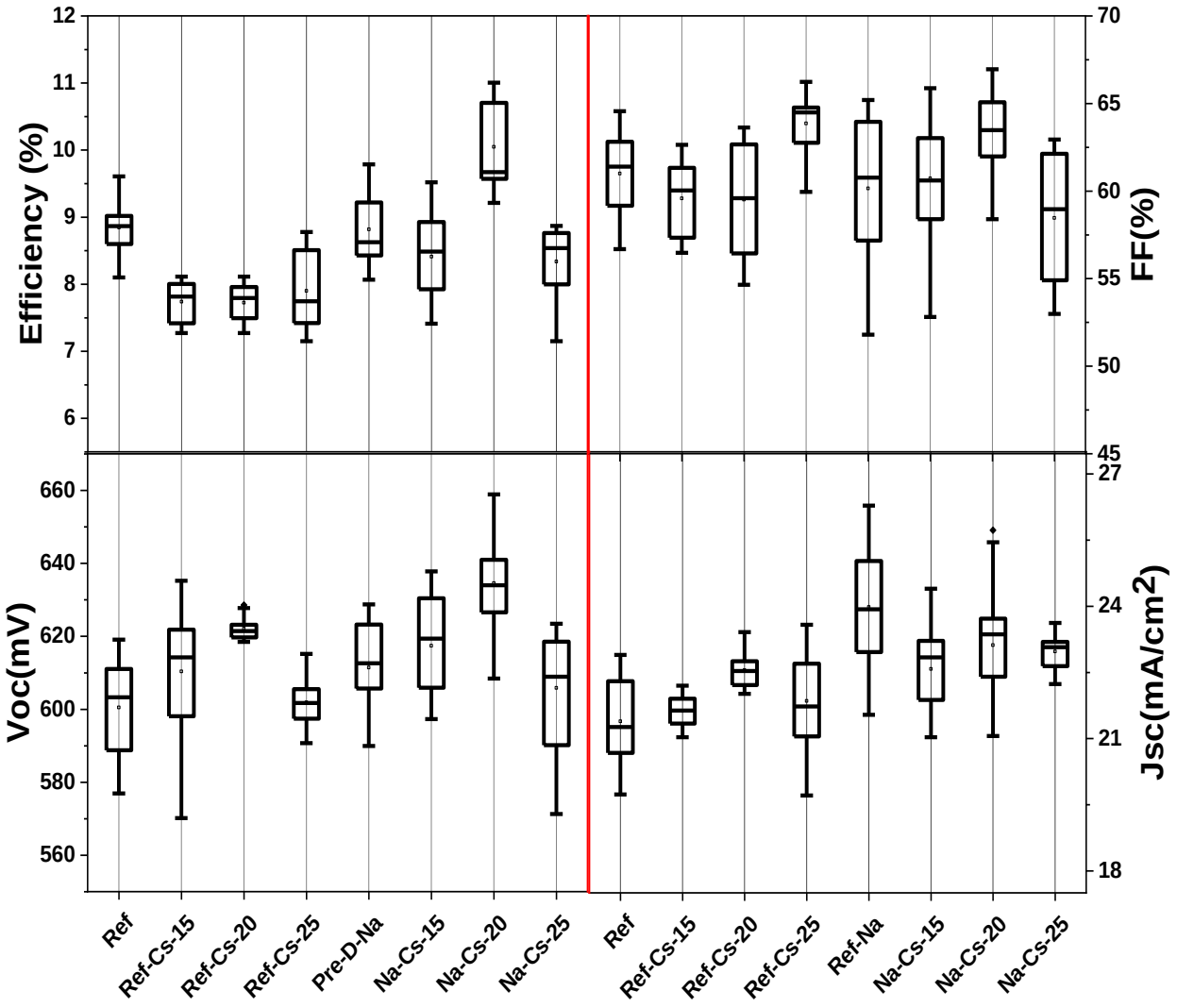

Figure 5.12: Boxchart of the main solar cell parameters of the devices.

The efficiency improvement is mainly due to the increase of both V_{OC} and R_{Sh} while J_{sc} and the FF of devices remained mostly unchanged. The Voc of the CsF-PDT devices are higher than those of the reference and starts to decreases if the CsF thickness exceeds 20 nm. The increase in Voc could be attributed to the crystallinity quality as confirmed from the XRD measurements in addition to the Rsh increase, which greatly reduces the interface recombination. The decrease observed in the Jsc of CsF-PDT devices as compared to the references devices could be caused by a reduction in the space charge region due to CsF-PDT [155]. The highest efficiency (11%) is obtained for the sample treated with Na-PreDT/CsF-PDT (20nm), as shown in Table 5.4, and there is a clear correlation between the XRD results and the performance for the devices combining Na-PreDT and CsF-PDT. In

contrast for the Na-free samples, there is no clear trend between the devices performance and the CsF-PDT content. Figure 5.13: shows the J(V) characteristics and the EQE curves which were measured for the best cell of each sample.

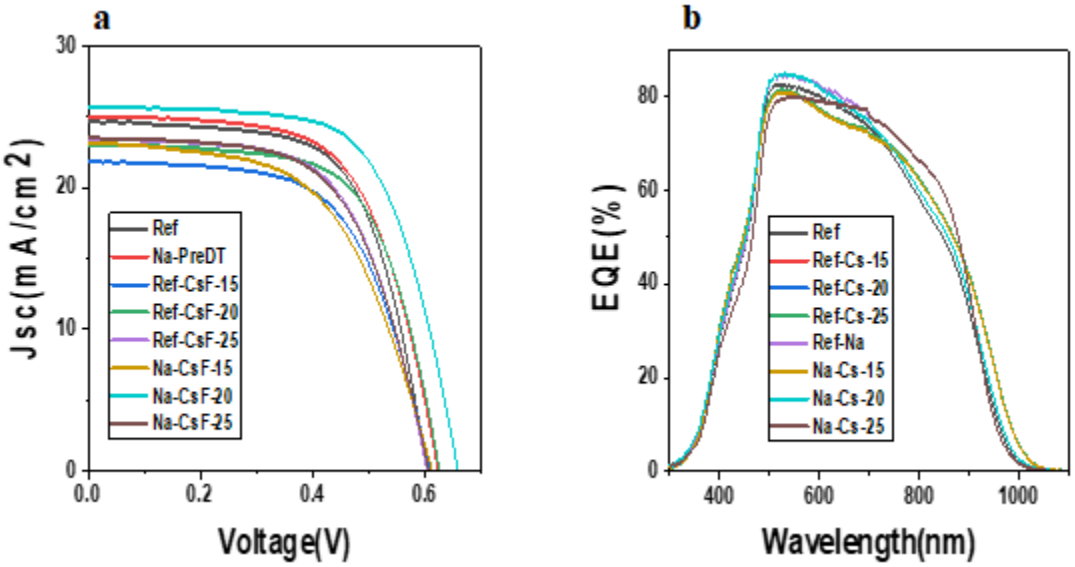

Figure 5.13: (a) J(V) characteristics and (b) EQE curves of the best cells of the CsF containing samples set.

As conclusion, it has been seen that CsF-PDT on Ga rich CIGS absorber has beneficial effects on the device performance, especially in the presence of Na, which means that the incorporation of Na into Ga rich CIGS absorber is critical to take advantage of the CsF-PDT, showing a clear synergistic effect of both alkalis.

B- Effect of RbF PDT on Ga rich CIGS absorber

Figure 5.14 shows the XRD patterns of the Ga rich CIGS absorbers grown with and without Na and RbF- PDT. The main peaks have been observed on the surface of the CsF-PDT samples in the previous section are shown in RbF-PDT with small shifts, (112), (220)/(20 4), (312)/(116) (112) (400/008.

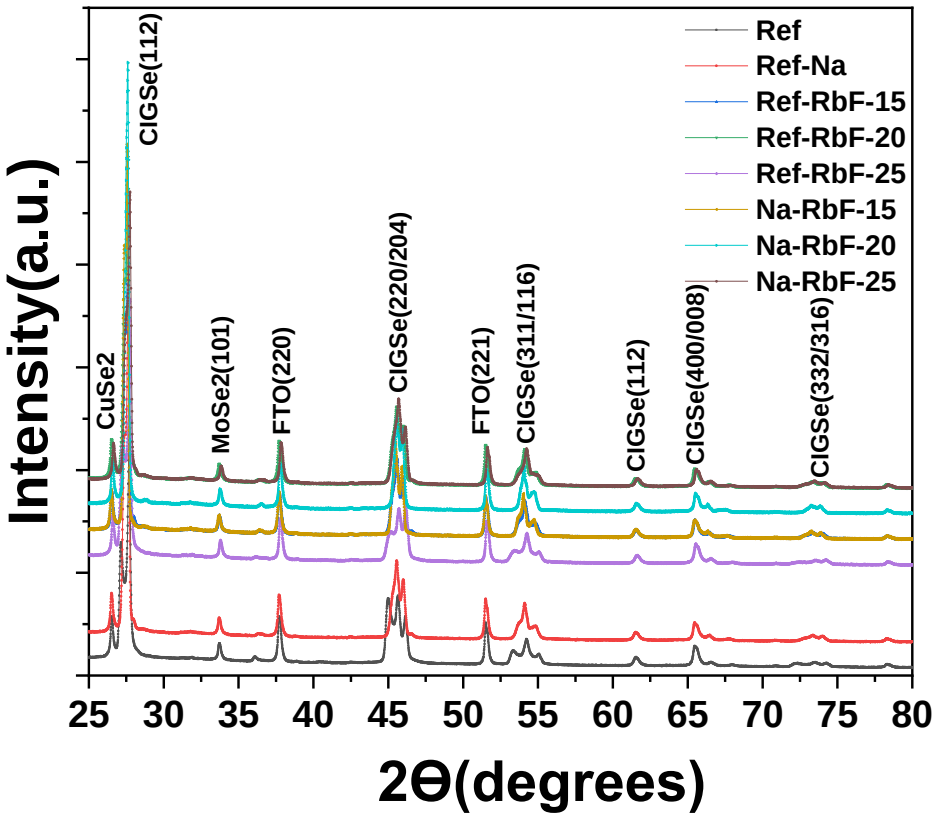

Figure 5.14: XRD patterns of RbF-PDT on Ga rich CIGS films onto FTO substrate without and with Na PreDT.

Figure 5.15 (A, B,C and D) and Table 5.5 show the XRD main peaks of Ga rich CIGS films with and without NaF PreDT treated with RbF-PDT along with the peak position and peak intensity. RbF-PDT films show a narrower FWHM compared to CsF- PDT films which tends to indicate a better crystallinity while the peaks' shift indicate a higher Ga incorporation. The highest crystallinity was reported for a 20nm RbF PDT film. Additionally, Na-PreDT Ga rich CIGS films show a much higher I(112)/I(220/204) XRD peak intensity ratio than the Na-free films, which again tends to indicate a synergy between Na and other heavy alkali elements.

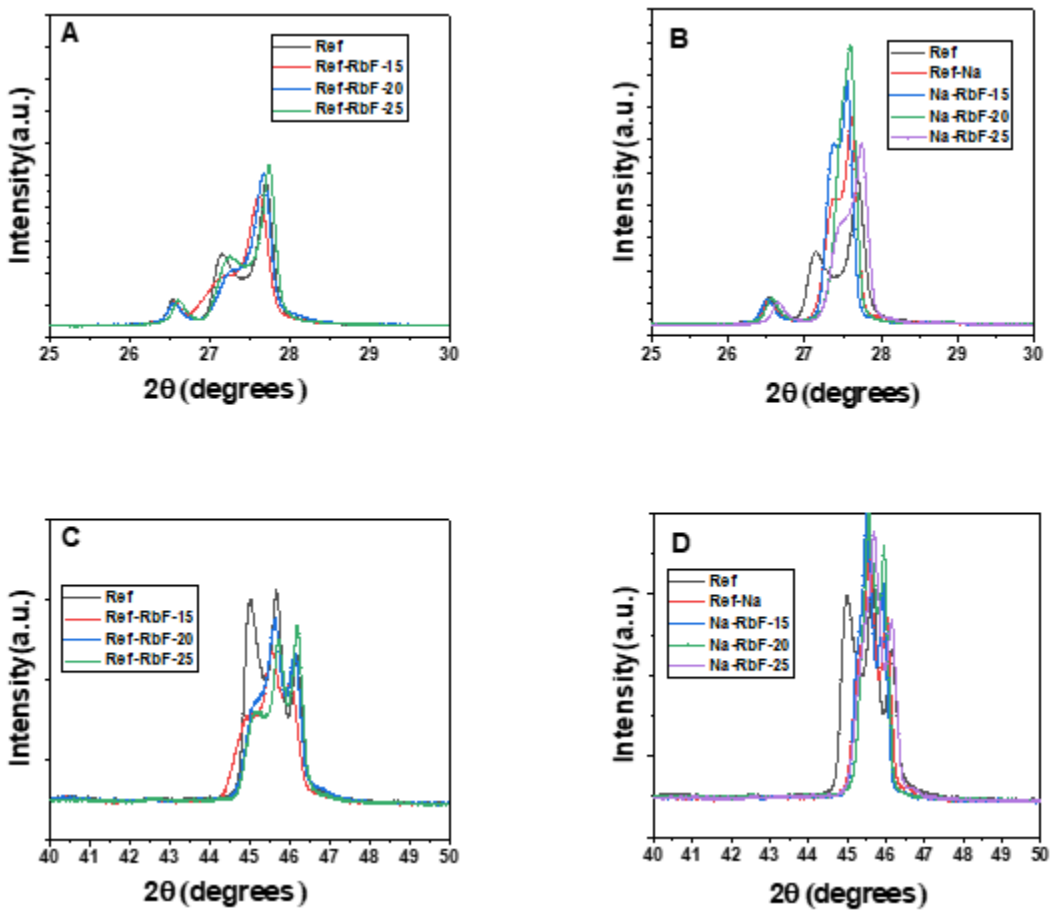

Figure 5.15: XRD diffraction pattern for (112) and (220)/(204) reflection peaks of CIGS films with RbF-PDT. (A) Na-free CIGS (112) peaks, (B) Na-doped CIGS (112) peaks, (C) Na-free CIGS (220)/(204) peaks, and (D) Na-doped CIGS (220)/(204) peaks.

Table 5.5: summarized peak position, peak intensity, rates and FWHM derived from XRD measurements of RbF-PDT Ga rich CIGS films with and without Na-PreDT.

film	**CIGS (112)**		**CIGS (220/204)**		**I(112)/I(220/204)**	**FWHM (112)**
	2θ[degrees]	I[counts]	2θ[degrees]	I[counts]		
Ref	27.51	48293	45.65	15546	3.10	0.81
Ref/15-RbF	27.49	43705	46.15	11511	3.79	0.67
Ref/20-RbF	27.57	50587	46	13641	3.70	0.55
Ref/25-RbF	27.57	53302	45.99	9623	5.53	0.72
Ref-Na	27.61	67038	45.57	17383	3.85	0.40
Ref-Na15-RbF	27.47	78446	46.16	13320	5.88	0.34

Ref-Na20-RbF	27.54	89375	45.92	15706	5.69	0.26
Ref-Na-25-RbF	27.64	59210	45.68	18898	3.13	0.45

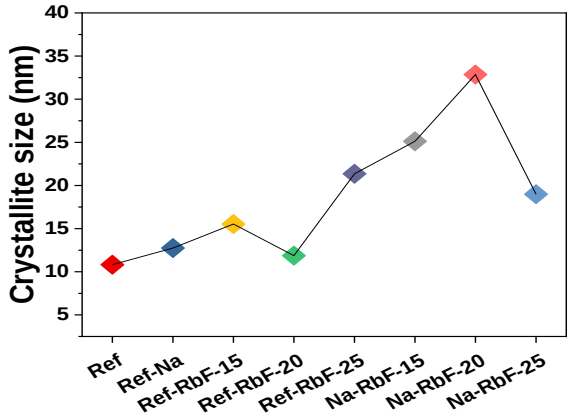

Figure 5.16: Effect of RbF-PDT on the crystallite size of Ga rich CIGS.

Effects of RbF-PDT on the performance of the devices

Figure 5.17 shows the statistical distribution of the PV performance and the parameters of GR-CIGS solar cells fabricated by using RbF-PDT. For the Na doped samples, the addition of RbF PDT does not significantly improve the conversion efficiency. Compared with undoped sample (Ref), the sample Ref-RbF- 25 shows very slightly better PV performance except for a reduced FF, which was related to an increased series resistance and reduced shunt resistance. In this specific case, the XRD observation do not positively correlate with photovoltaic performance. Additionally, there does not seem to be a beneficial synergy between Na and Rb regarding the PV parameters, with performance remaining similar or even slightly lower than the reference. In spite of the remarkable performance improvement of CIGS by Rb-PDT [173].

Table 5.6: Comparison summary of the main photovoltaic parameters of the best cell of each sample.

Device	**Jsc (mA/cm2)**	**Voc (mV)**	**FF (%)**	**η (%)**	**Rp ($\Omega.cm^2$)**	**Rs ($\Omega.cm^2$)**

Ref	**24,69**	**604**	**64,38**	**9,60**	**1010**	**1,89**
Ref -Rb-15	25.22	553	56 ,99	7.95	439	3.1
Ref -Rb-20	23.53	664	58.46	9.13	803	4.56
Ref -Rb-25	24.83	645	61.32	9.82	883	3.95
Ref-Na	25.05	623	62.66	9.78	1054	2.38
Na -Rb-15	22.85	601	51.58	7.08	436	3.88
Na -Rb-20	26.34	630	57.01	9.47	486	3.48
Na -Rb-25	23.27	605	52.36	7.38	283	3.11

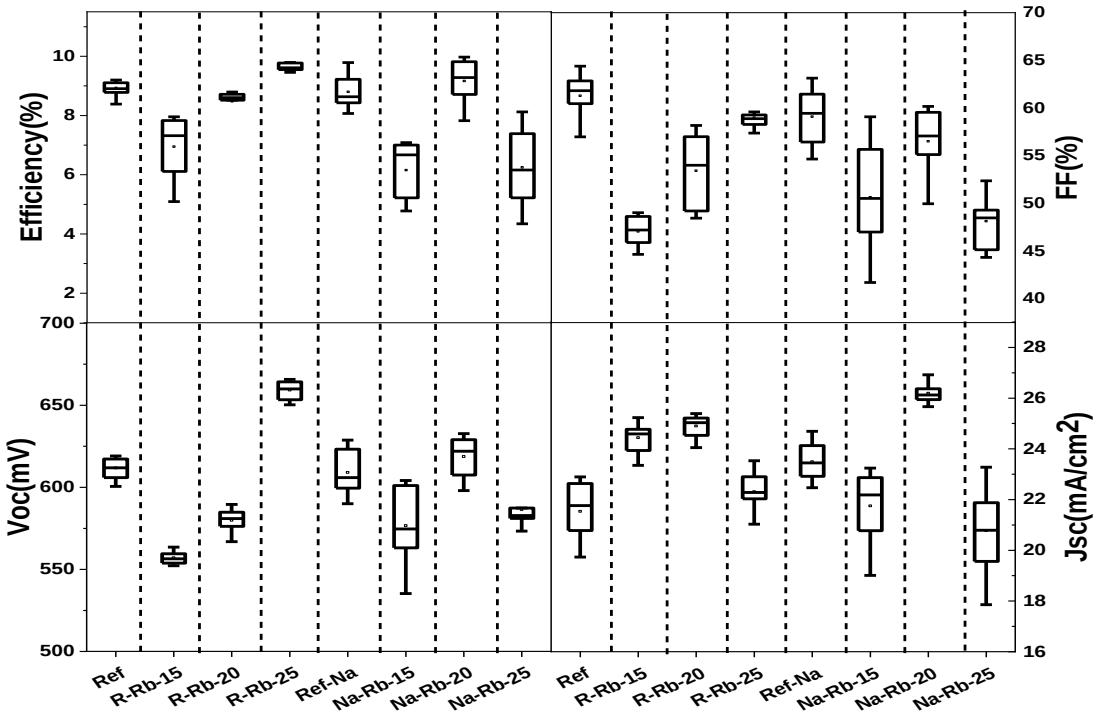

Figure 5.17: Boxchart of the main solar cell parameters of each sample.

Figure 5.18 (a) and (b) shows the J-V and the EQE curves of the best cells of the series. While the Jsc are maintained at a similar range, except for Na-Rb-15 showing a lower Jsc and Na-Rb-20a higher Jsc. This observation is confirmed by the EQE. The Voc improvement in the Na-doped cells could be due to reduce the interface recombination [174].

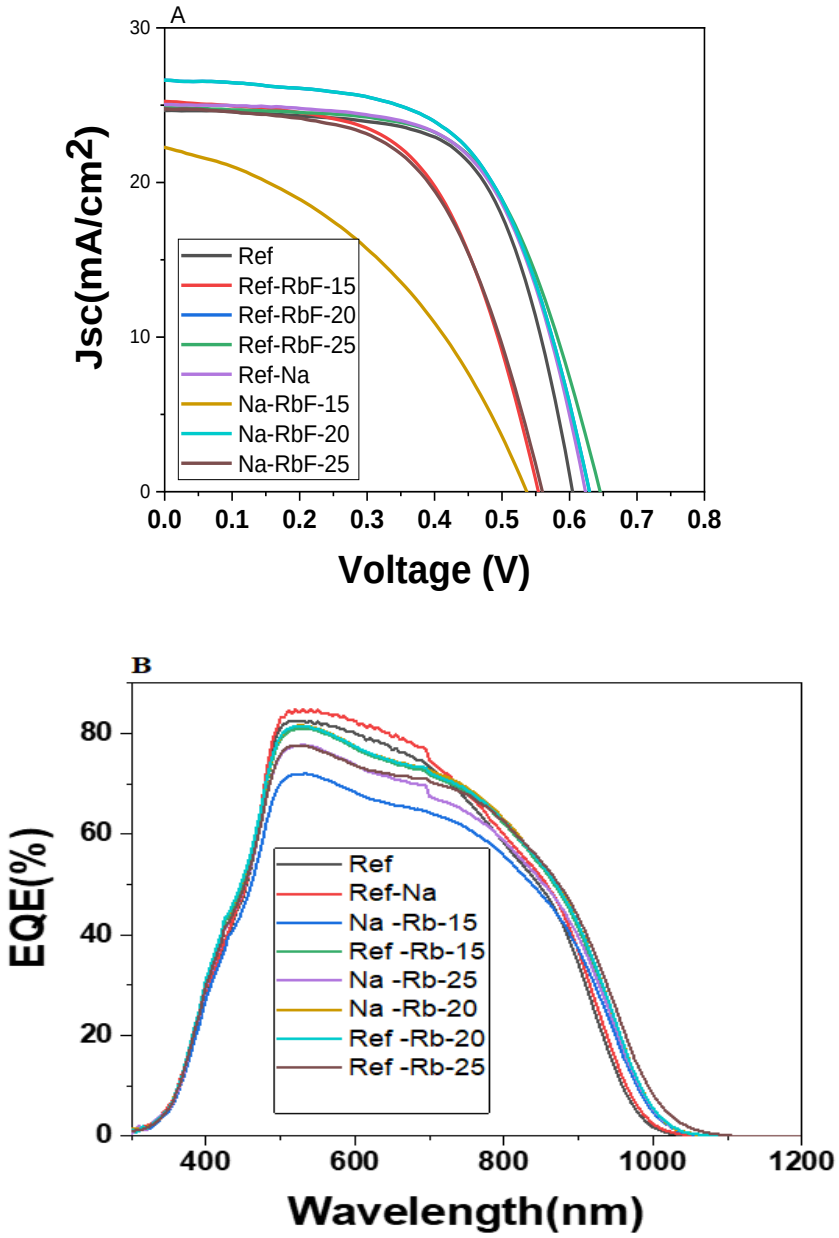

Figure 5.18: (A) J-V and (B) EQE curves of the best cell of each sample.

We assume that the increase in Voc for CIGS devices combining RbF-PDT and Na PreDT due to the diffusion of Ga to the surface of the CIGS as compared to the reference device (Table 5 and figure A and B).

The best solar cell efficiency was achieved by a 25nm of RbF -PDT without Na-PreDT

It is observed that the Cs- device has the highest η (11 %), Voc (616 mV) and FF (60.30 %) values while Jsc is highest for the KF device and yields the second best η value

5.4 Summary

Important results have been obtained for Ga rich CIGS thin film solar cells on FTO transparent back contact, which can be used as a top cell in tandem configuration, by appealing Na incorporation by pre-deposition treatment, Rb and Cs post deposition treatment strategies. A clear improvement in the crystallinity, electrical parameters have reported, the record cell has been obtained by CsF post deposition treatment on Na doped Ga rich CIGS with 70% of gallium. Figure 5.19 shows the data of the best cell obtained in this these work.

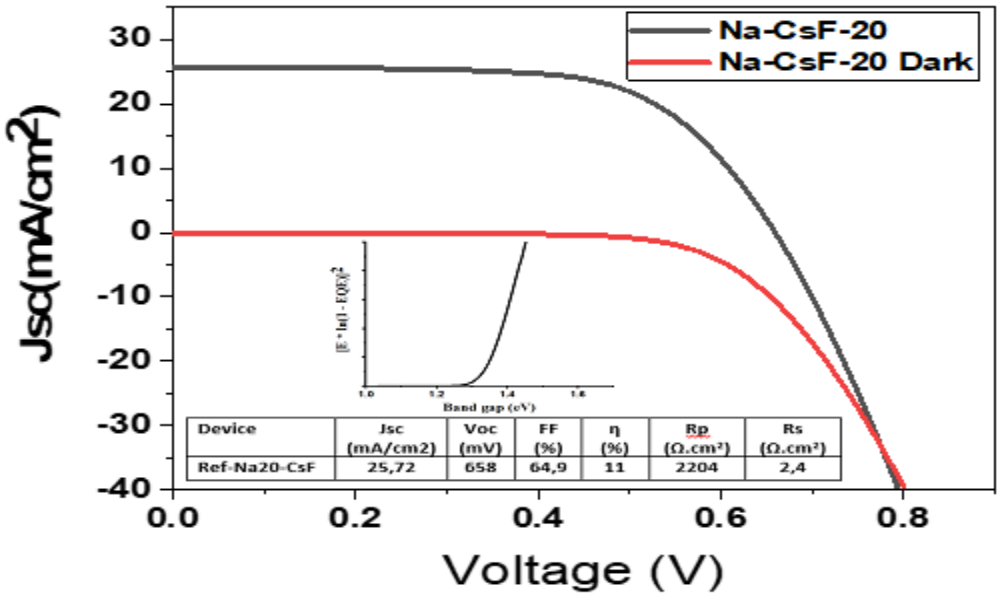

Figure 5.19: Electrical and optical parameters of the record cell.

6 Conclusions

The overarching purpose objective of this PhD thesis was to fabricate wide bandgap CIGS absorbers onto transparent substrate, while retaining performances close devices fabricated on standard Mo substrate. The results of this thesis have direct implication for emerging photovoltaic concepts such a BIPV, while bringing new opportunities for very high efficiency concepts such as tandem solar cells using CIGS absorbers. The main result of this work was the fabrication of wide bandgap CIGS-based solar cells on transparent substrate with a photovoltaic conversion efficiency up to 11%.

To achieve this goal, the first part of this PhD thesis has been devoted exclusively to the optimization of the CIGS growth processes, resulting in a baseline process with much improved efficiencies for high Ga content solar devices. A thorough study of the structural and chemical properties ascribed to performance limitations was carried out. In a first step, the structural and electrical properties of wide bandgap CIGS films (Eg>1.4 eV) have been examined by changing the CIG and GIG ratios in absorbers fabricated on FTO substrates. It was found that Cu-poor absorber composition (CGI ≈ 0.7) had the best conversion efficiency, open-circuit voltage, fill factor, and efficiency. The degradation of electrical parameters for high Cu contents has been attributed to an increased recombination rates and the formation of secondary $Cu_{2-x}Se$ phases. On the other hand, increasing the gallium content unexpectedly did not lead to a proportional improvement of the open circuit voltage, while simultaneously negatively affecting the current density.

In a second step, the effect of temperature employed during the absorber synthesis has been studied, with variations ranging from 500, 550, 575 to 600 °C. It was found that higher temperatures lead to a better homogenization of In/Ga in a single phase and an increased crystal quality. Despite the film annealed at 600 °C showing a better homogenization, the highest conversion efficiency was obtained with the film annealed at 550°C, and it was concluded that the annealing temperatures should be no less than 550 °C.

One detrimental factor degrading the efficiency of wideband gap CIGS is a possibly unfavorable band alignment at the p-n junction. Therefore, CdS was replaced by several

alternative buffer layers. However, no clear difference was observed in the resulting devices, despite an EQE enhancement when using In_2S_3 buffer at short wavelength photons.

Using methods widely reported to improve the efficiency of standard CIGS devices and applying those to wide bandgap absorbers was one of the main objectives of this thesis. As such, the influence of alkali elements doping such Na, Cs and Rb was a key step of this work. Using an innovative sodium pre-deposition method, Na PreDT, it was possible to finely tune the presence of Na within the CIGS matrix. From Raman and XRD results, we found that Na-treatment leads to an increased Ga incorporation and a strong (112) orientation of the Ga rich CIGS film. The analysis of illuminated J-V curve demonstrated that Na PreDT permits to markedly improve the devices' conversion efficiency. Post deposition treatments using PDT alkali-halides such as RbF, or CsF have been also considered, leading to a clear improvement in crystalline quality and efficiency of the devices when combining Na-PreDT and CsF-PDT, specifically due to the enhancement of the V_{oc}, FF and Rsh.

Finally, an efficiency of 11% for a wide bandgap CIGS absorber grown on FTO-coated glass was obtained thanks to the combined action of Na Pre-DT and Cs-PDT.

7 References

[1] C. Pasten and J. C. Santamarina, “Energy and quality of life,” *Energy Policy*, vol. 49, pp. 468–476, 2012, doi: 10.1016/j.enpol.2012.06.051.

[2] S. Pelin and Ö. Sezin, “The Role and Importance of Energy Ef fi ciency for Sustainable Development of the Countries,” vol. 1, no. Isbs 2017, 2018.

[3] F. Farirai, M. Ozonoh, T. C. Aniokete, O. Eterigho-ikelegbe, M. Mupa, and B. Zeyi, “Methods of extracting silica and silicon from agricultural waste ashes and

application of the produced silicon in solar cells : a mini-review," *Int. J. Sustain. Eng.*, vol. 00, no. 00, pp. 1–22, 2020, doi: 10.1080/19397038.2020.1720854.

[4] GEA, "Global Energy Assessment-Renewable Energy," pp. 761–900, 2012, [Online]. Available: http://www.iiasa.ac.at/web/home/research/Flagship-Projects/Global-Energy-Assessment/Home-GEA.en.html.

[5] H. A. Ajimotokan and W. O. Raji, "GLOBAL WARMING AND ENVIRONMENTAL CHANGE PROBLEMS : RENEWABLE ENERGY AND CLEANER FOSSIL FUELS," no. January, 2010.

[6] X. Tang, "Depletion of fossil fuels and anthropogenic climate change — A review," vol. 52, pp. 797–809, 2013, doi: 10.1016/j.enpol.2012.10.046.

[7] P. Gonçalves *et al.*, "Photovoltaic technologies : Mapping from patent analysis," *Renew. Sustain. Energy Rev.*, vol. 93, no. April, pp. 215–224, 2018, doi: 10.1016/j.rser.2018.05.033.

[8] L. Pe, "A review on buildings energy consumption information ´," vol. 40, pp. 394–398, 2008, doi: 10.1016/j.enbuild.2007.03.007.

[9] E. H. I and J. R. Benemann, "e r g a m o n," pp. 467–473, 1997.

[10] L. Chiari and A. Zecca, "Constraints of fossil fuels depletion on global warming projections," *Energy Policy*, vol. 39, no. 9, pp. 5026–5034, 2011, doi: 10.1016/j.enpol.2011.06.011.

[11] A. Holt and I. J. Pengelly, "ITS and renewable energy," *15th World Congr. Intell. Transp. Syst. ITS Am. Annu. Meet. 2008*, vol. 6, pp. 3854–3862, 2008, doi: 10.1049/ic.2008.0789.

[12] C. A. Tracker, "Global Update - Glasgow's 2030 credibility gap - Nov 2021," no. November, 2021.

[13] M. Aguirre and G. Ibikunle, "Determinants of renewable energy growth: A global sample analysis," *Energy Policy*, vol. 69, pp. 374–384, 2014, doi: 10.1016/j.enpol.2014.02.036.

[14] J. M. Martı, "Analytical model for solar PV and CSP electricity costs : Present LCOE values and their future evolution," vol. 20, pp. 119–132, 2013, doi: 10.1016/j.rser.2012.11.082.

[15] C. Kost, S. Shammugam, V. Jülch, H. Nguyen, and T. Schlegl, "Levelized Cost of Electricity- Renewable Energy Technologies," no. March, 2018.

[16] U. S. E. I. Administration, "Levelized Cost and Levelized Avoided Cost of New Generation Resources in the Annual Energy Outlook 2020," no. February, pp. 1–22, 2020.

[17] Lepetit Thomas, “Influence of KF post deposition treatment on the polycrystalline Cu(In,Ga)Se2/CdS hetero-junction formation for photovoltaic application,” *PhD Thesis - Univ. Nantes*, no. November 2015, 2015, doi: 10.13140/RG.2.1.3451.6242.

[18] T. Dullweber, G. Hanna, U. Rau, and H. W. Schock, “New approach to high-efficiency solar cells by band gap grading in Cu(In,Ga)Se2 chalcopyrite semiconductors,” *Sol. Energy Mater. Sol. Cells*, vol. 67, no. 1–4, pp. 145–150, 2001, doi: 10.1016/S0927-0248(00)00274-9.

[19] A. Kumar, P. Baredar, and U. Qureshi, “Historical and recent development of photovoltaic thermal (PVT) technologies,” vol. 42, pp. 1428–1436, 2015.

[20] I. Hajdukovic, “The Impact of International Trade on the Price of Solar Photovoltaic Modules : Empirical Evidence To cite this version : HAL Id : hal-02488067 The Impact of International Trade on the Price of Solar Photovoltaic Modules : Empirical Evidence *,” 2020.

[21] M. H. Shubbak, “Advances in solar photovoltaics: Technology review and patent trends,” *Renew. Sustain. Energy Rev.*, vol. 115, no. September, p. 109383, 2019, doi: 10.1016/j.rser.2019.109383.

[22] B. Parida, S. Iniyan, and R. Goic, “A review of solar photovoltaic technologies,” *Renew. Sustain. Energy Rev.*, vol. 15, no. 3, pp. 1625–1636, 2011, doi: 10.1016/j.rser.2010.11.032.

[23] I. W. Paper, “Materials availability for thin film (TF) PV technologies development : a real concern ?,” no. February, pp. 1–26, 2011.

[24] G. M. Wilson *et al.*, “The 2020 photovoltaic technologies roadmap,” 2020.

[25] R. E. N. Members, *Renewables 2020 global status report 2020*. 2020.

[26] O. K. Simya, P. Radhakrishnan, A. Ashok, K. Kavitha, and R. Althaf, “Engineered nanomaterials for energy applications,” *Handb. Nanomater. Ind. Appl.*, pp. 751–767, 2018, doi: 10.1016/B978-0-12-813351-4.00043-2.

[27] J. Ramanujam *et al.*, “Flexible CIGS, CdTe and a-Si:H based thin film solar cells: A review,” *Prog. Mater. Sci.*, vol. 110, p. 100619, 2020, doi: 10.1016/j.pmatsci.2019.100619.

[28] J. Chen *et al.*, “A Polymer / Carbon-Nanotube Ink as a Boron-Dopant / Inorganic-Passivation Free Carrier Selective Contact for Silicon Solar Cells with over 21 % Efficiency,” vol. 2004476, pp. 1–8, 2020, doi: 10.1002/adfm.202004476.

[29] A. Luceño-s and A. Mar, “Materials for Photovoltaics : State of Art and Recent Developments,” 2019, doi: 10.3390/ijms20040976.

[30] F. Ise, “Photovoltaics Report,” no. September, 2020.

[31] S. Chowdhury, M. Kumar, S. Dutta, and J. Park, “High-efficiency Crystalline Silicon Solar Cells : A Review High-efficiency Crystalline Silicon Solar Cells : A Review,” no. May 2020, 2019, doi: 10.7849/ksnre.2019.3.15.3.036.

[32] S. Chowdhury, K. Sajedur, and T. Chowdhury, “An overview of solar photovoltaic panels ’ end-of-life material recycling,” *Energy Strateg. Rev.*, vol. 27, p. 100431, 2020, doi: 10.1016/j.esr.2019.100431.

[33] A. Benmir and M. S. Aida, “Analytical modeling and simulation of CIGS solar cells,” *Energy Procedia*, vol. 36, pp. 618–627, 2013, doi: 10.1016/j.egypro.2013.07.071.

[34] T. B. Kamiya Monemar H Venghaus Y Yamamoto *et al.*, *SPRINGER SERIES IN PHOTONICS Advanced Optoelectronic Devices 8 Nonlinear Photonics Integrated Silicon Optoelectronics 9 Optical Solitons in Fibers 3 Third Edition Waveguide Nonlinear-Optic Devices from Semiconductor Lasers*. .

[35] S. Issue, “Thin-Film Solar Cells: An Overview,” vol. 92, no. December 2003, pp. 69–92, 2004, doi: 10.1002/pip.541.

[36] T. D. Lee and A. U. Ebong, “A review of thin fi lm solar cell technologies and challenges,” *Renew. Sustain. Energy Rev.*, no. September 2015, pp. 0–1, 2016, doi: 10.1016/j.rser.2016.12.028.

[37] V. Muteri *et al.*, “Review on Life Cycle Assessment of Solar Photovoltaic Panels,” 2020.

[38] H. Werner, “Second and Third Generation Photovoltaics –,” vol. 67, pp. 51–67, 2004.

[39] G. F. Brown and J. Wu, “Third generation photovoltaics,” *Laser Photonics Rev.*, vol. 3, no. 4, pp. 394–405, 2009, doi: 10.1002/lpor.200810039.

[40] R. Chandran, S. K. Panda, and A. Mallik, “A short review on the advancements in electroplating of - CuInGaSe 2 thin films,” *Mater. Renew. Sustain. Energy*, 2018, doi: 10.1007/s40243-018-0112-1.

[41] T. Feurer *et al.*, “Progress in thin fi lm CIGS photovoltaics – Research and development , manufacturing , and applications,” 2016, doi: 10.1002/pip.

[42] M. Nakamura, K. Yamaguchi, Y. Kimoto, Y. Yasaki, T. Kato, and H. Sugimoto, “Cd-Free Cu(In,Ga)(Se,S)2 thin-film solar cell with record efficiency of 23.35%,” *IEEE J. Photovoltaics*, vol. 9, no. 6, pp. 1863–1867, 2019, doi: 10.1109/JPHOTOV.2019.2937218.

[43] D. Delmonte *et al.*, “Metastable (CuAu-type) CuInS 2 Phase: High-Pressure Synthesis and Structure Determination,” pp. 0–5, 2020, doi: 10.1021/acs.inorgchem.0c01531.

[44] J. Liu, D. Zhuang, H. Luan, M. Cao, M. Xie, and X. Li, “Preparation of Cu(In,Ga)Se2thin film by sputtering from Cu(In,Ga)Se2quaternary target,” *Prog. Nat. Sci. Mater. Int.*,

vol. 23, no. 2, pp. 133–138, 2013, doi: 10.1016/j.pnsc.2013.02.006.

[45] T. Yamaguchi, K. Tsujita, S. Niiyama, and T. Imanishi, “Preparation of High Ga Content Cu(In,Ga)Se₂ Thin Films by Sequential Evaporation Process Added In₂S₃,” *Adv. Mater. Phys. Chem.*, vol. 02, no. 04, pp. 106–109, 2012, doi: 10.4236/ampc.2012.24b029.

[46] T. Higuchi, N. Usami, and T. Minemoto, “Effect of Ga content and growth temperature on Cu(In,Ga)Se2 thin film deposited on heat-resistant glass substrates,” *Phys. Status Solidi Curr. Top. Solid State Phys.*, vol. 10, no. 7–8, pp. 1035–1037, 2013, doi: 10.1002/pssc.201200833.

[47] S. H. Moon *et al.*, “Printable, wide band-gap chalcopyrite thin films for power generating window applications,” *Sci. Rep.*, vol. 4, no. August, 2014, doi: 10.1038/srep04408.

[48] Z. Cevher, “Optimization of CuInxGa1-xSe2 Solar Cells with Post Selenization,” 2018.

[49] M. Raghuwanshi, “Influence of Grain Boundary Chemistry on the properties of CIGS photovoltaic cells Mohit Raghuwanshi,” *Thesis*, 2016, [Online]. Available: https://tel.archives-ouvertes.fr/tel-01252605.

[50] J. Keller, W. C. Chen, L. Riekehr, T. Kubart, T. Törndahl, and M. Edoff, “Bifacial Cu(In,Ga)Se2 solar cells using hydrogen-doped In2O3 films as a transparent back contact,” *Prog. Photovoltaics Res. Appl.*, vol. 26, no. 10, pp. 846–858, 2018, doi: 10.1002/pip.3025.

[51] T. Nakada, “Microstructural and diffusion properties of CIGS thin film solar cells fabricated using transparent conducting oxide back contacts,” vol. 481, pp. 419–425, 2005, doi: 10.1016/j.tsf.2004.11.142.

[52] T. Nakada, Y. Hirabayashi, T. Tokado, D. Ohmori, and T. Mise, “Novel device structure for Cu (In , Ga) Se 2 thin film solar cells using transparent conducting oxide back and front contacts,” vol. 77, pp. 739–747, 2004, doi: 10.1016/j.solener.2004.08.010.

[53] Z. Y. Banyamin, P. J. Kelly, G. West, and J. Boardman, “Electrical and Optical Properties of Fluorine Doped Tin Oxide Thin Films Prepared by Magnetron Sputtering,” pp. 732–746, 2014, doi: 10.3390/coatings4040732.

[54] Z. Y. Banyamin, P. J. Kelly, G. West, and J. Boardman, “Electrical and optical properties of fluorine doped tin oxide thin films prepared by magnetron sputtering,” *Coatings*, vol. 4, no. 4, pp. 732–746, 2014, doi: 10.3390/coatings4040732.

[55] T. Nakada, “Microstructural and diffusion properties of CIGS thin film solar cells fabricated using transparent conducting oxide back contacts,” *Thin Solid Films*, vol. 480–481, pp. 419–425, 2005, doi: 10.1016/j.tsf.2004.11.142.

[56] D. Kim *et al.*, “Flexible and Semi-Transparent Ultra-Thin CIGSe Solar Cells Prepared

on Ultra-Thin Glass Substrate: A Key to Flexible Bifacial Photovoltaic Applications," *Adv. Funct. Mater.*, vol. 30, no. 36, pp. 1–14, 2020, doi: 10.1002/adfm.202001775.

[57] D. Rudmann, G. Bilger, H. Zogg, and A. N. Tiwari, "Comparison of structural and electrical properties of Cu (In, Ga) Se 2 for substrate and superstrate solar cells," vol. 404, pp. 293–296, 2002.

[58] F. Mollica *et al.*, "Light absorption enhancement in ultra-thin Cu(In,Ga)Se2 solar cells by substituting the back-contact with a transparent conducting oxide based reflector," *Thin Solid Films*, vol. 633, pp. 202–207, 2017, doi: 10.1016/j.tsf.2016.10.006.

[59] S.-H. Wei, S. Zhang, and A. Zunger, "Band Structure and Stability of Ternary Semiconductor Polytypes," *Jpn. J. Appl. Phys.*, vol. 39, no. S1, p. 237, 2000, doi: 10.7567/jjaps.39s1.237.

[60] J. H. Cha, S. J. Noh, and D. Y. Jung, "Synthesis and Nanostructures of Metal Selenide Precursors for Cu(In,Ga)Se<inf>2</inf> Thin-Film Solar Cells," *ChemSusChem*, vol. 8, no. 14, pp. 2407–2413, 2015, doi: 10.1002/cssc.201403464.

[61] T. Nishimura, S. Kasashima, Y. Hirai, Y. Kurokawa, and A. Yamada, "Fabrication of Cu(In,Ga)Se $_2$ solar cells with a single graded band profile," *Phys. Status Solidi*, vol. 252, no. 6, pp. 1235–1238, 2015, doi: 10.1002/pssb.201400305.

[62] Y. Shih, Y. Tsai, and D. Lin, "Synthesis and Characterization of CuIn 1 − x Ga x Se 2 Semiconductor Nanocrystals," pp. 1–12, 2020.

[63] K. Chang, Y. Zhang, J. Zhang, T. Li, J. Wang, and W. Qin, "Effect of temperature-induced phase transitions on bioleaching of chalcopyrite," *Trans. Nonferrous Met. Soc. China*, vol. 29, no. 10, pp. 2183–2191, 2019, doi: 10.1016/S1003-6326(19)65124-1.

[64] G. R. A. Ashok, P. Chawla, P. Semalti, S. Velumani, S. N. Sharma, and H. Castaneda, "Perspectives of chalcopyrite - based CIGSe thin - film solar cell : a review," *J. Mater. Sci. Mater. Electron.*, vol. 31, no. 10, pp. 7286–7314, 2020, doi: 10.1007/s10854-020-03338-2.

[65] J. Y. Srour, J. Youssef, and S. Electronic, "Electronic structure and competition of phases in Cu- (In , Ga) -Se , Ga-Se and In-Se semiconductors : first-principles calculations based on different exchange-correlation potentials To cite this version : HAL Id : tel-01531300 soutenance et mis à disp," 2017.

[66] G. Regmi *et al.*, "Perspectives of chalcopyrite-based CIGSe thin-film solar cell: a review," *J. Mater. Sci. Mater. Electron.*, vol. 31, no. 10, pp. 7286–7314, 2020, doi: 10.1007/s10854-020-03338-2.

[67] F. Annoni, "Progress in photovoltaic cells based on Low-Temperature Pulsed-

Electron- Deposited Cu (In , Ga) Se2 films UNIVERSITA ' DEGLI STUDI DI PARMA Dottorato di ricerca in Scienza e Tecnologia dei Materiali Ciclo XXIX Progress in photovoltaic cells based on Low," no. July, 2018, doi: 10.13140/RG.2.2.15023.23208.

[68] E. R. Baek, V. Astini, A. Tirta, and B. Kim, "Phase evolution of CIGS alloyed compound synthesis by direct melting method," *Curr. Appl. Phys.*, vol. 11, no. 1, pp. S76–S80, 2011, doi: 10.1016/j.cap.2010.11.091.

[69] E. C. D. O. N, "Local inhomogeneities in polycrystalline wide band gap," 2019.

[70] A. Thomere *et al.*, "Chemical crystallographic investigation on Cu2S-In2S3-Ga2S3 ternary system," *Thin Solid Films*, vol. 665, pp. 46–50, 2018, doi: 10.1016/j.tsf.2018.09.003.

[71] T. Unold and C. A. Kaufmann, *Chalcopyrite thin-film materials and solar cells*, vol. 1. Elsevier Ltd., 2012.

[72] H. Fujiwara and R. W. Collins, *Spectroscopic Ellipsometry for Photovoltaics Volume 2: Applications and Optical Data of Solar Cell Materials*, vol. 214. 2018.

[73] Y.-C. Wang and H.-P. D. Shieh, "Double-graded bandgap in Cu(In,Ga)Se $_2$ thin film solar cells by low toxicity selenization process," *Appl. Phys. Lett.*, vol. 105, no. 7, p. 073901, 2014, doi: 10.1063/1.4893713.

[74] M. Nardone *et al.*, "Baseline Models for Three Types of CIGS Cells: Effects of Buffer Layer and Na Content," *2018 IEEE 7th World Conf. Photovolt. Energy Conversion, WCPEC 2018 - A Jt. Conf. 45th IEEE PVSC, 28th PVSEC 34th EU PVSEC*, pp. 3013–3018, 2018, doi: 10.1109/PVSC.2018.8548167.

[75] K. Decock, J. Lauwaert, and M. Burgelman, "Characterization of graded CIGS solar cells," *Energy Procedia*, vol. 2, no. 1, pp. 49–54, 2010, doi: 10.1016/j.egypro.2010.07.009.

[76] J. Bi *et al.*, "Influence of Cu on Ga diffusion during post-selenizing the electrodeposited Cu/In/Ga metallic precursor process," *Sol. Energy Mater. Sol. Cells*, vol. 182, no. February, pp. 92–97, 2018, doi: 10.1016/j.solmat.2018.03.007.

[77] M. D. Heinemann, "CIGSe Superstrate Solar Cells : Growth and Characterization of CIGSe Thin Films on Transparent Conductive Oxides," *PhD Thesis*.

[78] C. Spindler *et al.*, "Electronic defects in Cu (In , Ga) Se 2 : Towards a comprehensive model," no. September, 2019, doi: 10.1103/PhysRevMaterials.3.090302.

[79] S. Siebentritt, "Chalcopyrite compound semiconductors for thin film solar cells," *Curr. Opin. Green Sustain. Chem.*, vol. 4, pp. 1–7, 2017, doi: 10.1016/j.cogsc.2017.02.001.

[80] J. Pohl and K. Albe, "Intrinsic point defects in CuInSe 2 and CuGaSe 2 as seen via screened-exchange hybrid," vol. 245203, pp. 1–16, 2013, doi:

10.1103/PhysRevB.87.245203.

[81] S. Siebentritt, M. Igalson, C. Persson, and S. Lany, “The electronic structure of chalcopyrites — bands , point defects and grain boundaries,” no. April, pp. 390–410, 2010, doi: 10.1002/pip.936.

[82] H. H. Sheu, Y. T. Hsu, S. Y. Jian, and S. C. Liang, “The effect of Cu concentration in the photovoltaic efficiency of CIGS solar cells prepared by co-evaporation technique,” *Vacuum*, vol. 131, pp. 278–284, 2016, doi: 10.1016/j.vacuum.2016.07.008.

[83] A. Darga *et al.*, “Study of the electronic properties of wide band gap CIGSe solar cells: Influence of copper off-stoichiometry,” *J. Non. Cryst. Solids*, vol. 358, no. 17, pp. 2428–2430, 2012, doi: 10.1016/j.jnoncrysol.2012.01.020.

[84] B. Ümsür, “Surface Engineering of Cu(In,Ga)Se 2 by KF and CdS – a Study by High-Energy Photoemission Spectroscopy,” 2017.

[85] J. Ramanujam and U. P. Singh, “Copper indium gallium selenide based solar cells – a review,” *Energy Environ. Sci.*, vol. 10, no. 6, pp. 1306–1319, 2017, doi: 10.1039/C7EE00826K.

[86] T. Film and D. Parameters, “16. VACUUM DEPOSITION TECHNIQUES* 16.1. Introduction,” vol. C, 1979.

[87] J. Ramanujam and U. P. Singh, “Copper indium gallium selenide based solar cells - A review,” *Energy Environ. Sci.*, vol. 10, no. 6, pp. 1306–1319, 2017, doi: 10.1039/c7ee00826k.

[88] P. Fan *et al.*, “Fabrication of Cu(In,Ga)Se2 thin films by ion beam sputtering deposition from a quaternary target at different substrate temperatures,” *J. Mater. Sci. Mater. Electron.*, vol. 23, no. 11, pp. 1957–1960, 2012, doi: 10.1007/s10854-012-0687-8.

[89] S. Niki *et al.*, “CIGS absorbers and processes,” *Prog. Photovoltaics Res. Appl.*, vol. 18, no. 6, pp. 453–466, 2010, doi: 10.1002/pip.969.

[90] C. H. Huang, W. J. Chuang, C. P. Lin, Y. L. Jan, and Y. C. Shih, “Deposition technologies of high-efficiency cigs solar cells: Development of two-step and co-evaporation processes,” *Crystals*, vol. 8, no. 7, 2018, doi: 10.3390/cryst8070296.

[91] M. Krause *et al.*, “Microscopic origins of performance losses in highly efficient Cu(In,Ga)Se2 thin-film solar cells,” *Nat. Commun.*, vol. 11, no. 1, 2020, doi: 10.1038/s41467-020-17507-8.

[92] I. Repins *et al.*, “No Title,” pp. 3–8, 2008.

[93] O. Salomon *et al.*, “Influence of molybdenum back contact on the pid effect for Cu(In,Ga)Se2 solar cells,” *Coatings*, vol. 9, no. 12, 2019, doi:

10.3390/coatings9120794.

[94] A. Chin, “Graduate Student Researcher Ac ce pte d M us pt,” vol. 2, 2019.

[95] L.-M.-U. M. Technische Universtität München, *済無No Title No Title*. 2018.

[96] R. Mohan and R. Paulose, “Brief Review on Copper Indium Gallium Diselenide (CIGS) Solar Cells,” *Photoenergy Thin Film Mater.*, pp. 157–192, 2019, doi: 10.1002/9781119580546.ch4.

[97] T. Dullweber *et al.*, “Study of the effect of gallium grading in Cu(In,Ga)Se2,” *Thin Solid Films*, vol. 361, pp. 478–481, 2000, doi: 10.1016/S0040-6090(99)00845-7.

[98] B. Kim and B. K. Min, “Strategies toward highly efficient CIGSe thin-film solar cells fabricated by sequential process,” *Sustain. Energy Fuels*, vol. 2, no. 8, pp. 1671–1685, 2018, doi: 10.1039/c8se00158h.

[99] M. Ould Salem *et al.*, “Over 10% Efficient Wide Bandgap CIGSe Solar Cells on Transparent Substrate with Na Predeposition Treatment,” *Sol. RRL*, no. October, 2020, doi: 10.1002/solr.202000284.

[100] Y. Cho *et al.*, “A novel two-stage hybrid processing technique towards industrial manufacturing of the Cu(In,Ga)(S,Se)2 solar cell with materially efficient fabrication,” *J. Mater. Chem. A*, vol. 7, no. 19, pp. 11651–11658, 2019, doi: 10.1039/c9ta02954k.

[101] I. Klugius *et al.*, “Growth mechanism of thermally processed Cu(In,Ga)S 2 precursors for printed Cu(In,Ga)(S,Se) 2 solar cells,” *Phys. Status Solidi - Rapid Res. Lett.*, vol. 6, no. 7, pp. 297–299, 2012, doi: 10.1002/pssr.201206191.

[102] P. Jackson, D. Hariskos, R. Wuerz, W. Wischmann, and M. Powalla, “Compositional investigation of potassium doped Cu (In , Ga) Se 2 solar cells with efficiencies up to 20 . 8 %,” vol. 222, no. 3, pp. 219–222, 2014, doi: 10.1002/pssr.201409040.

[103] P. Jackson *et al.*, “Properties of Cu(In,Ga)Se2solar cells with new record efficiencies up to 21.7%,” *Phys. Status Solidi - Rapid Res. Lett.*, vol. 9, no. 1, pp. 28–31, 2015, doi: 10.1002/pssr.201409520.

[104] P. Jackson, R. Wuerz, D. Hariskos, E. Lotter, W. Witte, and M. Powalla, “Effects of heavy alkali elements in Cu(In,Ga)Se2 solar cells with efficiencies up to 22.6%,” *Phys. Status Solidi - Rapid Res. Lett.*, vol. 10, no. 8, pp. 583–586, 2016, doi: 10.1002/pssr.201600199.

[105] C. C. In *et al.*, “Record Efficiency for Thin-Film Polycrystalline Solar Cells Up to 22 . 9 % Achieved by,” *IEEE J. Photovoltaics*, vol. PP, pp. 1–6, 2018, doi: 10.1109/JPHOTOV.2018.2882206.

[106] N. E. Gorji, U. Reggiani, and L. Sandrolini, “Graded band gap CIGS solar cells considering the valence band widening,” *Conf. Rec. IEEE Photovolt. Spec. Conf.*, pp.

906–908, 2012, doi: 10.1109/PVSC.2012.6317749.

[107] F. Larsson, N. S. Nilsson, J. Keller, M. Edoff, and T. Törndahl, “Record 1 . 0 V open - circuit voltage in wide band gap chalcopyrite solar cells,” no. April, pp. 755–763, 2017, doi: 10.1002/pip.2914.

[108] B. Telephone, L. Murray, and H. New, “CulnSe 2 /CdS heterojunction photoYoltaic detectors,” vol. 25, no. 8, pp. 434–435, 1974.

[109] S. O. Oyedele and B. Aka, “Numerical Simulation of Varied Buffer Layer of Solar Cells Based on Cigs,” *Model. Numer. Simul. Mater. Sci.*, vol. 07, no. 03, pp. 33–45, 2017, doi: 10.4236/mnsms.2017.73003.

[110] N. Severino, N. Bednar, and N. Adamovic, “Buffer layer optimization for high efficiency CIGS solar cells,” *J. Phys. Conf. Ser.*, vol. 758, no. 1, 2016, doi: 10.1088/1742-6596/758/1/012016.

[111] K. S. Gour, R. Parmar, R. Kumar, and V. N. Singh, “Cd-Free Zn(O,S) as Alternative Buffer Layer for Chalcogenide and Kesterite Based Thin Films Solar Cells: A Review,” *J. Nanosci. Nanotechnol.*, vol. 20, no. 6, pp. 3622–3635, 2019, doi: 10.1166/jnn.2020.17537.

[112] C. Bin Mo *et al.*, “Impact of Buffer Layer Process and Na on Shunt Paths of Monolithic Series-connected CIGSSe Thin Film Solar Cells,” *Sci. Rep.*, no. September 2018, pp. 1–11, 2019, doi: 10.1038/s41598-019-38945-5.

[113] C. Huang *et al.*, “Cu (In , Ga)(Se , S) 2 solar cell research in Solar Frontier : Progress and current status temperatures.”

[114] T. M. Friedlmeier *et al.*, “Improved Photocurrent in Cu (In , Ga) Se 2 Solar Cells :,” vol. 5, no. 5, pp. 1487–1491, 2015.

[115] T. Nakada and M. Mizutani, “18% efficiency Cd-free Cu(In, Ga)Se2 thin-film solar cells fabricated using chemical bath deposition (CBD)-ZnS buffer layers,” *Japanese J. Appl. Physics, Part 2 Lett.*, vol. 41, no. 2 B, pp. 165–167, 2002, doi: 10.1143/JJAP.41.L165.

[116] N. OKEREKE and A. EKPUNOBI, “ZnSe BUFFER LAYER DEPOSITION FOR SOLAR CELL APPLICATION.,” *J. Non-Oxide Glas. Vol*, vol. 3, no. 1, pp. 31–36, 2011.

[117] P. M. P. Salomé *et al.*, “Solar Energy Materials & Solar Cells CdS and Zn 1 À x Sn x O y buffer layers for CIGS solar cells,” *Sol. Energy Mater. Sol. Cells*, vol. 159, pp. 272–281, 2017, doi: 10.1016/j.solmat.2016.09.023.

[118] M. Nakamura, Y. Kouji, Y. Chiba, H. Hakuma, and T. Kobayashi, “Achievement of 19 . 7 % efficiency with a small-sized Cu (InGa)(SeS) 2 solar cells prepared by sulfurization after selenizaion process with Zn- based buffer,” pp. 849–852, 2013.

[119] U. Zimmermann and M. Edoff, “Cadmium-free CIGS mini-modules with ALD-grown

Zn (O , S) -based buffer layers," no. January, 2006.

[120] S. Kim, S. Mina, K. Kim, and J. Kim, "Sustainable Energy & Fuels solar cell as a bu ff er layer †," pp. 362–368, 2020, doi: 10.1039/c9se00778d.

[121] M. Powalla *et al.*, "CIGS cells and modules with high efficiency on glass and flexible substrates," *IEEE J. Photovoltaics*, vol. 4, no. 1, pp. 440–446, 2014, doi: 10.1109/JPHOTOV.2013.2280468.

[122] C. S. Lee, S. Kim, Y. M. Shin, B. G. Park, B. T. Ahn, and H. Kwon, "Performance improvement in Cd-free Cu(In,Ga)Se2 solar cells by modifying the electronic structure of the ZnMgO buffer layer," *RSC Adv.*, vol. 4, no. 69, pp. 36784–36790, 2014, doi: 10.1039/c4ra07776h.

[123] T. Minemoto *et al.*, "Theoretical analysis of the effect of conduction band offset of window/CIS layers on performance of CIS solar cells using device simulation," *Sol. Energy Mater. Sol. Cells*, vol. 67, no. 1–4, pp. 83–88, 2001, doi: 10.1016/S0927-0248(00)00266-X.

[124] C. Ga, S. Bechlaghem, B. Zebentout, and Z. Benamara, "Results in Physics The major in fl uence of the conduction-band-o ff set on Zn (O , S)/," vol. 10, no. July, pp. 650–654, 2018, doi: 10.1016/j.rinp.2018.07.006.

[125] S. H. Sohn *et al.*, "Band gap grading and photovoltaic performance of solution-processed Cu(In, Ga)S2 thin-film solar cells," *Phys. Chem. Chem. Phys.*, vol. 16, no. 48, pp. 27112–27118, 2014, doi: 10.1039/c4cp03243h.

[126] K. Decock, J. Lauwaert, and M. Burgelman, "Energy Procedia Characterization of graded CIGS solar cells," *Energy Procedia*, vol. 2, no. 1, pp. 49–54, 2010, doi: 10.1016/j.egypro.2010.07.009.

[127] Z. Jehl Li Kao, T. Kobayashi, and T. Nakada, "Modeling of the surface sulfurization of CIGSe-based solar cells," *Sol. Energy*, vol. 110, pp. 50–55, 2014, doi: 10.1016/j.solener.2014.08.004.

[128] S. Ouedraogo, R. Sam, F. Ouedraogo, M. B. Kebre, J. M. Ndjaka, and F. Zougmore, "Optimization of Copper Indium Gallium Di-Selenide (CIGS) based solar cells by back grading," *J. Ovonic Res.*, vol. 9, no. 4, pp. 95–103, 2013, doi: 10.1109/AFRCON.2013.6757813.

[129] M. Gloeckler and J. R. Sites, "Band-gap grading in Cu(In,Ga)Se2 solar cells," *J. Phys. Chem. Solids*, vol. 66, no. 11, pp. 1891–1894, 2005, doi: 10.1016/j.jpcs.2005.09.087.

[130] O. Lundberg, M. Edoff, and L. Stolt, "The effect of Ga-grading in CIGS thin film solar cells," *Thin Solid Films*, vol. 480–481, pp. 520–525, 2005, doi: 10.1016/j.tsf.2004.11.080.

[131] M. Saadat, M. Moradi, and M. Zahedifar, "CIGS absorber layer with double grading

Ga profile for highly efficient solar cells," *Superlattices Microstruct.*, vol. 92, pp. 303–307, 2016, doi: 10.1016/j.spmi.2016.02.036.

[132] J. wei Zhang, Y. ming Xue, W. Li, Y. min Zhao, and Z. xiang Qiao, "Morphology of CIGS thin films deposited by single-stage process and three-stage process at low temperature," *Optoelectron. Lett.*, vol. 9, no. 6, pp. 449–453, 2013, doi: 10.1007/s11801-013-3130-3.

[133] P. M. P. Salomé, H. Rodriguez-Alvarez, and S. Sadewasser, "Incorporation of alkali metals in chalcogenide solar cells," *Sol. Energy Mater. Sol. Cells*, vol. 143, pp. 9–20, 2015, doi: 10.1016/j.solmat.2015.06.011.

[134] Y. Sun *et al.*, "Review on Alkali Element Doping in Cu(In,Ga)Se2Thin Films and Solar Cells," *Engineering*, vol. 3, no. 4, pp. 452–459, 2017, doi: 10.1016/J.ENG.2017.04.020.

[135] M. Saifullah *et al.*, "The role of NaF post-deposition treatment on the photovoltaic characteristics of semitransparent ultrathin Cu(In,Ga)Se2 solar cells prepared on indium-tin-oxide back contacts: A comparative study," *J. Mater. Chem. A*, vol. 7, no. 38, pp. 21843–21853, 2019, doi: 10.1039/c9ta06274b.

[136] D. Rudmann *et al.*, "Efficiency enhancement of Cu (In , Ga) Se 2 solar cells due to post-deposition Na incorporation Efficiency enhancement of Cu „ In , Ga … Se 2 solar cells due to post-deposition Na incorporation," vol. 1129, no. 2004, pp. 21–24, 2014, doi: 10.1063/1.1646758.

[137] D. Güttler *et al.*, "Influence of NaF incorporation during Cu(In,Ga)Se2 growth on microstructure and photovoltaic performance," *Conf. Rec. IEEE Photovolt. Spec. Conf.*, pp. 3420–3424, 2010, doi: 10.1109/PVSC.2010.5614564.

[138] W. Li, X. Yan, A. G. Aberle, and S. Venkataraj, "Effect of sodium diffusion on the properties of CIGS solar absorbers prepared using elemental Se in a two-step process," *Sci. Rep.*, vol. 9, no. 1, pp. 1–11, 2019, doi: 10.1038/s41598-019-39283-2.

[139] V. Hadagali, "Study of The Effects of Sodium and Absorber Microstructure for the Development of Cuin1-Xgaxse2-Ysy Thin Film Solar Cell Using an Alternative Selenium Precursor," no. 2009, pp. 2004–2019, 2019.

[140] U. P. Singh and S. P. Patra, "Progress in Polycrystalline Thin-Film Cu (In , Ga) Se2 Solar Cells Progress in Polycrystalline Thin-Film Cu (In , Ga) Se 2 Solar Cells," no. July 2010, 2015, doi: 10.1155/2010/468147.

[141] M. Wang, M. A. Hossain, and K.-L. Choy, "Effect of Sodium Treatment on the Performance of Electrostatic Spray Assisted Vapour Deposited Copper-poor Cu(In,Ga)(S,Se) 2 Solar Cells," *Sci. Rep.*, vol. 7, no. 1, p. 6788, 2017, doi: 10.1038/s41598-017-07027-9.

[142] B. M. Keyes, F. Hasoon, P. Dippo, A. Balcioglu, and F. Abulfotuh, "Influence of Na on

the Electro- Optical Properties of Cu (In , Ga) Se 2," no. September, 1997.

[143] D. Colombara, K. Conley, and M. Malitckaya, "doping and Ga grading in Cu (In , Ga) Se 2 solar cells †," pp. 6471–6479, 2020, doi: 10.1039/d0ta01103g.

[144] M. T. Caldes *et al.*, "Layered Quaternary Compounds in the Cu2S-In2S3-Ga2S3 system," *Inorg. Chem.*, vol. 59, no. 7, pp. 4546–4553, 2020, doi: 10.1021/acs.inorgchem.9b03686.

[145] S. Zahedi-Azad, M. Maiberg, and R. Scheer, "Effect of Na-PDT and KF-PDT on the photovoltaic performance of wide bandgap Cu (In,Ga)Se2 solar cells," *Prog. Photovoltaics Res. Appl.*, vol. 28, no. 11, pp. 1146–1157, 2020, doi: 10.1002/pip.3317.

[146] T. Kodalle, "Unraveling the Structural and Optoelectronic Effects of Rb on Chalcopyrite Solar Cells Dissertation," 1990.

[147] P. Jackson, R. Wuerz, D. Hariskos, E. Lotter, W. Witte, and M. Powalla, "Effects of heavy alkali elements in Cu(In,Ga)Se2 solar cells with efficiencies up to 22.6%," *Phys. Status Solidi - Rapid Res. Lett.*, vol. 10, no. 8, pp. 583–586, 2016, doi: 10.1002/pssr.201600199.

[148] S. Kim *et al.*, "Reduced recombination in a surface-sulfurized Cu(InGa)Se2 thin-film solar cell," *Jpn. J. Appl. Phys.*, vol. 57, no. 5, 2018, doi: 10.7567/JJAP.57.055701.

[149] T. Kodalle *et al.*, "Elucidating the Mechanism of an RbF Post Deposition Treatment in CIGS Thin Film Solar Cells," *Sol. RRL*, vol. 2, no. 9, p. 1800156, 2018, doi: 10.1002/solr.201800156.

[150] S. Kim, H. Tampo, H. Shibata, K. Matsubara, and S. Niki, "Effect of Combined Alkali (KF + CsF) Post-Deposition Treatment on Cu(InGa)Se2 Solar Cells," *Phys. Status Solidi - Rapid Res. Lett.*, vol. 12, no. 10, pp. 1–5, 2018, doi: 10.1002/pssr.201800372.

[151] A. Laemmle, R. Wuerz, and M. Powalla, "Efficiency enhancement of Cu(In,Ga)Se2 thin-film solar cells by a post-deposition treatment with potassium fluoride," *Phys. Status Solidi - Rapid Res. Lett.*, vol. 7, no. 9, pp. 631–634, 2013, doi: 10.1002/pssr.201307238.

[152] X. Lyu *et al.*, "An investigation on performance enhancement for KF post deposition treated CIGS solar cells fabricated by sputtering CIGS quaternary targets," *Vacuum*, vol. 151, pp. 233–236, 2018, doi: 10.1016/j.vacuum.2018.02.023.

[153] A. Laemmle, R. Wuerz, and M. Powalla, "Investigation of the effect of potassium on Cu (In , Ga) Se 2 layers and solar cells KF-precursor KF-PDT," *Thin Solid Films*, vol. 582, pp. 27–30, 2015, doi: 10.1016/j.tsf.2014.10.088.

[154] M. Malitckaya *et al.*, "Alkali Postdeposition Treatment-Induced Changes of the Chemical and Electronic Structure of Cu(In,Ga)Se 2 Thin-Film Solar Cell Absorbers: A First-Principle Perspective," *ACS Appl. Mater. Interfaces*, vol. 11, no. 3, pp. 3024–

3033, 2019, doi: 10.1021/acsami.8b18216.

[155] H. Lee *et al.*, “Passivation of Deep-Level Defects by Cesium Fluoride Post-Deposition Treatment for Improved Device Performance of Cu(In,Ga)Se2 Solar Cells,” *ACS Appl. Mater. Interfaces*, vol. 11, pp. 35653–35660, 2019, doi: 10.1021/acsami.9b08316.

[156] M. Malitckaya, H. P. Komsa, V. Havu, and M. J. Puska, “Effect of Alkali Metal Atom Doping on the CuInSe2-Based Solar Cell Absorber,” *J. Phys. Chem. C*, vol. 121, no. 29, pp. 15516–15528, 2017, doi: 10.1021/acs.jpcc.7b03083.

[157] S. Swann, “Magnetron sputtering,” *Phys. Technol.*, vol. 19, no. 2, pp. 67–75, 1988, doi: 10.1088/0305-4624/19/2/304.

[158] C. Stan, C. Beavers, M. Kunz, and N. Tamura, “X-Ray Diffraction under Extreme Conditions at the Advanced Light Source,” *Quantum Beam Sci.*, vol. 2, no. 1, p. 4, 2018, doi: 10.3390/qubs2010004.

[159] A. Namin, C. Jivacate, D. Chenvidhya, K. Kirtikara, and J. Thongpron, “Determination of solar cell electrical parameters and resistances using color and white LED-based solar simulators with high amplitude pulse input voltages,” *Renew. Energy*, vol. 54, pp. 131–137, 2013, doi: 10.1016/j.renene.2012.08.046.

[160] C. Iatosti, M. Moret, A. Tiberj, and O. Briot, “Analysis of the gallium gradient in Cu(In1-xGax)Se2 absorbers by X-ray diffraction,” *Sol. Energy Mater. Sol. Cells*, vol. 220, no. October 2020, p. 110847, 2021, doi: 10.1016/j.solmat.2020.110847.

[161] S. Jung, S. J. Ahn, J. H. Yun, J. Gwak, D. Kim, and K. Yoon, “Effects of Ga contents on properties of CIGS thin films and solar cells fabricated by co-evaporation technique,” *Curr. Appl. Phys.*, vol. 10, no. 4, pp. 990–996, 2010, doi: 10.1016/j.cap.2009.11.082.

[162] S. A. Jensen *et al.*, “Beneficial effect of post-deposition treatment in high-efficiency Cu (In , Ga) Se 2 solar cells through reduced potential fluctuations,” 2016.

[163] C. A. Kaufmann *et al.*, “Depth profiling of Cu(In,Ga)Se2 thin films grown at low temperatures,” *Sol. Energy Mater. Sol. Cells*, vol. 93, no. 6–7, pp. 859–863, 2009, doi: 10.1016/j.solmat.2008.10.009.

[164] H. Miyazaki, R. Mikami, A. Yamada, and M. Konagai, “Cu(InGa)Se2thin film absorber with high Ga contents and its application to the solar cells,” *J. Phys. Chem. Solids*, vol. 64, no. 9–10, pp. 2055–2058, 2003, doi: 10.1016/S0022-3697(03)00204-X.

[165] W. Witte, R. Kniese, A. Eicke, and M. Powalla, “INFLUENCE OF THE GA CONTENT ON THE MO / CU (IN , GA) SE 2 INTERFACE FORMATION Raman Shift [cm] Sputter Time [s] Sputter Time [s],” pp. 553–556, 2006.

[166] J. Mu, J. Nowoczin, and H. Schmitt, “Composition , structure and optical properties of sputtered thin films of CuInSe 2,” vol. 496, pp. 364–370, 2006, doi: 10.1016/j.tsf.2005.09.077.

[167] A. Moreau *et al.*, “Solar Energy Materials & Solar Cells Impact of Cu – Au type domains in high current density CuInS 2 solar cells,” *Sol. Energy Mater. Sol. Cells*, vol. 139, pp. 101–107, 2015, doi: 10.1016/j.solmat.2015.03.008.

[168] M. Wang, M. A. Hossain, and K. L. Choy, “Effect of Sodium Treatment on the Performance of Electrostatic Spray Assisted Vapour Deposited Copper-poor Cu(In,Ga)(S,Se) 2 Solar Cells,” *Sci. Rep.*, vol. 7, no. 1, pp. 1–10, 2017, doi: 10.1038/s41598-017-07027-9.

[169] B. A. James, B. Adam, and J. Moores, “Research Collection,” 2004, doi: 10.3929/ethz-a-010782581.

[170] C. Insignares-Cuello, C. Broussillou, V. Bermúdez, E. Saucedo, A. Pérez-Rodríguez, and V. Izquierdo-Roca, “Raman scattering analysis of electrodeposited Cu(In,Ga)Se2 solar cells: Impact of ordered vacancy compounds on cell efficiency,” *Appl. Phys. Lett.*, vol. 105, no. 2, pp. 0–4, 2014, doi: 10.1063/1.4890970.

[171] A. Cuevas, “The recombination parameter J 0,” *Energy Procedia*, vol. 55, pp. 53–62, 2014, doi: 10.1016/j.egypro.2014.08.073.

[172] M. O. Salem *et al.*, “Over 10 % Ef fi cient Wide Bandgap CIGSe Solar Cells on Transparent Substrate with Na Predeposition Treatment,” no. October, 2020, doi: 10.1002/solr.202000284.

[173] X. Zheng, C. Xie, W. Li, A. G. Aberle, and S. Venkataraj, “Investigations of potassium-induced surface treatment of Cu(In,Ga)Se2 (CIGSe) thin film solar cells prepared by two-stage process using elemental selenium,” *Appl. Surf. Sci.*, vol. 525, no. December 2019, p. 146368, 2020, doi: 10.1016/j.apsusc.2020.146368.

[174] S. Paul *et al.*, “Analysis of Back-Contact Interface Recombination in Thin-Film Solar Cells,” *IEEE J. Photovoltaics*, vol. 8, no. 3, pp. 871–878, 2018, doi: 10.1109/JPHOTOV.2018.2819664.